Open access • Journal Article • DOI:10.1021/JACS.9B13620

Rationally Designed Long-Wavelength Absorbing Ru(II) Polypyridyl Complexes as Photosensitizers for Photodynamic Therapy — Source link

Johannes Karges, Franz Heinemann, Franz Heinemann, Marta Jakubaszek ...+11 more authors

Institutions: Chimie ParisTech, University of Zurich, Université Paris-Saclay, University of Extremadura

Published on: 25 Mar 2020 - Journal of the American Chemical Society (American Chemical Society (ACS))

Topics: Polypyridine complex

Rationally Designed Long-Wavelength Absorbing Ru(II) Polypyridyl Complexes as Photosensitizers for Photodynamic Therapy

Karges, Johannes ; Heinemann, Franz ; Jakubaszek, Marta ; Maschietto, Federica ; Subecz, Chloé ; Dotou, Mazzarine ; Vinck, Robin ; Blacque, Olivier ; Tharaud, Mickaël ; Goud, Bruno ; Viñuelas Zahínos, Emilio ; Spingler, Bernhard ; Ciofini, Ilaria ; Gasser, Gilles

Abstract: The utilization of photodynamic therapy (PDT) for the treatment of various types of cancer has gained increasing attention over the last decades. Despite the clinical success of approved photosensitizers (PSs), their application is sometimes limited due to poor water solubility, aggregation, photodegradation, and slow clearance from the body. To overcome these drawbacks, research efforts are devoted toward the development of metal complexes and especially Ru(II) polypyridine complexes based on their attractive photophysical and biological properties. Despite the recent research developments, the vast majority of complexes utilize blue or UV-A light to obtain a PDT effect, limiting the penetration depth inside tissues and, therefore, the possibility to treat deep-seated or large tumors. To circumvent these drawbacks, we present the first example of a DFT guided search for efficient PDT PSs with a substantial spectral red shift toward the biological spectral window. Thanks to this design, we have unveiled a Ru(II) polypyridine complex that causes phototoxicity in the very low micromolar to nanomolar range at clinically relevant 595 nm, in monolayer cells as well as in 3D multicellular tumor spheroids.

DOI: https://doi.org/10.1021/jacs.9b13620

Rationally Designed Long-Wavelength Absorbing Ru(II) Polypyridyl Complexes as Photosensitizers for Photodynamic Therapy

Johannes Karges,[†] Franz Heinemann,[†,‡] Marta Jakubaszek,[†,¶] Federica Maschietto,[§] Chloé Subecz,[†] Mazzarine Dotou,[†] Olivier Blacque,[‡] Mickaël Tharaud,[$] Bruno Goud,[¶] Emilio Viñuelas Zahínos,[⊥] Bernhard Spingler,[‡,*] Ilaria Ciofini,[§,*] and Gilles Gasser[†,*]

† Chimie ParisTech, PSL University, CNRS, Institute of Chemistry for Life and Health Sciences, Laboratory for Inorganic Chemical Biology, 75005 Paris, France.

‡ Department of Chemistry, University of Zurich, Winterthurerstrasse 190, 8057, Zurich, Switzerland.

¶ Institut Curie, PSL University, CNRS UMR 144, 75005 Paris, France.

§ Chimie ParisTech, PSL University, CNRS, Institute of Chemistry for Life and Health Sciences, Theoretical Chemistry and Modelling, 75005 Paris, France.

$ Université de Paris, Institut de physique du globe de Paris, CNRS, F-75005 Paris, France.

⊥ Departamento de Química Orgánica e Inorgánica, Facultad de Ciencias, Universidad de Extremadura, 06071 Badajoz, Spain.

KEYWORDS: Anticancer, Bioinorganic Chemistry, Medicinal Inorganic Chemistry, Metals in Medicine, Photodynamic Therapy.

ABSTRACT: The utilization of Photodynamic Therapy (PDT) for the treatment of various types of cancer has gained increasing attention over the last decades. Despite the clinical success of approved photosensitizers (PSs), their application is limited due to poor water solubility, aggregation, photodegradation, and slow clearance from the body. To overcome these drawbacks, research efforts are devoted towards the development of metal complexes and especially Ru(II) polypyridine complexes based on their attractive photophysical and biological properties. Despite the recent research developments, the vast majority of complexes utilize blue or UV-A light to obtain a PDT effect, limiting the penetration depth inside the tissue and therefore, the possibility to treat deep-seated or large tumors. To circumvent these drawbacks, we present the first example of the DFT guided search for efficient PDT PSs with a substantial spectral red shift towards the biological spectral window. Thanks to this design, we have unveiled a Ru(II) polypyridine complex, which causes phototoxicity in the very-low micromolar-to-nanomolar range at clinically relevant 595 nm, in monolayer cells as well as in 3D multicellular tumor spheroids.

INTRODUCTION

Photodynamic Therapy (PDT) is a non-invasive medical technique for the treatment of various types of cancer (e.g., lung, bladder, esophageal, and brain cancer) as well as bacterial, fungal or viral infections. The effect of PDT relies on the combination of an ideally non-toxic molecule, a so-called photosensitizer (PS), oxygen, and light. The PS is injected either systemically or locally. Upon light irradiation, the PS is uplifted to an excited singlet state from which the PS can undergo an intersystem crossing process to reach an excited triplet state. This state can influence the biological environment either by a Type I or Type II pathway. A Type I mechanism is characterized by an electron or proton transfer from or to the PS, which leads to the formation of reactive oxygen species (ROS) or other highly reactive radicals. In a Type II mechanism, the energy is transferred to triplet oxygen ($^3O_2$) to generate singlet oxygen ($^1O_2$). Due to their high reactivity, ROS and $^1O_2$ can cause oxidative stress and damage in different cellular compartments (i.e., membrane, nucleus, endoplasmic reticulum, lysosome, mitochondria). Both of these mechanisms can happen simultaneously upon light irradiation even so Type II pathway is the predominant one for most approved PSs.[1-6]

Photofrin is the most commonly used PS in PDT. It has been approved for the treatment of bladder cancer, early-stage lung cancer, esophageal cancer, and early non-small cell lung cancer. However, based on its low solubility and low absorption in the therapeutic window (i.e., 600-900 nm), high concentrations, as well as high light doses are required for an adequate tumor treatment making Photofrin not an ideal PS. Additionally, it was shown that this PS has an exceptionally long half-life excretion time leading to severe photosensitivity for the patients. Since the majority of investigated and approved PS are based on a tetrapyrrolic scaffold (i.e., porphyrins, chlorins, phthalocyanines), these PSs are likely to have similar drawbacks which include 1) poor water solubility; 2) tedious synthesis and purification; 3) low cancer selectivity; 4) photobleaching effect and 5) slow clearance from the body causing photosensitivity. Therefore, a need for modification of existing PSs or the development of new classes of PSs is needed.[7-14]

Among the new classes of PSs investigated the development of Ru(II) polypyridyl complexes as PDT PSs has received much attention due to their ideal photophysical and photochemical properties (i.e., high water solubility, high chemical stability and photostability, intense luminescence, large Stokes shifts, high $^1O_2$ production).[15-30] Worthy of note, the complex TLD-1433 $[Ru(dmb)_2(IP\text{-}TT)]^{2+}$ (dmb=4,4′-dimethyl-2,2′-bipyridine, IP-TT=2-(2′,2″:5″,2′ ″-terthiophene)-imidazol[4,5-f][1,10]phenanthroline) has just entered phase II clinical trial as a PDT PS for the treatment of non-muscle invasive bladder cancer in Canada.[31-34] Despite these remarkable properties, the majority of Ru(II)-based PS are typically excited using blue or UV-A light and therefore suffer from a lack of absorption in the biological spectral window (600-900 nm).[35-38] Based on absorption and light scattering effects in the biological environment, the light penetration depth into the tissue is low at this wavelength, which limits their application to treat deep tumors or large tumors.[39, 40] To overcome this limitation, there is a need for optimization of the absorption properties of Ru(II)-based PSs. It has been well-established that the photophysical properties, including absorption, emission as well as excited-state lifetimes of Ru(II) polypyridyl complexes depend on the ligands bound to the Ru center. This variable can, therefore, be tuned. In this context, we applied a combined experimental and theoretical approach to design new suitable Ru-based PDT PSs. Based on the already well-established biological activity of the complex $[Ru(phen)_3]^{2+}$ (phen = 1,10-phenanthroline) as a minor groove binder[41] and $[Ru(bphen)_3]^{2+}$ (bphen = 4,7-diphenyl-1,10-phenanthroline) as a mitochondria and lysosome targeting agent[42] and their ability to be effective PDT PSs[43-45], we decided to use $[Ru(phen)_2(bipy)]^{2+}$ and $[Ru(bphen)_2(bipy)]^{2+}$ (bipy = 2,2'-bipyridine) derivatives as basic scaffolds. In this investigation, the electronic properties, the origin, and the magnitude of red shift towards the biologic spectral window are disclosed. The resulting complexes (**1-7**, Figure 1) were synthesized, characterized, and biologically evaluated in-depth. Thanks to this combined study, a highly active Ru(II)-based PDT PS that can be excited up to 595 nm could be unveiled.

RESULTS AND DISCUSSION

Rational Design. As the basis of the design of Ru(II) polypyridine complexes as PDT PSs with red-shifted absorption near or in the biological spectral window, the $[Ru(phen)_2(bipy)]^{2+}$ scaffold was used due to its synthetic accessibility and generally high physical stability. To pursue this aim, systematic modification on the bipyridine moiety was investigated, and these effects studied by a theoretical and experimental approach.

It is well known that, in a simplified picture, the highest occupied orbitals in a pseudo-octahedral Ru(II) polypyridyl complex are mainly consisting of the Ruthenium t_{2g}-*d*-orbitals while the lowest occupied orbitals typically correspond to π*-orbitals localized on the ligands.[46, 47] Therefore, the lowest intense absorption band is expected to be of metal to ligand charge transfer (MLCT) character stemming from electronic transitions from the t_{2g} manifold to the empty ligands lowest-lying orbitals and leading to the population of a singlet state of MLCT nature under light irradiation. A simple way to red shift the MLCT absorption energy is, therefore, to decrease the HOMO-LUMO gap by an ad-hoc functionalization of the ligands. In particular, functionalization of the ligands with electron-donating and electron-withdrawing (EDG/EWG) groups is expected to increase the occupied MOs and lower the LUMO energy, respectively.

In the case of the unsubstituted compound **1**, the ligands are not strictly equivalent (two phen and one bipy ligand) so that the t_{2g} orbitals are not expected to be strictly degenerate. Nonetheless, from the computed MOs energies of **1**, it can be seen that the difference in energy between the t_{2g} orbitals is very tiny (roughly 0.04 eV) and the same holds for the LUMOs of π* character (roughly 0.08 eV) with contributions arising both from the phen and the bipy ligands. As a consequence, the functionalization of any of the two ligands shall induce a shift of the gap but is indeed expected to be easier in the case of the bipy, due to the reduced steric congestion around this ligand. For this reason, EDGs and EWGs were exclusively introduced only on the bipy ligand (**1-5**, Figure 1, optimized cartesian coordinates Table S1-S5).

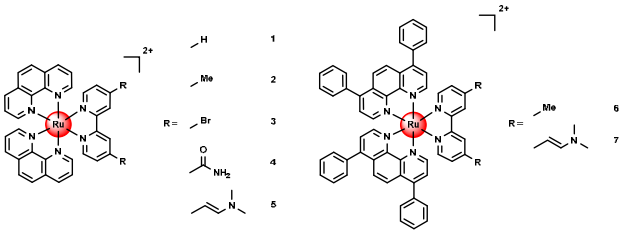

Figure 1. Chemical structures of the Ru(II) polypyridyl complexes investigated in this work. The complexes **1-7** were isolated as PF_6^- salts.

For this purpose, the energies of the frontier molecular orbitals were computed (Figure 2). Indeed, functionalization with -Me (**2**) (a weakly EDG) only negligibly affects the gap (reducing from 3.99 eV for **1** to 3.97 eV for **2**). A slightly more significant effect is obtained by weak EWGs such as -Br (**3**) and $-CONH_2$ (**4**, 3.83 eV, and 3.77 eV, respectively), which induce a small stabilization of the LUMO. These observations are in line with

the results previously obtained by some of us[48] when functionalizing with a -CHO group, a better EWG for which the computed gap is indeed 3.47 eV. On the other hand, functionalization with the vinyl dimethylamine-EDG (**5**) results in a substantial reduction of the HOMO-LUMO gap (to 3.24 eV, roughly 0.7 eV lower than the native compound (**1**) due to a sizable increase of the HOMO energy. Nonetheless, it should be underlined that the gap is reduced here due to the presence of occupied orbitals centered on the vinyl dimethylamine group in the gap. Therefore, although de facto the gap is substantially reduced, there is no destabilization of the t_{2g} manifold so that the bright MLCT transition (occurring from the t_{2g} orbitals to the π* ligand orbitals) is expected not to be affected (that is red-shifted).

To capitalize on this theoretical insight, we additionally examined the functionalization with a methyl and vinyl dimethylamine group on the $[Ru(bphen)_2(bipy)]^{2+}$ scaffold **6-7** (optimized cartesian coordinates Table S6-S7). Interestingly, changing the ligand scaffold from phen to bphen does not significantly affect the gap – as expected due to the small electronic effect induced by the presence of the four phenyl groups on the phen ligands. Indeed comparing compounds **2** and **6** or **5** and **7** (that are the analogous in the two series), a difference of only 0.1 and 0.07 eV in the gap, respectively, can be observed.

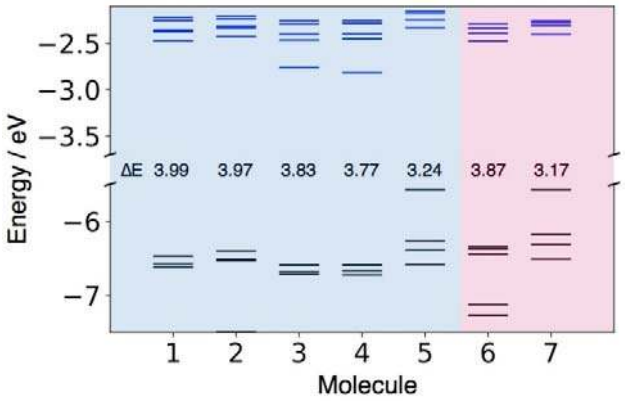

Figure 2. Computed frontier orbitals' energies and HOMO-LUMO gaps (in eV). Occupied/virtual orbitals energies are represented as black/blue line. Blue background: $Ru(phen)_2(bipy)^{2+}$ skeleton. Purple background: $Ru(bphen)_2(bipy)^{2+}$ skeleton.

Synthesis and Characterization. Based on the theoretical design, the Ru(II) polypyridine complexes **1-7** (Figure 1) were synthesized. To date, the synthesis of complexes **3–5** and **7** has not been yet reported, while complexes **1**[49], **2**[50], and **6**[51] are known. However, in this study, slightly different experimental procedures than the previously described were employed to obtain these compounds (for experimental protocols see supporting information). The identity of all complexes was confirmed by ^{1}H, ^{13}C-NMR (Scheme S1, Figures S1-S14), HRMS, and the purity by elemental analysis. In addition, the molecular structures of complexes **1-3** (Figure S15-17, Table S8-S9) were confirmed by single-crystal X-ray diffraction studies. The crystal structure of compound **1** has already been characterized by Huang and Ogawa[52], with the exception that the crystal structure presented here contains one solvent molecule of acetonitrile per ruthenium complex. In all molecular structures, the Ru(II) central atom adopts a distorted octahedral geometry chelated by two 1,10-phenanthroline ligands and one 2,2'-bipyridine ligand with Ru – N bond lengths ranging from 2.046(3) to 2.078(3) Å, $N_{phen} - Ru - N_{phen}$ angles from 79.48(12) to 80.1(2)°, and $N_{bipy} - Ru - N_{bipy}$ angles from 78.55(10) to 78.98(13)°. It is worth to note that the substitution of the bipyridine ligand by methyl groups in **2** and bromo ligands in **3** has no significant influence on the Ru – N bond distances.

Photophysical properties. The absorption spectra of the compounds **1-7** were measured in CH_3CN (Figure S19, extinction coefficients Table S10) and compared with the computed spectra (Figure 3). Although in the simulated spectra the energy of the MLCT band (around 450 nm) is systematically overestimated while the higher energy ligand centered (LE) band (around 300 nm) is better reproduced, small shifts towards the spectral windows of interest and a rise in intensity for the lowest energy band is indeed observed for the compounds **5**, **6** and **7**.

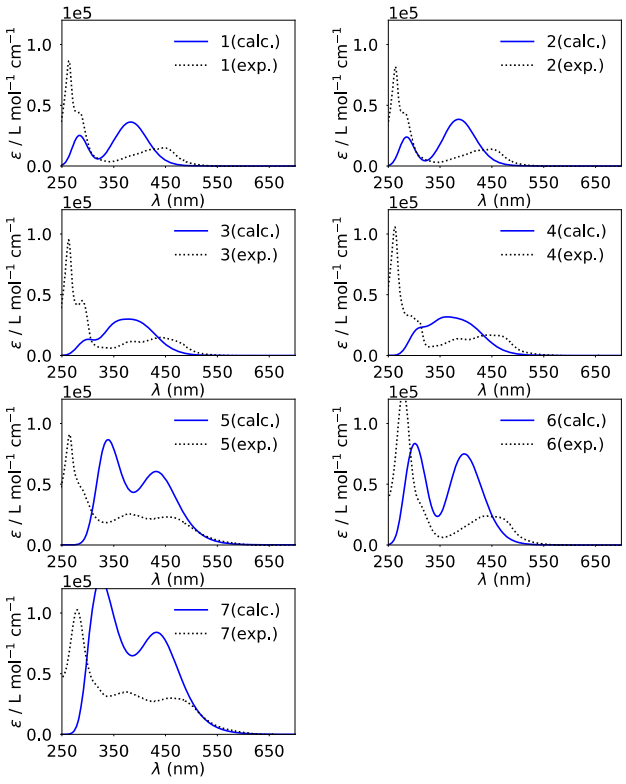

Figure 3. Simulated (blue) and experimental (black) spectra of compounds **1-7** in CH_3CN (c = 7.5 μM). Computed vertical electronic transitions are depicted as vertical blue bars. Corresponding oscillator strength (*f*) is given in a.u.

Of note, in the case of **5** and **7**, several electronic transitions are computed to contribute to the first -lowest energy- absorption band. The most intense has still an MLCT character while the one occurring at lower energy (less intense than those of MLCT character) and responsible for the tail and red-shift of the band are predicted

to be essentially ligand centered. These transitions are indeed of HOMO-LUMO type and, as discussed above, corresponding essentially to a transition from the vinyl dimethylamine group to the π* orbitals of the ligand. This can be visualized and understood from the maps of the difference in density between ground (GS) and excited state (ES) for two representative transitions of compound **6** (Figure S18a) and **7** (Figure S18b). For both complexes, the lowest energy transition (first electronic transition ES1) and the most intense one contributing to the first band (ES 4 and ES 9 for **6** and **7**, respectively) were analyzed. In Figure S18, density depletion/increase regions upon excitation for each are represented by blue/yellow zones, and the barycenters of these regions - depicted as blue/yellow dots - can be interpreted as the position of the electron and hole upon excitation. It can be clearly seen that while for complex **6**, both transitions have a clear MLCT character though not necessarily involving the same ligand, in the case of **7**, in agreement with the MO diagram, the lowest energy transition is of interligand type and mostly involving the vinyl dimethylamine-part. Therefore, even if a redshift of the first absorption band is predicted and indeed experimentally observed, it is not necessarily expected to correlate with an improvement of the phototherapeutic properties that are indeed linked to the population of a MLCT state.

Following this, the luminescence of the Ru(II) polypyridine complexes upon excitation at 355 nm was investigated. The maxima of the emission signals (Figure S20) were measured and found to be between 600-710 nm. Interestingly, complexes **5** and **7**, which showed the highest red shift in absorption, also demonstrated the strongest red shift in their emission maximum. All complexes demonstrated a large Stokes shift implying minimal inference between excitation and emission. The luminescence quantum yields were found with values between 5.0% - 1.4% (Table S10) for **1**-**4**, **6** and are therefore in the same range then other Ru(II) polypyridine complexes.[53, 54] On the contrary, the luminescence of **5** and **7** were barely measurable - with luminescence quantum yields >0.1%. This is consistent with the computed vertical absorption (see before) highlighting that for these two complexes the lowest lying excited states are of LC character. This result is also in agreement with the exceptionally low luminescence quantum yield of (*E*,*E*')-4,4'-bis(*N*,*N*'-dimethylaminovinyl)-2,2'-bipyridine in dichloromethane (1.5%) in comparison to other substituted 2,2'-bipyridines[55] and of the [Ru((*E*,*E*')-4,4'-bis(*N*,*N*'-dimethylaminovinyl)-2,2'-bipyridine)$_3$]$^{2+}$ complex in CH_3CN (>0.1%),[56] which were recently reported.

The excited-state lifetimes were determined in degassed and air-saturated CH_3CN solution to investigate the influence of the presence of oxygen. The obtained values (Figure S21-S27, Table S10) were found to be in the nanosecond scale in a degassed (312 – 1387 ns) and air saturated (55 – 326 ns) solution. All measured lifetimes were found to be in the same range as for other Ru(II) polypyridine complexes.[53, 54] Importantly, the data shows that the presence of oxygen has a significant influence on the lifetime of the excited state for all complexes indicating that molecular oxygen can interact with the triplet state of the complex.

The generation of singlet oxygen ($^1O_2$) was quantitatively measured upon excitation at 450 nm by two complementary methods: (i) direct by measurement of the phosphorescence of $^1O_2$, (ii) indirect by temporal monitoring the change of absorption of a $^1O_2$ scavenger.[57, 58] Complexes **1**-**4**, **6** were found to have $^1O_2$ quantum yields (Table S11) between 53-69% in CH_3CN and 5-36% in an aqueous solution, suggesting an application as a PDT agent. These values are comparable with those previously reported for related compounds.[59, 60] In comparison, the $^1O_2$ quantum yields of the (*E*,*E*')-4,4'-bis(*N*,*N*'-dimethylaminovinyl)-2,2'-bipyridine coordinated complexes **5** and **7** were found to be drastically lower with values of 22-35% in CH_3CN and 7-21% in an aqueous solution. This was expected as these compounds show an untypical excited state behavior (emission, luminescence, lifetime) which is also explained by DFT calculations.

Stability. The stability of a compounds is an essential parameter for their use as a PDT agent. As a first experiment, the stability of the complexes was investigated in a DMSO solution since this solvent was shown to be problematic for certain drug (candidates).[61-63] For this purpose, solutions of the complexes in DMSO-d_6 were prepared and stored in a NMR tube in the dark at room temperature. A ^{1}H-NMR spectrum was measured directly after preparing the solution after one, two and seven days. For complexes **1**-**4** and **6** (Figures S28-S31, S33), no significant change in the spectra were observed, indicating that no decomposition occurred. In contrast to this, small changes in the spectra for compounds **5** and **7** could be observed. For both compounds, changes in the signals could be detected after 7 days (Figures S32, S34). This indicates that these compounds are not stable in DMSO. To assess the compatibility of

Table 1. IC_{50} values (μM) for the complexes **1**-**7** and Protoporphyrin IX (PpIX) in mouse colon carcinoma (CT-26), human glioblastoma (U87), human glioblastoma astrocytoma (U373), human cervical carcinoma (HeLa) and non-cancerous retina pigmented epithelial (RPE-1) cell lines in the dark and upon light irradiation (480 nm, 10 min, 3.21 J cm^{-2}).

	CT-26			**U87**			**U373**			**HeLa**			**RPE-1**		
	Dark	**Light**	**PI**	**Dark**	**Light**	**PI**	**Dark**	**Light**	**PI**	**Dark**	**Light**	**PI**	**Dark**	**Light**	**PI**
1	>100	>100	-	>100	93.68 ± 2.50	>1	>100	>100	-	>100	>100	-	>100	>100	-
2	>100	91.24 ± 7.54	>1	>100	71.40 ± 5.67	>1	>100	>100	-	>100	>100	-	>100	>100	-
3	>100	85.71 ± 9.47	>1	>100	>100	-	>100	>100	-	>100	>100	-	>100	>100	-
4	>100	72.59 ± 7.44	>1	>100	>100	-	>100	>100	-	>100	>100	-	>100	>100	-
5	>100	52.54 ± 6.04	>2	>100	>100	-	>100	>100	-	>100	>100	-	>100	>100	-
6	3.09 ± 0.30	0.19 ± 0.04	16.3	28.45 ± 1.97	0.67 ± 0.13	42.5	23.37 ± 0.53	1.89 ± 0.07	12.4	13.57 ± 1.30	0.61 ± 0.06	22.2	28.77 ± 0.94	0.83 ± 0.03	34.9
7	94.47 ± 7.38	6.62 ± 0.07	14.3	>100	7.90 ± 0.54	>12.7	>100	14.85 ± 0.81	>6.7	>100	15.21 ± 1.29	>6.5	>100	8.95 ± 0.50	>11.2

the compounds under biological conditions, the stability of the complexes was tested in pooled human plasma. The complexes were incubated for 48 h in the dark with coffeine as an internal standard, which was previously shown to be stable under these conditions[64] and then analysed by HPLC (Figures S35-41). The stability of complexes **1**-**4** and **6** and the previously mentioned decomposition of compounds **5** and **7** were confirmed. Based on these findings, the stability of compounds **5** and **7** has been investigated more in detail by incubation of these complexes with shorter time intervals (0 h, 4 h, 12 h, 24 h, 48 h) in the dark. **5** shows first sign of degradation after 12 h and compound **7** after 24 h. The degradation of both complexes advanced in the investigated time interval, but still show unreacted complex even after 48 h incubation.

Following this, the potential decomposition of the complexes upon light irradiation was also tested as previous studied have shown that the stability of metal complexes could be influenced upon light exposure.[65, 66] This is crucially important as some of the currently approved PDT agents are associated with a strong photobleaching effect. The complexes were exposed to a continuous LED irradiation at 450 nm and the absorption spectra monitored. As a positive control $[Ru(bipy)_3]Cl_2$ and as a negative control Protoporphyrin IX was used. The comparison of the spectra shows that complexes **1**-**4** and **6** (Figure S42-46, 48) have a photobleaching effect in a similar range than $[Ru(bipy)_3]Cl_2$ (Figure S41). However, compounds **5** and **7** were found to be strongly affected by light irradiation with a loss of about half of their absorbance after one minute (Figure S47, 49). This effect is even stronger than that observed for Protoporphyrin IX (Figure S50).

Biological Evaluation. The lipophilicity/hydrophilicity of the compounds was determined by measuring the distribution coefficient (log*P*) between an organic octanol and aqueous phosphate buffer saline phase (Table S12). The complexes based on a $[Ru(phen)_2(bipy)]^{2+}$ scaffold (**1**-**5**) were found with log*P* values between +0.2 - +0.7 and the complexes based on a $[Ru(bphen)_2(bipy)]^{2+}$ scaffold (**6**-**7**) between +1.4 - +1.7. As all complexes were found majorly in the organic phase, their lipophilicity is indicated.

Following this, the cellular uptake of the compounds was investigated. Amount of Ru metal accumulated inside the human cervical carcinoma (HeLa) cells upon incubation for 4 h was determined by inductively coupled plasma mass spectrometry (ICP-MS). As expected, the compounds **6**-**7** which are based on a $[Ru(bphen)_2(bipy)]^{2+}$ scaffold showed a 2.1-5.8 times higher cellular accumulation (Figure S51) in comparison to compounds **1**-**5**, in agreement with their log*P* values.

To determine the potential of the complexes to act as PDT agents, mouse colon carcinoma (CT-26), human glioblastoma (U87) human glioblastoma astrocytoma (U373), human cervical carcinoma (HeLa) as well as non-cancerous retina pigmented epithelial (RPE-1) cell lines were treated with the complexes. Their cytotoxicity in the dark and upon light exposure was investigated using fluorometric cell viability assay (Table 1). Ideally, a PDT PS should be non-toxic in the dark and highly toxic upon light exposure. Promisingly, complexes **1**-**5** and **7** were found to be non-cytotoxic in the dark in all chosen cell lines (IC_{50} >100 μM), while compound **6** showed a cytotoxic profile in the range from 3.09 to 28.77 μM in all investigated cell lines. Upon irradiation at 480 nm (10 min, 3.21 J cm^{-2}), no or only poor toxicity (IC_{50} range from >100 to 52.54 μM) was observed for complexes based on a $[Ru(phen)_2(bipy)]^{2+}$ scaffold (**1**-**5**). In contrast, compounds based on the $[Ru(bphen)_2(bipy)]^{2+}$ scaffold (**6**-**7**) showed a notable phototoxicity upon light irradiation (Phototoxic index (PI)- IC_{50} in the dark/IC_{50} in upon irradiation, ranges from 6.5 to 42.5). This effect can be attributed to the significantly higher uptake of **6** and **7**. Overall, considering the instability of complex **7** in DMSO and human plasma and the absence/low phototoxicity of complexes **1**-**5**, complex **6** was further studied.

Following this preliminary examination, the ability to cause a phototoxic effect at longer wavelengths towards the biological spectral window was further evaluated. CT-26 cell line which was previously shown to be the strongest affected by this compound was chosen for subsequent studies. Importantly, light irradiation of the treated cells at 510 nm or 540 nm caused a phototoxic effect (Table 2). Strikingly, even irradiation at 595 nm generated a phototoxic effect in cells. It has to be noted that the lack of CO_2 atmosphere during irradiation also contributed to the obtained results. Nevertheless, the calculated PI values are reliable, as cells used as dark control were also incubated for the same amount of time at 37 °C in non-CO_2 atmosphere.

Table 2. IC_{50} values (μM) for **6** in mouse colon carcinoma (CT-26) cells in the dark and upon light irradiation at 510 nm (40 min, 10.00 J cm^{-2}), 540 nm (60 min, 14.25 J cm^{-2}) and 595 nm (2 h, 22.47 J cm^{-2}).

Wavelength /nm	Dark	Light	PI
510 nm	4.18 ± 0.56	0.20 ± 0.005	20.6
540 nm	3.27 ± 0.64	0.34 ± 0.005	9.6
595 nm	1.41 ± 0.003	0.06 ± 0.004	23.5

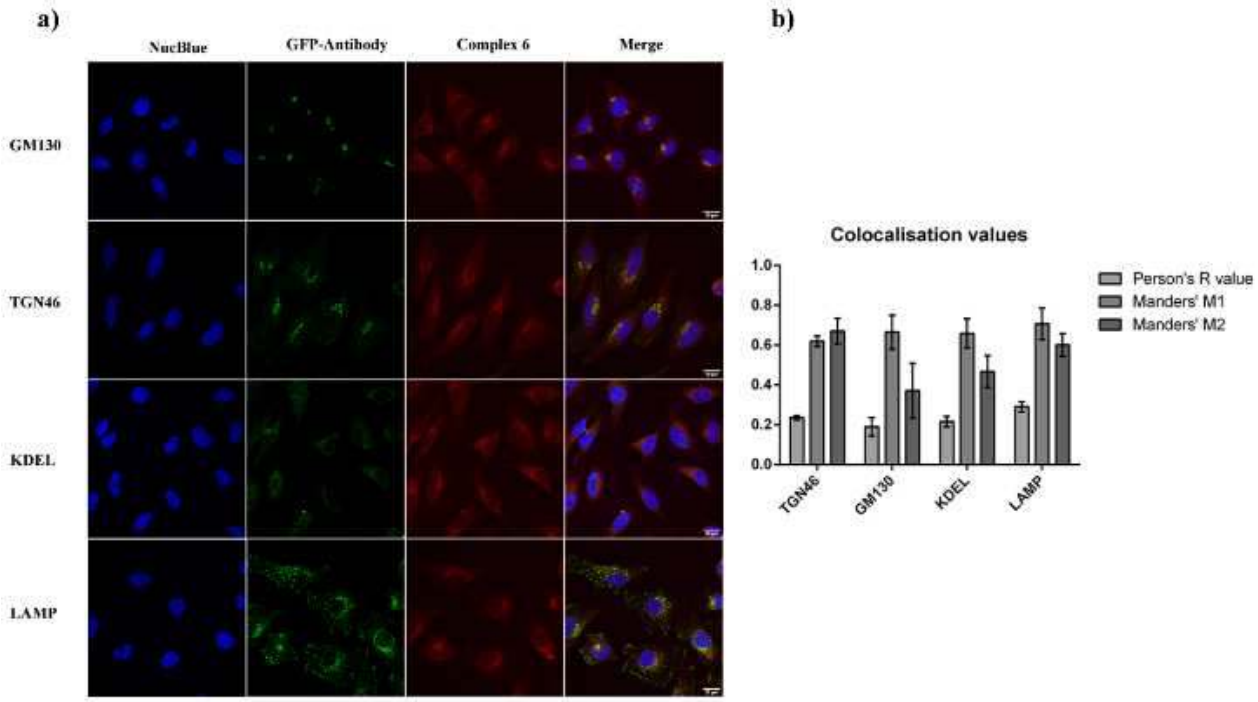

Figure 4. a) Immunofluorescent images of HeLa cells treated with complex **6** (14 µM, 30 min). DNA visualised by NucBlue staining, immunofluorescence for GM130, TGN46, KDEL and LAMP proteins shown in green, complex **6** shown in red. Scale bar, 20 µm. b) Person's R, Manders' M1 and Manders' M2 colocalisation values obtained for complex **6** and fluorescent probes.

Overall, these results make compound **6** an impressive candidate as a PDT agent.

To have a deeper insight in the mechanism of action of compound **6**, its cellular localisation in HeLa cell line was determined by confocal microscopy experiments. After 2 h incubation (14 µM), the complex was detected in the cytoplasm (see Figure S52). Immunofluorescence studies with GM130 (cis-Golgy protein), TGN46 (trans-Golgy protein), KDEL (endoplasmic reticulum protein retention receptor) and LAMP (lysosome- associated membrane glycoprotein) antibodies demonstrated that compound **6** did not colocalize with any of them (Figure 4a). Correlation analysis including Pearson's R value as well as Manders' M1 and Manders's M2 values confirmed the lack of colocalisation of the tested probes with complex **6** (Figure 4b). It is possible that the cytosolic localisation of our complex could be explained by its binding to the cytoskeleton as recently reported for structurally similar complex by the group of MacDonnell.[67]

To further study the mechanism of action of complex **6**, its influence on cellular metabolism was studied. Seahorse XF instrument was used which allows for real time measurements of oxygen consumption rate (OCR) and extracellular acidification rate (ECAR) in cells. To observe the effect of the compound **6** on oxidative phosphorylation (ATP production in mitochondria through electron transport chain), the Mito Stress test was performed. In this test, sequential injections of specific inhibitors of the electron transport chain proteins allows for determination of the effect that the compound has on the mitochondrial metabolism of the tested cells. Briefly, the cells were treated (4 h, 1µM) with complex **6** as well as with cisplatin and 5-ALA (5-aminolevulinic acid) - precursor of protoporphyrin IX (PpIX), a known photosensitizer, as controls.[68] After the incubation time, the cells were irradiated at 595 nm (2 h, 22.47 J cm^{-2}, see Figure S53) and the Mito Stress Test was performed. Strikingly, the data shows that only the cells, which were treated with complex **6** and irradiated, had their metabolism impaired right after the irradiation process. Injection of oligomycin (a specific inhibitor of ATP synthase) or FCCP (an uncoupling agent) did not affect their oxygen consumption rates. The mitochondrial membrane of these cells lost the capacity to restore the proton balance. ATP production was inhibited and spare respiratory capacity (difference between OCR values of maximal respiration and basal respiration) was strongly reduced, contrary to the cells treated with complex **6** that were not irradiated (Figure 5a and Figure S54).

Additional tests investigating whether the glycolysis is also affected were performed. Indeed, the glycolysis process is also severely impaired in the cells that are treated with complex **6** and irradiated (Figure 5b and Figure S55). It is known that the glycolysis process is significantly reduced during apoptosis.[69] Additionally, mitochondria are important compartment, which are responsible for triggering an intrinsic cell death.[70] It is then likely that the start of apoptosis is responsible for the initial effect in the cellular metabolism observed. A similar metabolic

response could not be noticed for the cisplatin. This phenomenon could be explained by the short incubation time (only 4 h) and the very low concentration tested (1 µM) that is not sufficient to trigger apoptosis by this drug in CT-26 cell line. Overall, compound **6** has an immediate effect on irradiated cells but not in the ones kept in the dark, resulting in disturbed mitochondrial respiration and glycolysis process.

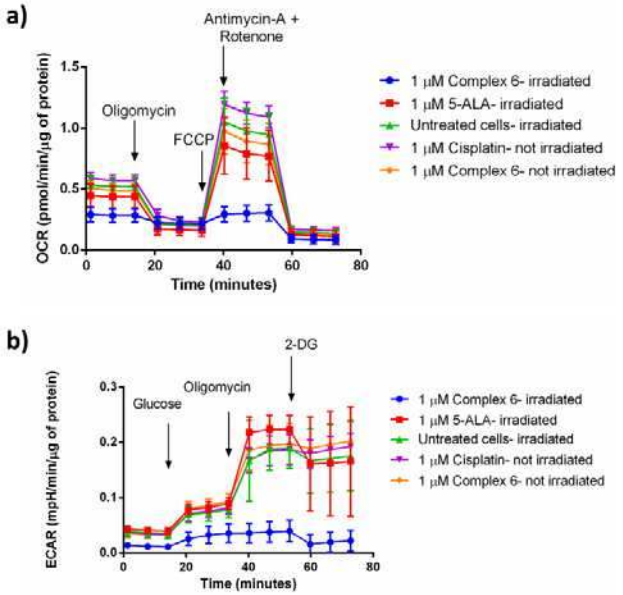

Figure 5. a) Mito Stress Test profile in CT-26 cells after 4 h treatment and 2 h irradiation at 595 nm; oxygen consumption rate changes after treatment with specific electron transport chain inhibitors, namely oligomycin (inhibitor of ATP synthase (complex V)), FCCP (uncoupling agent), antimycin-A (complex III inhibitor) and rotenone (complex I inhibitor). b) Glycolysis Stress Test profile in CT-26 cells after 4 h treatment and 2 h irradiation at 595 nm; extracellular acidification rate that corresponds to the glycolysis process changes after treatment with glucose (basal level of glycolysis in cells), oligomycin (inhibitor of ATP synthase (complex V)- mitochondria inhibition), 2-deoxyglucose (analog of glucose that inhibits glycolytic pathway).

After evaluation of the (photo-)cytotoxicity on 2D monolayer cells, the effect of complex **6** on multicellular tumor spheroids (MCTS) was investigated. This is of special interest as many anticancer drug candidates have failed the translation from monolayer cells to an *in vivo* model due to compromised drug delivery. MCTS are small spherical cell aggregates that mimic cell tumors. They can simulate the gradient of nutrients availability from upper cell layers, that are highly exposed, to lower layers and are able to model the potential penetration of a drug inside a 3D struture.[71, 72] Therefore, compound **6** was incubated for 24 h in HeLa MCTS and its cytotoxic effect determined by measurement of the ATP concentration. Importantly, upon irradiation at 595 nm (2 h, 22.47 J cm^{-2}), compound **6** showed a phototoxic effect ($IC_{50,dark}$ = 29.42 ± 4.60 µM, $IC_{50,595nm}$ = 20.07 ± 4.15 µM, PI_{595nm} = 1.5), indicating that the compound is able to exert its action inside the 3D MCTS and act as a PDT agent.

CONCLUSION

In summary, we have combined the theoretical understanding provided by DFT calculations with the photophysical and biological experimental evaluation of Ru(II) polypyridine complexes as PSs for PDT. Thanks to this rational design, ruthenium complexes with a strong red shift in their absorption profile could be successfully prepared. While the (*E*,*E*')-4,4'-bis(*N*,*N*'-dimethylaminovinyl)-2,2'-bipyridine coordinated complexes showed the desired red shift, they were however found to have poor photophysical properties (luminescence, $^1O_2$ production) and poor stability. In contrast, the $[Ru(bphen)_2(bmb)]^{2+}$ complex was found to have an absorption tail towards the biological spectral window. While being stable in human plasma as well as upon light irradiation, it was found to localize in the cytoplasm of HeLa cells. Upon irradiation at clinically relevant 595 nm it led to the disturbance of mitochondrial respiration and glycolysis process in 2D monolayer cells as well as 3D MCTS. We strongly believe that the rational design approach to unveil novel (metal-based) PDT PSs have a great potential in the development of PSs for long-wavelength PDT. We are planning to investigate the *in vivo* efficiency of compound **6** in the future.

ASSOCIATED CONTENT

The Supporting Information is available free of charge via the Internet at http://pubs.acs.org.

Detailed experimental protocols, supporting figures and tables.

AUTHOR INFORMATION

Corresponding Author

*spingler@chem.uzh.ch
*Ilaria.ciofini@chimieparistech.psl.eu
*gilles.gasser@chimieparistech.psl.eu; www.gassergroup.com; Tel. +33 1 44 27 56 02.

ORCID-ID:

Johannes Karges: 0000-0001-5258-0260
Franz Heinemann: 0000-0001-9590-443X
Federica Maschietto: 0000-0002-5995-2765
Marta Jakubaszek: 0000-0001-7590-2330
Chloé Subecz : 0000-0001-8510-4818
Mazzarine Dotou: 0000-0001-87814-6763
Olivier Blacque: 0000-0001-9857-4042
Bruno Goud: 0000-0003-1227-4159
Emilio Viñuelas Zahínos: 0000-0003-0634-1829
Bernhard Spingler: 0000-0003-3402-2016
Ilaria Ciofini: 0000-0002-5391-4522
Gilles Gasser: 0000-0002-4244-5097

ACKNOWLEDGMENT

We thank Dr. Philippe Goldner for access to state-of-the-art laser apparatus. This work was financially supported by an ERC Consolidator Grant PhotoMedMet to G.G. (GA 681679) and has received support under the program "Investissements d' Avenir" launched by the French Government and implemented by the ANR with the

reference ANR-10-IDEX-0001-02 PSL (G.G.). I.C and F.M. gratefully acknowledge the European Research Council (ERC) for funding (ERC Consolidator Grant STRIGES to I.C., GA No 648558).

ABBREVIATIONS

PDT, Photodynamic Therapy; PS, Photosensitiser; ROS, reactive oxygen species; $^1O_2$, singlet oxygen; dmb, 4,4′-dimethyl-2,2′-bipyridine; IP-TT, 2-(2′,2″:5″,2′ ″-terthiophene)-imidazol[4,5-f][1,10]phenanthroline; phen, 1,10-phenanthroline; bphen, 4,7-diphenyl-1,10-phenanthroline; bipy, 2,2'-bipyridine; MLCT, metal to ligand charge transfer; EDG, electron donating group; EWG, electron withdrawing group; LE, ligand centered; GS, ground state; ES, excited state; $^1O_2$, singlet oxygen; log*P*, distribution coefficient; PI, phototoxic index; ICP-MS, inductively coupled plasma mass spectrometry; HeLa, human cervical carcinoma cell line; CT-26, mouse colon carcinoma cell line; U87 human glioblastoma cell line, U373, human glioblastoma astrocytoma cell line, RPE-1 retina pigmented epithelial cell line; MCTS, multicellular tumor spheroid.

REFERENCES

1. D. E. Dolmans, D. Fukumura and R. K. Jain, *Nat. Rev. Cancer*, 2003, **3**, 380-387.
2. K. Plaetzer, B. Krammer, J. Berlanda, F. Berr and T. Kiesslich, *Lasers Med. Sci.*, 2009, **24**, 259-268.
3. S. Bonnet, *Dalton Trans.*, 2018, **47**, 10330-10343.
4. R. Bonnett, *Chem. Soc. Rev.*, 1995, **24**, 19-33.
5. T. J. Dougherty, C. J. Gomer, B. W. Henderson, G. Jori, D. Kessel, M. Korbelik, J. Moan and Q. Peng, *J. Natl. Cancer Inst.*, 1998, **90**, 889-905.
6. B. W. Henderson and T. J. Dougherty, *Photochem. Photobiol.*, 1992, **55**, 145-157.
7. A. E. O'Connor, W. M. Gallagher and A. T. Byrne, *Photochem. Photobiol.*, 2009, **85**, 1053-1074.
8. A. Naik, R. Rubbiani, G. Gasser and B. Spingler, *Angew. Chem. Int. Ed.*, 2014, **53**, 6938-6941.
9. F. Heinemann, J. Karges and G. Gasser, *Acc. Chem. Res.*, 2017, **50**, 2727-2736.
10. J. Karges, U. Basu, O. Blacque, H. Chao and G. Gasser, *Angew. Chem. Int. Ed.*, 2019, **58**, 14334-14340.
11. P. M. Antoni, A. Naik, I. Albert, R. Rubbiani, S. Gupta, P. Ruiz-Sanchez, P. Munikorn, J. M. Mateos, V. Luginbuehl, P. Thamyongkit, U. Ziegler, G. Gasser, G. Jeschke and B. Spingler, *Chem. Eur. J.*, 2015, **21**, 1179-1183.
12. P. Agostinis, K. Berg, K. A. Cengel, T. H. Foster, A. W. Girotti, S. O. Gollnick, S. M. Hahn, M. R. Hamblin, A. Juzeniene and D. Kessel, *CA Cancer J. Clin.*, 2011, **61**, 250-281.
13. S. Callaghan and M. O. Senge, *Photochem. Photobiol. Sci.*, 2018, **17**, 1490-1514.
14. L. Schneider, M. Larocca, W. Wu, V. Babu, R. Padrutt, E. Slyshkina, C. König, S. Ferrari and B. Spingler, *Photochem. Photobiol. Sci.*, 2019, **18**, 2792-2803.
15. C. Mari, V. Pierroz, S. Ferrari and G. Gasser, *Chem. Sci.*, 2015, **6**, 2660-2686.
16. S. Monro, K. L. Colón, H. Yin, J. Roque III, P. Konda, S. Gujar, R. P. Thummel, L. Lilge, C. G. Cameron and S. A. McFarland, *Chem. Rev.*, 2019, **119**, 797-828.
17. L. Zeng, P. Gupta, Y. Chen, E. Wang, L. Ji, H. Chao and Z.-S. Chen, *Chem. Soc. Rev.*, 2017, **46**, 5771-5804.
18. L. K. McKenzie, H. E. Bryant and J. A. Weinstein, *Coord. Chem. Rev.*, 2019, **379**, 2-29.
19. A. Li, C. Turro and J. J. Kodanko, *Acc. Chem. Res.*, 2018, **51**, 1415-1421.
20. J. Liu, C. Zhang, T. W. Rees, L. Ke, L. Ji and H. Chao, *Coord. Chem. Rev.*, 2018, **363**, 17-28.
21. F. E. Poynton, S. A. Bright, S. Blasco, D. C. Williams, J. M. Kelly and T. Gunnlaugsson, *Chem. Soc. Rev.*, 2017, **46**, 7706-7756.
22. M. Jakubaszek, J. Rossier, J. Karges, J. Delasoie, B. Goud, G. Gasser and F. Zobi, *Helv. Chim. Acta*, 2019, **102**, e1900104.
23. J. Shum, P. K.-K. Leung and K. K.-W. Lo, *Inorg. Chem.*, 2019, **58**, 2231-2247.
24. K. Qiu, Y. Chen, T. W. Rees, L. Ji and H. Chao, *Coord. Chem. Rev.*, 2019, **378**, 66-86.
25. J. Karges, M. Jakubaszek, C. Mari, K. Zarschler, B. Goud, H. Stephan and G. Gasser, *ChemBioChem*, doi:10.1002/cbic.201900419.
26. R. Lincoln, L. Kohler, S. Monro, H. Yin, M. Stephenson, R. Zong, A. Chouai, C. Dorsey, R. Hennigar, R. P. Thummel and S. A. McFarland, *J. Am. Chem. Soc.*, 2013, **135**, 17161-17175.
27. Y. Ellahioui, M. Patra, C. Mari, R. Kaabi, J. Karges, G. Gasser and S. Gómez-Ruiz, *Dalton Transactions*, 2019, **48**, 5940-5951.
28. B. S. Howerton, D. K. Heidary and E. C. Glazer, *J. Am. Chem. Soc.*, 2012, **134**, 8324-8327.
29. J. D. Knoll and C. Turro, *Coord. Chem. Rev.*, 2015, **282-283**, 110-126.
30. A. M. Palmer, B. Peña, R. B. Sears, O. Chen, M. E. Ojaimi, R. P. Thummel, K. R. Dunbar and C. Turro, *Philos. Trans. R. Soc. A*, 2013, **371**, 20120135.
31. https://theralase.com/pressrelease/theralase-annouces-first-patient-treated-in-phase-ii-non-muscle-invasive-bladder-cancer-clinical-study/, last accessed 20.09.2019.
32. J. Fong, K. Kasimova, Y. Arenas, P. Kaspler, S. Lazic, A. Mandel and L. Lilge, *Photochem. Photobiol. Sci.*, 2015, **14**, 2014-2023.
33. P. Kaspler, S. Lazic, S. Forward, Y. Arenas, A. Mandel and L. Lilge, *Photochem. Photobiol. Sci.*, 2016, **15**, 481-495.
34. S. A. McFarland, A. Mandel, R. Dumoulin-White and G. Gasser, *Curr. Opin. Chem. Biol.*, 2020, **56**, 23-27.
35. S. M. Cloonan, R. B. P. Elmes, M. Erby, S. A. Bright, F. E. Poynton, D. E. Nolan, S. J. Quinn, T. Gunnlaugsson and D. C. Williams, *J. Med. Chem.*, 2015, **58**, 4494-4505.
36. J. Karges, O. Blacque, M. Jakubaszek, B. Goud, P. Goldner and G. Gasser, *J. Inorg. Biochem.*, 2019, **198**, 110752.
37. H. Yin, M. Stephenson, J. Gibson, E. Sampson, G. Shi, T. Sainuddin, S. Monro and S. A. McFarland, *Inorg. Chem.*, 2014, **53**, 4548-4559.
38. E. Wachter, D. K. Heidary, B. S. Howerton, S. Parkin and E. C. Glazer, *Chem. Commun.*, 2012, **48**, 9649-9651.
39. K. Ogawa and Y. Kobuke, *Anti-Cancer Agents Med. Chem.*, 2008, **8**, 269-279.
40. B. C. Wilson, W. P. Jeeves and D. M. Lowe, *Photochem. Photobiol.*, 1985, **42**, 153-162.
41. M. Eriksson, M. Leijon, C. Hiort, B. Norden and A. Graeslund, *J. Am. Chem. Soc.*, 1992, **114**, 4933-4934.
42. M. Dickerson, Y. Sun, B. Howerton and E. C. Glazer, *Inorg. Chem.*, 2014, **53**, 10370-10377.

43. H. Audi, D. Azar, F. Mahjoub, S. Farhat, Z. El-Masri, M. El-Sibai, R. J. Abi-Habib and R. S. Khnayzer, *J. Photochem. Photobiol. A*, 2018, **351**, 59-68.
44. S. Mehanna, N. Mansour, H. Audi, K. Bodman-Smith, M. A. Mroueh, R. I. Taleb, C. F. Daher and R. S. Khnayzer, *RSC Adv.*, 2019, **9**, 17254-17265.
45. N. Mansour, S. Mehanna, M. A. Mroueh, H. Audi, K. Bodman-Smith, C. F. Daher, R. I. Taleb, M. El-Sibai and R. S. Khnayzer, *Eur. J. Inorg. Chem.*, 2018, **2018**, 2524-2532.
46. S. Finck, J.-T. Issenhuth, S. Despax, C. Sirlin, M. Pfeffer, C. Poidevin, C. Gourlaouen, A. Boeglin and C. Daniel, *J. Organomet. Chem.*, 2014, **760**, 248-259.
47. S. Campagna, F. Puntoriero, F. Nastasi, G. Bergamini, V. Balzani, *Photochemistry and Photophysics of Coordination Compounds I*, ed. V. Balzani, S. Campagna, Springer Berlin Heidelberg, 2007, 117-214.
48. J. Karges, F. Heinemann, F. Maschietto, M. Patra, O. Blacque, I. Ciofini, B. Spingler and G. Gasser, *Biorg. Med. Chem.*, 2019, **27**, 2666-2675.
49. G. Crosby and W. Elfring, *J. Phys. Chem.*, 1976, **80**, 2206-2211.
50. W. E. Jones Jr, R. A. Smith, M. T. Abramo, M. D. Williams and J. Van Houten, *Inorg. Chem.*, 1989, **28**, 2281-2285.
51. O. Mazuryk, K. Magiera, B. Rys, F. Suzenet, C. Kieda and M. Brindell, *J. Biol. Inorg. Chem.*, 2014, **19**, 1305-1316.
52. W. Huang and T. Ogawa, *Polyhedron*, 2006, **25**, 1379-1385.
53. M. J. Cook, A. P. Lewis, G. S. McAuliffe, V. Skarda, A. J. Thomson, J. L. Glasper and D. J. Robbins, *J. Chem. Soc., Perkin Trans. 2*, 1984, 1293-1301.
54. V. Balzani and A. Juris, *Coord. Chem. Rev.*, 2001, **211**, 97-115.
55. O. Maury, J.-P. Guégan, T. Renouard, A. Hilton, P. Dupau, N. Sandon, L. Toupet and H. Le Bozec, *New J. Chem.*, 2001, **25**, 1553-1566.
56. J. Karges, O. Blacque, P. Goldner, H. Chao and G. Gasser, *Eur. J. Inorg. Chem.*, 2019, 3704-3712.
57. J. Karges and G. Gasser, *Inorg. Chim. Acta*, 2020, **499**, 119196.
58. J. Karges, P. Goldner and G. Gasser, *Inorganics*, 2019, **7**, 4.
59. A. A. Abdel-Shafi, P. D. Beer, R. J. Mortimer and F. Wilkinson, *Helv. Chim. Acta*, 2001, **84**, 2784-2795.
60. D. Garcìa-Fresnadillo, Y. Georgiadou, G. Orellana, A. M. Braun and E. Oliveros, *Helv. Chim. Acta*, 1996, **79**, 1222-1238.
61. M. Patra, T. Joshi, V. Pierroz, K. Ingram, M. Kaiser, S. Ferrari, B. Spingler, J. Keiser and G. Gasser, *Chem. Eur. J.*, 2013, **19**, 14768-14772.
62. M. D. Hall, K. A. Telma, K.-E. Chang, T. D. Lee, J. P. Madigan, J. R. Lloyd, I. S. Goldlust, J. D. Hoeschele and M. M. Gottesman, *Cancer Res.*, 2014, **74**, 3913-3922.
63. S. Keller, Y. C. Ong, Y. Lin, K. Cariou and G. Gasser, *J. Organomet. Chem.*, 2019, 121059.
64. S. J. Bruce, I. Tavazzi, V. r. Parisod, S. Rezzi, S. Kochhar and P. A. Guy, *Anal. Chem.*, 2009, **81**, 3285-3296.
65. U. Basu, J. Karges, F. Chotard, C. Balan, P. Le Gendre, G. Gasser, E. Bodio and R. Malacea Kabbara, *Polyhedron*, 2019, **172**, 22-27.
66. A. K. Renfrew, J. Karges, R. Scopelliti, F. D. Bobbink, P. Nowak-Sliwinska, G. Gasser and P. Dyson, *ChemBioChem*, 2019, **20**, 2876-2882.
67. N. Alatrash, F. H. Issa, N. S. Bawazir, S. J. West, K. E. Van Manen-Brush, C. P. Shelor, A. S. Dayoub, K. A. Myers, C. Janetopoulos, E. A. Lewis and F. M. MacDonnell, *Chemi. Sci.*, 2019, doi: 10.1039/C9SC05671H.
68. K. Mahmoudi, K. L. Garvey, A. Bouras, G. Cramer, H. Stepp, J. G. Jesu Raj, D. Bozec, T. M. Busch and C. G. Hadjipanayis, *J. Neurooncol.*, 2019, **141**, 595-607.
69. L. A. Pradelli, E. Villa, B. Zunino, S. Marchetti and J. E. Ricci, *Cell Death Dis.*, 2014, **5**, e1406-e1406.
70. E. F. Mason and J. C. Rathmell, *Biochim. Biophys. Acta*, 2011, **1813**, 645-654.
71. J. Friedrich, C. Seidel, R. Ebner and L. A. Kunz-Schughart, *Nat. Protoc.*, 2009, **4**, 309-324.
72. T. T. Goodman, C. P. Ng and S. H. Pun, *Bioconjugate Chem.*, 2008, **19**, 1951-1959.

TABLE OF CONTENT (TOC) GRAPHIC:

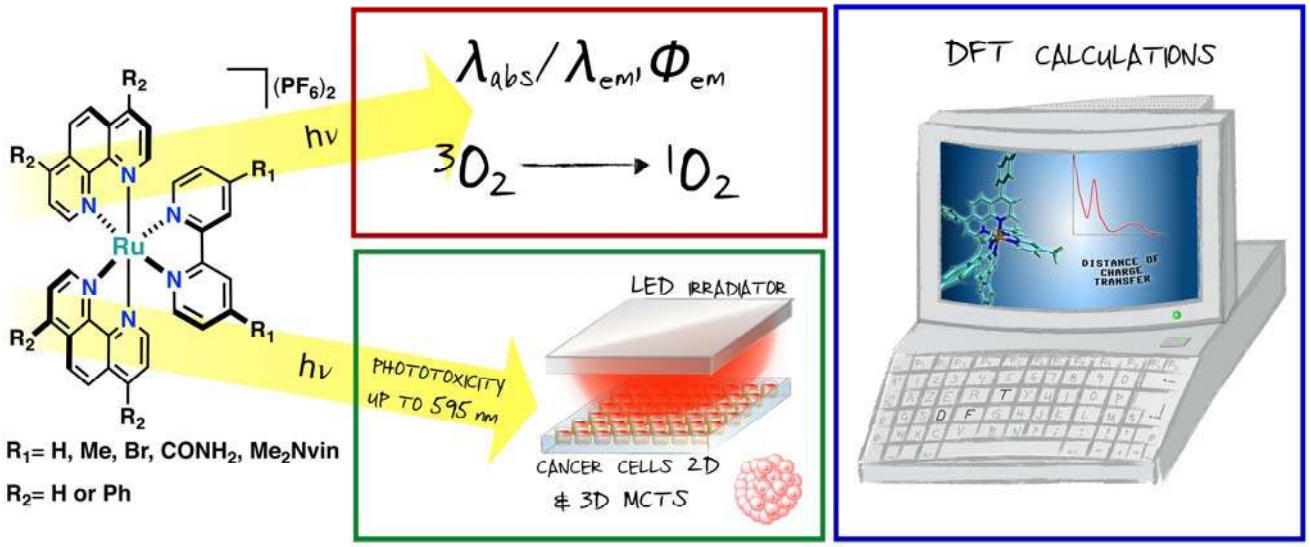

Supporting Information: Rationally Designed Long-Wavelength Absorbing Ru(II) Polypyridyl Complexes as Photosensitizers for Photodynamic Therapy

Johannes Karges,[†] Franz Heinemann,[†,‡] Marta Jakubaszek,[†,¶] Federica Maschietto,[§] Chloé Subecz,[†] Mazzarine Dotou,[†] Olivier Blacque,[‡] Mickaël Tharaud,[$] Bruno Goud,[¶] Emilio Viñuelas Zahínos,[⊥] Bernhard Spingler,[‡,*] Ilaria Ciofini,[§,*] and Gilles Gasser[†,*]

† Chimie ParisTech, PSL University, CNRS, Institute of Chemistry for Life and Health Sciences, Laboratory for Inorganic Chemical Biology, 75005 Paris, France.

‡ Department of Chemistry, University of Zurich, Winterthurerstrasse 190, 8057, Zurich, Switzerland.

¶ Institut Curie, PSL University, CNRS UMR 144, 75005 Paris, France.

§ Chimie ParisTech, PSL University, CNRS, Institute of Chemistry for Life and Health Sciences, Theoretical Chemistry and Modelling, 75005 Paris, France.

$ Université de Paris, Institut de physique du globe de Paris, CNRS, F-75005 Paris, France

⊥ Departamento de Química Orgánica e Inorgánica, Facultad de Ciencias, Universidad de Extremadura, 06071 Badajoz, Spain.

Table of Contents

EXPERIMENTAL SECTION

Computational Details

All calculations were performed using the Gaussian 09[1] software package. All calculations were performed using the Los Alamos LANL2[2] effective core potential and the corresponding triple-zeta basis set for the Ruthenium atom, with all other atoms treated with the Pople double-zeta basis set with a single set of polarisation and diffuse functions on non-hydrogen atoms (6-31+G(d)[3, 4]. Solvent effects (here acetonitrile) were included using an implicit model (i.e. the Polarizable Continuum Model – PCM[5]. All geometry optimisations were performed using density functional theory (DFT) with the global hybrid B3LYP[6] exchange-correlation functional and all minima on the potential energy surface were verified via a calculation of vibrational frequencies, ensuring no imaginary frequencies were present. Excited states of all compounds (as shown in Scheme 1) were probed using time dependent density functional theory (TD-DFT[7]) combined with the same exchange correlation functional and basis set. All transitions (singlet-singlet) were calculated vertically with respect to the singlet ground state. Absorption spectra were simulated by convolution with Gaussian functions with a full width at half maximum (FWHM) of 0.3 eV. In order to characterize the nature of the lowest energy states of interest (see discussion), relaxed excited state density was also computed together with the corresponding associated charge transfer distance (D_{CT})[8]. In brief the D_{CT} index provides a measure of the spatial extent of a given transition and yields a coherent representation of the charge rearrangements occurring upon generation of the exciton based on the ground and excited states density distributions. Details on how to calculate the D_{CT} index are reported in refs.[8, 9]

Materials

All chemicals were obtained from commercial sources and were used without further purification. Solvents were dried over molecular sieves if necessary. The Ru(II) complexes dichlorobis(1,10-phenanthroline)ruthenium(II) [$RuCl_2(phen)_2$] and dichlorobis(4,7-Diphenyl-1,10-phenanthroline)ruthenium(II) [$RuCl_2(bphen)_2$] were synthesised as previously published using the respective ligands.[10] The substituted bipyridine ligands 2,2'-bipyridine-4,4'-dicarbonitrile[11] and (*E*,*E*')-4,4'-bis(*N*,*N*-dimethylaminovinyl)-2,2'-bipyridine[12] were synthesised as previously reported.

Instrumentation and methods

^{1}H and ^{13}C NMR spectra were recorded on a Bruker 400 MHz or Bruker 500 MHz NMR spectrometer. Chemical shifts (δ) are reported in parts per million (ppm) referenced to tetramethylsilane (δ 0.00) ppm using the residual proton solvent peaks as internal standards. Coupling constants (J) are reported in Hertz (Hz) and the multiplicity is abbreviated as follows: s (singlet), d (doublet), dd (doublet of doublet), t (triplet), m (multiplet). ESI mass spectra were recorded on a Bruker ESQUIRE-LC quadrupole ion trap spectrometer. Elemental microanalyses were performed on a LecoCHNS-932 elemental analyser or a Thermo Flash 2000 elemental analyser. Inductively coupled plasma mass spectrometry (ICP-MS) experiments were carried out on HR-ICP-MS Element II (Thermo Scientific) apparatus.

Synthesis

Proton and carbon NMR spectra can be found in the supplemental information (Figures S1-14).

(1) $[Ru(bpy)(phen)_2](PF_6)_2$

(2,2'-Bipyridine)bis(1,10-phenanthroline)ruthenium(II)hexafluorophosphate

The synthesis of $[Ru(bipy)(phen)_2](PF_6)_2$ is already published[13] but in this study another synthetic route was employed. $RuCl_2(phen)_2$ (150 mg, 0.28 mmol, 1.0 equiv.) and 2,2′-bipyridine (48 mg, 0.31 mmol, 1.1 equiv.) were dissolved in 8 mL MeOH and refluxed for 18 h under N_2 atmosphere. After this time, the volume of the brown mixture was reduced to 1/4. A saturated, aq. NH_4PF_6 solution was added and the resulting precipitate was collected by vacuum filtration and washed with H_2O (50 mL) and Et_2O (50 mL). The product was dried in high vacuum. Yield: 51%. ^{1}H NMR (500 MHz, CD_3CN) δ = 8.65 (dd, 2H, *J* = 8.3, 1.3 Hz), 8.55 (dd, 2H, *J* = 8.2, 1.3 Hz), 8.52 (d, 2H, *J* = 8.3 Hz), 8.26 (d, 2H, *J* = 8.9 Hz), 8.23 (d, 2H, *J* = 8.9 Hz), 8.20 (d, 2H, *J* = 5.2 Hz), 8.03 (td, 2H, *J* = 8.1, 1.4 Hz), 7.88 (dd, 2H, *J* = 5.3, 1.2 Hz), 7.79 (dd, 2H, *J* = 8.3, 5.2 Hz), 7.67 (d, 2H, *J* = 5.6 Hz), 7.56 (dd, 2H, *J* = 8.2, 5.3 Hz), 7.27 (ddd, 2H, *J* = 7.3, 5.6, 1.3 Hz); ^{13}C NMR (125 MHz, CD_3CN) δ = 158.3, 153.8, 153.6, 153.2, 148.8, 148.6, 138.7, 137.8, 137.7, 132.0, 132.0, 129.0, 129.0, 128.3, 127.0, 126.8, 125.1; HRMS (ESI^+ m/z): Calcd. for $[C_{34}H_{24}F_{12}N_6P_2Ru\text{-}2PF_6]^{2+}$: 309.05478, Found: 309.05475, Calcd. for $[C_{34}H_{24}F_{12}N_6P_2Ru\text{-}PF_6]^{+}$: 763.07423, Found: 763.07434; Anal. Calcd. for $C_{34}H_{24}F_{12}N_6P_2Ru$: C, 44.99; H, 2.67; N, 9.26, Found: C, 44.69; H, 2.61; N 9.25.

(2) $[Ru(dmb)(phen)_2](PF_6)_2$

(4,4′-Dimethyl-2,2′-bipyridine)bis(1,10-phenanthroline)ruthenium(II) hexafluorophosphate

The synthesis of $[Ru(dmb)(phen)_2](PF_6)_2$ is already published[14] but in this study another synthetic route was employed. $RuCl_2(phen)_2$ (150 mg, 0.28 mmol, 1.0 equiv.) and 4,4'-dimethyl-2,2'-bipyridine (57 mg, 0.31 mmol, 1.1 equiv.) were dissolved in a 1:1 mixture of H_2O/EtOH (7 mL) and were refluxed for 18 h under N_2 atmosphere. The solvent was evaporated to one third of the volume and a saturated, aq. NH_4PF_6 solution was added. The resulting precipitate was collected by vacuum filtration and washed with H_2O (50 mL) and Et_2O (50 mL). The product was dried in high vacuum. Yield: 97%. ^{1}H NMR (400 MHz, CD_3CN) δ = 8.64 (dd, 2H, *J* = 8.3, 1.3 Hz), 8.53 (dd, 2H, *J* = 8.3, 1.3 Hz), 8.37 (s, 2H), 8.25 (d, 2H, *J* = 8.9 Hz), 8.22 (d, 2H, *J* = 8.9 Hz) 8.20 (dd, *J* = 5.3, 1.3 Hz), 7.88 (dd, 2H, *J* = 5.3, 1.3 Hz), 7.79 (dd, 2H, *J* = 8.3, 5.3 Hz), 7.54 (dd, 2H, *J* = 8.2, 5.3 Hz), 7.47 (d, 2H, *J* = 5.8 Hz), 7.10 (dd, 2H, *J* = 5.8, 1.2 Hz), 2.51 (s, 6H); ^{13}C NMR (100 MHz, CD_3CN) δ = 157.8, 153.6, 153.6, 152.2, 151.3, 148.9, 148.7, 137.6, 137.5, 131.9, 131.9, 129.0, 129.0, 129.0, 126.9, 126.8, 125.8, 21.2; HRMS (ESI^+ m/z): Calcd. for $[C_{36}H_{28}F_{12}N_6P_2Ru\text{-}2PF_6]^{2+}$: 323.07040, Found: 323.07040; Anal. Calcd. for $C_{36}H_{28}F_{12}N_6P_2Ru+2H_2O$: C, 44.50; H, 3.32; N, 8.65, Found: C, 44.43; H, 3.08; N, 8.52.

(3) $[Ru(Br\text{-}bpy)(phen)_2](PF_6)_2$

(4,4′-Dibromo-2,2′-bipyridine)bis(1,10-phenanthroline)ruthenium(II) hexafluorophosphate

$RuCl_2(phen)_2$ (150 mg, 0.28 mmol, 1.0 equiv.) and 4,4'-Dibromo-2,2'-bipyridine (105 mg, 0.34 mmol, 1.2 equiv.) were dissolved in a 1:1 mixture of H_2O/EtOH (40 mL) and were refluxed for 18 h under N_2 atmosphere. The solvent was evaporated and the residue redissolved in 5 mL of H_2O. A saturated, aq. NH_4PF_6 solution was added and the resulting precipitate was collected by vacuum filtration. The solid was washed with H_2O (50 mL) and Et_2O (50 mL). The product was isolated by column chromatography on silica gel with an CH_3CN/aq. KNO_3 (0.4 M) solution (10:1). The fractions containing the product were united and the solvent was removed. The residue was dissolved in CH_3CN and undissolved KNO_3 was removed by filtration. The solvent was removed and the product was dissolved in H_2O (50 mL). Upon addition of NH_4PF_6 the product precipitated as a PF_6 salt. The solid was obtained by filtration and was washed with H_2O (50 mL) and Et_2O (50 mL). The product was dried in high vacuum. Yield: 78%. ^{1}H NMR (500 MHz, CD_3CN) δ = 8.76 (2H, d, *J* = 2.0 Hz), 8.68 (2H, dd, *J* = 8.3, 1.3 Hz), 8.55 (2H, dd, *J* = 8.3, 1.3 Hz), 8.27 (2H, d, *J* = 8.9 Hz), 8.25 (2H, dd, *J* = 5.3, 1.3 Hz), 8.22 (2H, d, *J* = 8.9

Hz), 7.84 (2H, dd, *J* = 5.3, 1.3 Hz), 7.81 (2H, dd, *J* = 8.3 , 5.2 Hz), 7.55 (2H, dd, *J* = 8.3, 5.3 Hz), 7.50 (2H, d, *J* = 6.1 Hz), 7.47 (2H, dd, *J* = 6.1, 2.0 Hz). ^{13}C NMR (125 MHz, CD_3CN) δ = 158.3, 154.0, 153.9, 153.6, 148.7, 148.4, 138.0, 137.9, 134.7, 132.0, 132.0, 131.7, 129.1, 129.0, 129.0, 127.0, 126.9. HR-MS (ESI$^+$ m/z): Calcd. $[M\text{-}2PF_6]^{2+}$: 386. 96526; found: 386. 96576. Anal. (%): Calcd. for ($C_{34}H_{22}Br_2F_{12}N_6P_2Ru$): C 38.33, H 2.08, N 7.89; found. C 38.62, H 2.01, N 7.78.

(4) $[Ru(CONH2\text{-}bpy)(phen)_2](PF_6)_2$

(2,2'-bipyridine-4,4'-carboxamide)bis(1,10-phenanthroline)ruthenium(II) hexafluorophosphate

$RuCl_2(phen)_2$ (150 mg, 0.28 mmol, 1.0 equiv.) and 2,2'-Bipyridine-4,4'-dicarbonitrile (64 mg, 0.31 mmol, 1.1 equiv.) were dissolved in a 1:1 mixture of H_2O/EtOH (30 mL) and were refluxed for 18 h under N_2 atmosphere. The solvent was evaporated and the residue redissolved in 5 mL of H_2O. A saturated, aq. NH_4PF_6 solution was added and the resulting precipitate was collected by vacuum filtration. The solid was washed with H_2O (50 mL) and Et_2O (50 mL). The product was purified by column chromatography on silica gel with an CH_3CN /aq. KNO_3 (0.4 M) solution (10:1). The fractions containing the product were united and the solvent was removed. The residue was dissolved in CH_3CN and undissolved KNO_3 was removed by filtration. The solvent was removed again and the product was dissolved in H_2O (50 mL). Upon addition of NH_4PF_6 the product precipitated as a PF_6 salt. The solid was obtained by filtration and was washed with H_2O (50 mL) and Et_2O (50 mL). The product was dried in high vacuum. Yield: 16%. ^{1}H NMR (400 MHz, CD_3CN) δ = 8.97 (2H, s), 8.67 (2H, d, *J* = 8.3 Hz), 8.58 (2H, d, *J* = 8.3 Hz), 8.30-8.22 (4H, m), 8.18 (2H, d, *J* = 5.2 Hz), 7.87-7.84 (4H, m), 7.79 (2H, dd, *J* = 8.3, 5.2 Hz), 7.61-.7.57 (4H, m), 7.25 (2H, s), 6.48 (2H, s). ^{13}C NMR (100 MHz, CD_3CN) δ = 165.7, 158.8, 154.0, 153.9, 153.5, 148.6, 148.3, 143.0, 138.2, 138.0, 132.1, 132.0, 129.1, 129.0, 127.0, 127.0, 126.0, 123.1. HR-MS (ESI$^+$ m/z): Calcd. $[M\text{-}2PF_6]^{2+}$: 352.06056; found: 352.06063. Anal. (%): Calcd. for ($C_{36}H_{26}F_{12}N_8O_2P_2Ru$): C 43.52, H 2.64, N 11.28; found. C 43.33, H 2.47, N 11.15.

(5) $[Ru(Me_2Nvin\text{-}bpy)(phen)_2](PF_6)_2$

((*E*,*E*')-4,4'-Bis(*N*,*N*'-dimethylaminovinyl)-2,2'-bipyridine)bis(1,10-phenanthroline) ruthenium(II) hexafluorophosphate

[Ru(dmb)(phen)$_2$](PF$_6$)$_2$ (**2**) (100 mg, 0.11 mmol, 1.0 equiv.) was dissolved in dry DMF (1.5 mL) and *tert*-butoxy bis(dimethylamino)methane (0.2 mL, 0.97 mmol, 8.8 equiv.) was added. The mixture was heated at 140 °C for 16 h under N_2 atmosphere. The solution was cooled down and an aq. solution of NH_4PF_6 was added. The resulting precipitate was collected by vacuum filtration and the solid was washed with H_2O (50 mL) and Et_2O (50 mL). The product was isolated via fractionated precipitation from CH_3CN by adding dropwise Et_2O and afterwards dried in high vacuum. Yield: 41%. ^{1}H NMR (400 MHz, CD_3CN) δ = 8.61 (2H, dd, *J* = 8.3, 1.3 Hz), 8.48 (2H, dd, *J* = 8.3, 1.3 Hz), 8.38 (2H, dd, *J* = 5.3, 1.3 Hz), 8.24 (2H, d, *J* = 8.9 Hz), 8.19 (2H, *J* = 9.0 Hz), 8.08 (2H, d, *J* = 2.2 Hz), 7.87 (2H, dd, *J* = 5.3, 1.3 Hz), 7.82 (2H, dd, *J* = 8.2 Hz, 5.3 Hz), 7.52 (2H, dd, *J* = 8.2 Hz, 5.3 Hz), 7.51 (2H, d, *J* = 13.3 Hz), 6.99 (2H, d, *J* = 6.2 Hz), 6.77 (2H, dd, *J* = 6.2, 2.1 Hz), 5.08 (2H, d, *J* = 13.4 Hz), 2.94 (12H, s). ^{13}C NMR (100 MHz, CD_3CN) δ = 157.6, 153.5, 153.5, 151.6, 150.6, 149.2, 149.1, 147.8, 137.0, 137.0, 131.9, 131.9, 129.0, 129.0, 126.9, 126.7, 120.3, 117.1, 92.9, 40.1. HR-MS (ESI$^+$ m/z): Calcd. [M-2PF$_6$]$^{2+}$: 378.11260; found: 378.11289. Anal. (%): Calcd. for ($C_{42}H_{38}F_{12}N_8P_2Ru$): C 48.24, H 3.66, N 10.71; found: C 47.97, H 3.59, N 10.76.

(6) [Ru(dmb)(bphen)$_2$](PF$_6$)$_2$ <

(4,4′-Dimethyl-2,2′-bipyridine)bis(4,7-diphenyl-1,10-phenanthroline)ruthenium(II) hexafluorophosphate

The synthesis of [Ru(dmb)(bphen)$_2$](PF$_6$)$_2$ is already published[15] but in this study another synthetic route was employed. $RuCl_2(bphen)_2$ (200 mg, 0.24 mmol, 1.0 equiv.) and 4,4'-Dimethyl-2,2'-bipyridine (53 mg, 0.29 mmol, 1.2 equiv.) were dissolved in a 1:1 mixture of H_2O/EtOH (10 mL) and were refluxed for 18 h under N_2 atmosphere. The solvent was evaporated and the residue redissolved in 10 mL of H_2O. A saturated, aq. NH_4PF_6 solution was added and the suspension was sonicated. 60 mL of H_2O were added and the resulting precipitate was collected by vacuum filtration. The solid was washed with H_2O (50 mL) and Et_2O (50 mL). The product was dried in high vacuum. Yield: 93%. ^{1}H NMR (400 MHz, CD_3CN) δ = 8.44 (2H, s), 8.29 (2H, d, *J* = 5.5 Hz), 8.22-8.16 (m, 4H), 8.10 (2H, d, *J* = 5.5 Hz), 7.75 (2H, d, *J* = 5.5 Hz), 7.72 – 7.53 (24H, m), 7.21 (2H, d, *J* = 5.8, *J* = 1.7 Hz), 2.56 (6H, s). ^{13}C NMR (125 MHz, CD_3CN) δ = 157.7, 153.1, 152.9, 152.2, 151.4, 149.9, 149.8, 149.5, 149.4, 136.7, 136.7, 130.8, 130.7, 130.7, 130.6, 130.6, 130.1, 130.1, 130.1, 129.9, 129.9, 129.1, 127.1, 127.0, 127.0, 126.9, 125.8, 21.3. HR-MS (ESI$^+$ m/z): Calcd. [M-2PF$_6$]$^{2+}$: 475.13300; found: 475.13388. Anal.

(%): Calcd. ($C_{60}H_{44}F_{12}N_6P_2Ru$)·($H_2O$)$_2$: C 56.47, H 3.79, N 6.59; found: C 56.46, H 3.85, N 6.11.

(7) [Ru(Me$_2$Nvin-bipy)(bphen)$_2$](PF$_6$)$_2$

((*E*,*E*')-4,4'-Bis(*N*,*N*'-dimethylaminovinyl)-2,2'-bipyridine)bis(4,7-diphenyl-1,10-phenanthroline)ruthenium(II) hexafluorophosphate

[Ru(dmb)(bphen)$_2$](PF$_6$)$_2$ (**7**) (150 mg, 0.12 mmol, 1.0 equiv.) was dissolved in dry DMF (1.5 mL) and *tert*-butoxy bis(dimethylamino)methane (0.3 mL, 1.45 mmol, 12.1 equiv.) was added. The mixture was heated at 140 °C for 18 h under N_2 atmosphere. After this time, more *tert*-butoxy bis(dimethylamino)methane (0.4 mL, 1.94 mmol, 16.2 equiv.) was added the mixture was heated at 145 °C for 72 h under N_2 atmosphere. The solution was cooled down and an aq. solution of NH_4PF_6 was added. The resulting precipitate was collected by vacuum filtration and the solid was washed with H_2O (50 mL) and Et_2O (50 mL). The product was isolated via fractionated precipitation from CH_3CN by adding dropwise Et_2O and afterwards dried in high vacuum. Yield: 67%. ^{1}H NMR (500 MHz, CD_3CN) δ = 8.48 (2H, d, *J* = 5.5 Hz), 8.20 (2H, d, *J* = 9.4 Hz), 8.16 8.20 (2H, d, *J* = 9.5 Hz), 8.13 (2H, d, *J* = 2.11 Hz), 8.09 (2H, d, *J* = 5.5 Hz), 7.80 (2H, d, *J* = 5.5 Hz), 7.69 – 7.52 (22H, m), 7.21 (2H, d, *J* = 6.2 Hz), 6.87 (2H, dd, *J* = 6.3, 2.0 Hz), 5.14 (2H, d, *J* = 13.4 Hz), 2.96 (12H, s). ^{13}C NMR (125 MHz, CD_3CN) δ = 157.4, 152.9, 152.7, 151.5, 150.6, 149.7, 149.6, 149.2, 149.2, 149.2, 149.2, 149.2, 147.7, 136.9, 136.8, 130.8, 130.7, 130.7, 130.5, 130.5, 130.1,130.0, 130.0, 129.7, 129.7, 127.1, 126.9, 126.8, 126.8, 120.2, 117.0, 92.7, 40.7. HR-MS (ESI$^+$ m/z): Calcd. [M$^-$2PF$_6$]$^{2+}$: 530.17520; found: 530.17584. Anal. (%): Calcd. for ($C_{66}H_{54}F_{12}N_8P_2Ru$)·($H_2O$)$_{0.5}$: C 58.32, H 4.08, N 8.24; found: C 58.17, H 3.83, N 8.66.

X-ray crystallography

Single crystal X-ray diffraction data were collected at 183(1) K on a Rigaku OD SuperNova (Atlas CCD detector) diffractometer for **1** and **2** and on a Rigaku OD Xcalibur (Ruby CCD detector) diffractometer for **3** equipped with Oxford liquid-nitrogen Cryostream coolers. A single wavelength X-ray source from a micro-focus sealed X-ray tube was used with the Cu K$_\alpha$ radiation (λ = 1.54184 Å) for **1** and **2** and with the Mo K$_\alpha$ radiation (λ = 0.71073 Å) for **3**. The selected single crystals were mounted using polybutene oil on a flexible loop fixed on a goniometer head and transferred to the diffractometer. Pre-experiments, data collections, data reductions and analytical absorption corrections[16] were performed with the program suite *CrysAlisPro*.[17] Using *Olex2*,[18] the structures were solved with the SHELXT[19] small molecule

structure solution program and refined with the *SHELXL2018/1* program package[20] by full-matrix least-squares minimization on F^2. The crystal data collections and structure refinement parameters are gathered in Tables S1 and S2. CCDC 1969709 (for **1**), 1969708 (for **2**), and 1969710 (for **3**) contain the supplementary crystallographic data for these compounds, and can be obtained free of charge from the Cambridge Crystallographic Data Centre via www.ccdc.cam.ac.uk/data_request/cif.

In the crystal structure of **1**, solvent molecules of acetonitrile cocrystallized with the main species, one molecule could easily be introduced in the model and freely refined but a second one was observed badly disordered in the asymmetric unit. Consequently, the *PLATON SQUEEZE* tool[21] was used to take the solvent contribution into account to the calculated structure factors: a total number of 92 electrons were found in the P1 unit cell that were considered as 4 solvent molecules of acetonitrile (one per asymmetric unit). In the crystal structure of **2,** the PF_6 counterions occupy three different positions in the asymmetric unit: one general position and two special positions (centers of inversions). The F atoms of one PF_6 are disordered over two sets of positions. Solvent molecules of tetrahydropyran cocrystallized with the main species. They occupy two general positions and are disordered over two sets of positions. Solvent molecules of water are also present in the crystal. The non H atoms of the solvent molecules were isotropically refined. In the crystal structure of **3**, the PF_6 counterions occupy two different positions in the asymmetric unit and in both independent molecules the F atoms are disordered over two sets of positions. There are also two solvent molecules of acetonitrile in the asymmetric unit, one is fully disordered over two sets of positions.

Spectroscopic measurements

The absorption of the samples in cuvettes has been measured with a Lambda 800 UV/VIS Spectrometer (PerkinElmer Instruments) and in 96 well plates with a SpectraMax M2 Spectrometer (Molecular Devices) or with a Varian Cary 8454" UV/Visible spectrophotometer and quartz cuvettes (width 1 cm) at c = 7.5 µM The emission was measured by irradiation of the sample in fluorescence quartz cuvettes (width 1 cm) using a NT342B Nd-YAG pumped optical parametric oscillator (Ekspla) at 355 nm. Luminescence was focused and collected at right angle to the excitation pathway and directed to a Princeton Instruments Acton SP-2300i monochromator. As a detector a XPI-Max 4 CCD camera (Princeton Instruments) has been used.

Lifetime measurements

For the determination of the lifetimes, the samples were prepared in an air saturated and in a degassed CH_3CN solution with an absorbance of 0.1 at 355 nm. This solution was irradiated in fluorescence quartz cuvettes (width 1 cm) using a NT342B Nd-YAG pumped optical parametric oscillator (Ekspla) at 355 nm. The emission signal was focused and collected at right angle to the excitation pathway and directed to a Princeton Instruments Acton SP-2300i monochromator. As a detector a R928 photomultiplier tube (Hamamatsu) was used.

Luminescence quantum yield measurements

For the determination of the luminescence quantum yield, the samples were prepared in an CH_3CN solution with an absorbance of 0.1 at 355 nm. This solution was irradiated in fluorescence quartz cuvettes (width 1 cm) using a NT342B OPO pulse laser Nd-YAG pumped optical parametric oscillator (Ekspla) at 355 nm. The emission signal was focused and collected at right angle to the excitation pathway and directed to a Princeton Instruments Acton SP-2300i monochromator. As detector a XPI-Max 4 CCD camera (Princeton Instruments) was used. The luminescence quantum yields were determined by comparison with the reference $[Ru(bipy)_3]Cl_2$ in CH_3CN ($\Phi_{em} = 0.059$)[22] applying the following formula :

$$\Phi_{em,sample} = \Phi_{em,reference} * \frac{F_{reference}}{F_{sample}} * \frac{I_{sample}}{I_{reference}} * \left(\frac{n_{sample}}{n_{reference}}\right)^2$$

$$F = 1 - 10^{-A}$$

Φ_{em} = luminescence quantum yield, F = fraction of light absorbed, I = integrated emission intensities, n = refractive index, A = absorbance of the sample at irradiation wavelength

Singlet oxygen measurements

- direct evaluation

The samples were prepared in an air saturated CH_3CN or D_2O solution with an absorbance of 0.2 at 450 nm. This solution was irradiated in fluorescence quartz cuvettes (width 1 cm) using a mounted M450LP1 LED (Thorlabs) whose irradiation, centred at 450 nm, has been focused with aspheric condenser lenses. The intensity of the irradiation has been varied using a T-Cube LED Driver (Thorlabs) and measured with an optical power and energy meter. The emission signal was focused and collected at right angle to the excitation pathway and directed to a Princeton Instruments Acton SP-2300i monochromator. A longpass glass filter was placed in

front of the monochromator entrance slit to cut off light at wavelengths shorter than 850 nm. The slits for detection were fully open. As a detector an EO-817L IR-sensitive liquid nitrogen cooled germanium diode detector (North Coast Scientific Corp.) has been used. The singlet oxygen phosphorescence at 1270 nm was measured by recording spectra from 1100 to 1400 nm. For the data analysis, the singlet oxygen luminescence peaks at different irradiation intensities were integrated. The resulting areas were plotted against the percentage of the irradiation intensity and the slope of the linear regression calculated. The absorbance of the sample was corrected with an absorbance correction factor. As reference for the measurement in an CH_3CN solution phenalenone ($\Phi_{phenaleone} = 0.95$)[23] and for the measurement in a D2O solution $[Ru(bipy)_3]Cl_2$ ($\Phi_{Ru(bipy)_3Cl_2} = 0.22$)[24] was used and the singlet oxygen quantum yields were calculated using the following formula:

$$\Phi_{sample} = \Phi_{reference} \times \frac{S_{sample}}{S_{reference}} \times \frac{I_{reference}}{I_{sample}}$$

$$I = I_0 \times (1 - 10^{-A})$$

Φ = singlet oxygen quantum yield, S = slope of the linear regression of the plot of the areas of the singlet oxygen luminescence peaks against the irradiation intensity, I = absorbance correction factor, I_0 = light intensity of the irradiation source, A = absorbance of the sample at irradiation wavelength.

- indirect evaluation

For the measurement in CH_3CN: The samples were prepared in an air-saturated CH_3CN solution containing the complex with an absorbance of 0.1 at the irradiation wavelength, *N*,*N*-dimethyl-4-nitrosoaniline aniline (RNO, 24 µM) and imidazole (12 mM). For the measurement in PBS buffer: The samples were prepared in an air-saturated PBS solution containing the complex with an absorbance of 0.1 at the irradiation wavelength, *N*,*N*-dimethyl-4-nitrosoaniline aniline (RNO, 20 µM) and histidine (10 mM). The samples were irradiated on 96 well plates with an Atlas Photonics LUMOS BIO irradiator for different times. The absorbance of the samples was measured during these time intervals with a SpectraMax M2 Microplate Reader (Molecular Devices). The difference in absorbance (A_0-A) at 420 nm for the CH_3CN solution or at 440 nm a PBS buffer solution was calculated and plotted against the irradiation times. From the plot the slope of the linear regression was calculated as well as the absorbance correction factor determined. The singlet oxygen quantum yields were calculated using the same formulas as used for the direct evaluation.

Stability in DMSO

The stability of the complexes in DMSO was determined by ^{1}H-NMR spectroscopy. The complexes were dissolved in 0.7 mL DMSO-d_6 [2 mg/mL] and the filled tube stored at room temperature in the dark. A spectrum was measured directly after preparing the solutions and after 1, 2 and 7 days.

Stability in human plasma

The stability of the complexes was evaluated with Caffeine as an internal standard, which has already shown to be suitable for these experiments.[25] The pooled human plasma was obtained from Biowest and caffeine from TCI Chemicals. Stock Solutions of the compounds (40 µM) and caffeine (40 or 20 µM) were prepared in DMSO. One aliquot of the solutions was added to 975 µL of human plasma to a total volume of 1000 µL. Final concentrations of the compounds of 0.5 µM and caffeine of 0.5 or 0.25 µM were achieved. The resulting solution was incubated for 4 h, 12 h, 24 h and 48 h at 37 °C with continuous gentle shaking (ca. 300 rpm). The reaction was stopped after the incubation time by addition of 2 mL of methanol. The mixture was centrifuged for 45 min at 650 g at 4 °C. The methanolic solution was filtered through a 0.2 µm membrane filter. The solvent was evaporated under reduced pressure and the residue was dissolved in 1:1 (v/v) CH_3CN/ H_2O 0.1 % TFA solution. The solution was filtered through a 0.2 µm membrane filter and analysed using a HPLC System. For analytic HPLC the following system has been used: 2 x Agilent G1361 1260 Prep Pump system with Agilent G7115A 1260 DAD WR Detector equipped with an Agilent Pursuit XRs 5C18 (100 Å, C18 5 µm 250 × 4.6 mm) Column and an Agilent G1364B 1260-FC fraction collector. The flow rate was 1 mL/min and the chromatogram was detected at 250 nm. In this study, the chromatograms were recorded using two different methods. Method M1: The solvents (HPLC grade) were millipore water (0.1 % TFA, solvent A) and acetonitrile (solvent B). 0-3 minutes: isocratic 95 % A (5 % B); 3-17 minutes: linear gradient from 95 % A (5 % B) to 0 % A (100 % B); 17-23 minutes: isocratic 0 % A (100% B). Method M2: The solvents (HPLC grade) were millipore water (0.1 % TFA, solvent A) and acetonitrile (0.1 % TFA, solvent B). 0-3 minutes: isocratic 95 % A (5 % B); 3-17 minutes: linear gradient from 95 % A (5 % B) to 0 % A (100 % B); 17-23 minutes: isocratic 0 % A (100 % B).

Photostability

The samples were prepared in an air saturated CH_3CN solution with an absorbance of about 0.5 at 450 nm. To measure the photostability, the samples were irradiated at 450 nm in 96 well plates with an Atlas Photonics LUMOS BIO irradiator during time intervals from 0-10 min. The absorbance spectrum from 350-700 nm was recorded with a SpectraMax M2 Microplate Reader (Molecular Devices) after each time interval and compared. As a positive control $[Ru(bipy)_3]Cl_2$ and as a negative control Protoporphyrin IX has been used.

Distribution coefficient

The lipophilicity of a complex was determined by measuring its distribution coefficient between the PBS and Octanol phase by using the "shake-flask" method. For this technique, the used phases were previously saturated in each other. The complex was dissolved in the phase (A) with its major presence with an absorbance of about 0.5 at 450 nm. This solution was then mixed with an equal volume of the other phase (B) at 80 rpm for 8 h with an Invitrogen sample mixer and then equilibrated overnight. The phase A was then carefully separated from phase B. The amount of the complex before and after the sample mixing was determined by UV/Vis spectroscopy at 450 nm using a SpectraMax M2 Microplate Reader (Molecular Devices). The evaluation of the complexes was repeated three times and the ratio between the organic and aqueous phase calculated.

Cell culture

HeLa and CT-26 cell lines were cultured in DMEM media (Gibco, Life Technologies, USA) supplemented with 10 % of fetal calf serum (Gibco). U87 and U373 cell lines were cultured in MEM media with addition of 1 % of MEM NEAA (non-essential amino acids) (Gibco) and 10 % of fetal calf serum. RPE-1 cells were cultured in DMEM/F-12 (Gibco) supplemented with 10 % of fetal calf serum. All cell lines were complemented with 100 U/mL penicillin-streptomycin mixture (Gibco) and maintained in humidified atmosphere at 37 °C and 5 % of CO_2.

Cellular uptake

The cellular uptake of the complex was investigated by the determination of the Ru content inside the cells. The complex with a final concentration of 25 µM (2% DMSO, *v*%) was incubated for 4 h at 37 °C on a cell culture dish with a density of ca. $5 \cdot 10^6$ cells in 10 mL of media. After this time, the media was removed and the cells were washed with cell media. The

cells were trypsinised, harvested, centrifuged and resuspended. The number of cells on each dish was accurately counted. Each sample was the digested using a 60% HNO_3 solution for three days. The acid was removed and the residue dissolved in 2% HCl in water. The Ru content was determined using an ICP-MS apparatus and comparing the results with the Ru references. The Ru content was then associated with the number of cells.

(Photo-)cytotoxicity

Dark and light cytotoxicity of the the Ru(II) complexes was assesed by fluorometric cell viability assay using resazurin (ACROS Organics). For dark and light cytotoxicity, cells were seeded in triplicates in 96 well plates at a density of 4000 cells per well in 100 µL, 24 h prior to treatment. The medium was then replaced with increasing concentration of the tested complexes and cells were incubated for 4 h. Medium was then replaced for fresh complete medium. Cells used for light cytotoxicity experiment were exposed to: 480 nm light for 10 min, 510 nm for 40 min, 540 for 60 min or 595 nm for 120 min in a 96-well plate using a LUMOS-BIO photoreactor (Atlas Photonics). Each well was individually illuminated with a LED at constant current. After irradiation cells were kept for another 44 h in the incubator and the medium was replaced by fresh complete medium containing resazurin (0.2 mg mL^{-1} final concentration). After 4 h incubation at 37 °C, the fluorescence signal of the resorufin product was read by SpectraMax M5 mictroplate reader (ex: 540 nm em: 590 nm). IC_{50} values were calculated using GraphPad Prism software.

Cellular localisation

HeLa cells were grown on the 12 mm Menzel–Gläser coverslips in 2 ml of complete medium at a density of 1.3 x 10^5 cells per ml. Cells were then treated with the compounds (IC_{50} concentration in the dark) for 2 h, with NucBlue (2 drops per 1 ml of media) for the last 25 min and with 100 nm Mitotracker Green FM for the last 15 min. HeLa cells were then fixed with paraformaldehyde solution in PBS (4%) and mounted on glass slides using Prolong Glass Antifade Mountant. Leica SP8 confocal microscope was used to analyse the samples. Ru compounds were excited at 488 nm and emission above 650nm was recorded.

*Time dependent localisation of complex **6***

HeLa cells were grown on the 12 mm Menzel–Gläser coverslips in 2 ml of complete medium at a density of 1.3 x 10^5 cells per ml. Cells were then treated with the complex 6 (14 µM) for 5 min, 10 min, 30 min and 2h. Cells were then co-stained with NucBlue (2 drops per 1 ml of

media) for the last 25 min and with 100 nm Mitotracker Green FM for the last 15 min. HeLa cells were then fixed and images were taken on Leica SP8 confocal microscope.

Indirect Immunofluorescence

HeLa cells were grown on the 12 mm Menzel–Gläser coverslips in 2 ml of complete medium at a density of 1.3 x 10^5 cells per ml. Cells were then treated with the complex 6 (14 μM) for 2h. Cells were co-stained with NucBlue (2 drops per 1 ml of media) for the last 25 min and with 100 nm Mitotracker Green FM for the last 15 min. HeLa cells were then fixed with paraformaldehyde solution in PBS (4%). Fixed cells were then incubated in blocking solution (0.2% BSA, 0,05 % Saponin in PBS) for 15 min at RT, and incubated with indicated primary antibodies for 1 h, anti-GM130 (BD Biosciences, catalog number 610823, batch 4324839) anti-TGN46 (AbD Serotec, AHP500), anti-KDEL (Santa Cruz Biotechnology, catalog number sc-58774) and anti-LAMP antibodies (BD Biosciences) were used at 1:1000, 1:1000. 1:50 and 1:3000 dilution, respectively and detected using Alexa 488 conjugated secondary antibodies (Jackson ImmunoResearch Laboratory) at 1:400 dilution. Coverslips were mounted on glass slides using Prolong Glass Antifade Mountant. Leica SP8 confocal microscope was used to analyse the samples. Ru compounds were excited at 488 nm and emission above 650nm was recorded. Images were recorded in Cellular and Molecular Imaging Technical Platform, INSERM UMS 025 - CNRS UMS 3612, Faculty of Pharmacy of Paris, Paris Descartes University, Paris, France. Colocalisation values were calculated using Fiji software.[26]

Seahorse mito stress test

CT-26 cells were seeded in Seahorse XFe96 well plate at density of 30 000 cells per well in 80 μl. After 24 h cells were treated with 1 μM concentration of: complex **6,** cisplatin or 5-ALA according to the plate arrangement (Figure S53). After 4 h incubation media was exchanged for fresh complete media and chosen wells were irradiated for 2 h at 595 nm using a LUMOS-BIO photoreactor (Atlas Photonics). Each well was individually illuminated with a LED at constant current. Wells that were not irradiated were covered with aluminium foil. After irradiation regular media was removed and the cells were washed thrice using bicarbonate and serum free DMEM, supplemented with glucose, 1.8 mg/ mL; 1% glutamine and 1% sodium pyruvate and incubated in a non-CO_2 incubator at 37 °C for 1 h. Mito Stress assay was run using Oligomycin, 1 μM, FCCP 1 μM and mixture of Antimycin-A/ Rotenone 1 μM each in ports A, B and C respectively using Seahorse XFe96 Extracellular Flux Analyzer.

Seahorse glycolysis stress test

CT-26 cells were seeded in Seahorse XFe96 well plate at density of 30 000 cells per well in 80 µl. After 24 h cells were treated with 1 µM concentration of: complex **6,** cisplatin or 5-ALA according to the plate arrangement (Figure S53). After 4 h incubation media was exchanged for fresh complete media and chosen wells were irradiated for 2 h at 595 nm using a LUMOS-BIO photoreactor (Atlas Photonics). Each well was individually illuminated with a LED at constant current. Wells that were not irradiated were covered with aluminium foil. After irradiation regular media was removed and the cells were washed thrice using bicarbonate and serum free DMEM and incubated in a non-CO_2 incubator at 37 °C for 1 h. Glycolytic stress test was run using glucose, 10 mM, Oligomycin, 1 µM and 2-Deoxyglucose, 50 mM in ports A, B and C respectively using Seahorse XFe96 Extracellular Flux Analyzer.

Generation of 3D HeLa MCTS

HeLa cells were seeded at a density of 5000 cells per well in 200 µL in low attachment round bottom plates (Corning 4515). The single cells would generate MCTS approximately 400 µm in diameter at day 4 at. Plates were kept in the incubator at 37 °C with 5 % CO_2.

(Photo-)cytotoxicity in 3D HeLa MCTSs

HeLa MCTSs after 4 days of growing at 37 °C and 5 % CO_2 were treated by replacing half of the medium in the well by the treatment solutions. For untreated reference MCTS, half of the medium was replaced by fresh medium only. For dark treatment, the cells were treated with increasing concentration of compounds for 24 h. Then medium was removed and replaced by fresh culture medium followed by 44 h incubation in the dark. For phototoxicity treatment, cells were also treated for 24 h with increasing concentration of compounds in the dark. Then medium was removed and replaced by fresh culture medium prior to 2 h of irradiation at 595 nm in using a LUMOS-BIO photoreactor (Atlas Photonics). Each well was individually illuminated with a LED at constant current. Plates were incubated for 44 h. The cytotoxicity was measured using CellTiter-Glo Cell viability kit (Promega, USA).

SUPPORTING FIGURES AND TABLES

Table S1. Cartesian coordinates of the optimized structure of complex **1**.

	X	Y	Z
C	-0.55825800	-1.96095500	2.11992700
C	-1.32520200	-2.95947100	2.73615900
C	-2.57829600	-3.25637400	2.24465400
C	-3.06351800	-2.54957200	1.12647700
C	-4.34971300	-2.77696100	0.53919300
C	-4.76366600	-2.06185400	-0.54228300
C	-3.92623100	-1.06012200	-1.13032600
C	-4.29645200	-0.29247000	-2.25201600
C	-3.41537600	0.64568400	-2.74488300
C	-2.17012700	0.81945000	-2.12553800
C	-2.65677500	-0.81781200	-0.56873200
C	-2.22376500	-1.56600500	0.56718600
C	2.17016700	0.81998000	2.12493100
C	3.41540600	0.64639700	2.74433400
C	4.29647000	-0.29192300	2.25176300
C	3.92622600	-1.05989200	1.13031100
C	4.76365600	-2.06180800	0.54257700
C	4.34968700	-2.77729400	-0.53863300
C	3.06349400	-2.55009700	-1.12600800
C	2.57828400	-3.25721700	-2.24396500
C	1.32523200	-2.96035700	-2.73563200
C	0.55834500	-1.96157600	-2.11979800
C	2.22376000	-1.56630200	-0.56706400
C	2.65675600	-0.81777000	0.56865400
Ru	0.00000600	0.22859500	-0.00022700
N	-0.99051300	-1.27662700	1.06515800
N	0.99057200	-1.27692700	-1.06521200
N	1.79285000	0.10923100	1.06602700
N	-1.79284000	0.10902500	-1.06640500
C	-0.44617000	3.06821300	0.58482200
C	-0.92736500	4.22724500	1.19106300
C	-1.76280900	4.12552500	2.29500100
C	-2.10011900	2.86312400	2.76981300
C	-1.58958200	1.74883800	2.12081700

N	-0.78172800	1.84151000	1.05500000
C	0.44577800	3.06833800	-0.58496600
C	0.92665100	4.22749500	-1.19122600
C	1.76249300	4.12600500	-2.29488000
C	2.10055300	2.86368500	-2.76939100
C	1.59016100	1.74927200	-2.12050900
N	0.78185400	1.84172300	-1.05501100
H	0.42737700	-1.70452600	2.49214500
H	-0.91820400	-3.48203200	3.59416400
H	-3.19246400	-4.02400000	2.70531200
H	-4.99091900	-3.53494500	0.97817000
H	-5.74040200	-2.23999000	-0.98131900
H	-5.26612700	-0.44670400	-2.71513600
H	-3.66460500	1.25466200	-3.60622700
H	-1.46034500	1.54863800	-2.49979900
H	1.46044700	1.54933800	2.49896400
H	3.66460000	1.25561600	3.60551800
H	5.26612700	-0.44607100	2.71494300
H	5.74039300	-2.23979800	0.98167400
H	4.99088400	-3.53545400	-0.97732300
H	3.19236900	-4.02509300	-2.70431500
H	0.91824800	-3.48322900	-3.59345700
H	-0.42724300	-1.70521600	-2.49216800
H	-0.65585400	5.20236000	0.80614600
H	-2.14396300	5.02035900	2.77520200
H	-2.74834400	2.73302700	3.62865400
H	-1.82296300	0.74556400	2.45707300
H	0.65454100	5.20253300	-0.80652900
H	2.14336700	5.02094900	-2.77510000
H	2.74927400	2.73376100	-3.62788300
H	1.82399000	0.74603000	-2.45659800
C	-0.55825800	-1.96095500	2.11992700

Table S2. Cartesian coordinates of the optimized structure of complex **2**.

	X	**Y**	**Z**
C	-0.07795000	-2.37011400	2.04174200
C	0.32568500	-3.60818400	2.56061300
C	1.31528700	-4.32403000	1.92216300
C	1.90355100	-3.79521800	0.75601800
C	2.94035400	-4.45376100	0.01953800
C	3.47380500	-3.89001300	-1.09806300
C	3.01386200	-2.62127900	-1.57764400
C	3.52375400	-1.98850100	-2.72878300
C	3.00941000	-0.76736500	-3.10807600
C	1.98774400	-0.17986700	-2.34937000
C	1.99103700	-1.95698000	-0.87205500
C	1.43499600	-2.54604600	0.30320100
C	-1.56193800	-1.78469500	-2.04093000
C	-2.70290000	-2.40839000	-2.56423700
C	-3.91682100	-2.24903100	-1.93155800
C	-3.98555500	-1.46251700	-0.76485100
C	-5.19478500	-1.23175700	-0.03303300

C	-5.20065800	-0.46041000	1.08795300
C	-3.99750700	0.14509900	1.57450900
C	-3.93918300	0.94994600	2.72956400
C	-2.72876200	1.48439400	3.11592000
C	-1.57975800	1.21744900	2.35880200
C	-2.79515500	-0.06740100	0.87056500
C	-2.78949300	-0.87426400	-0.30749800
Ru	-0.01503200	-0.03870600	0.00290600
N	0.45927900	-1.84594200	0.94408400
N	-1.60435600	0.46121700	1.26472800
N	-1.59689100	-1.03364400	-0.94402000
N	1.48548700	-0.75448500	-1.26026800
C	1.50067100	2.41741700	0.53655200
C	2.42028500	3.29933200	1.09947700
C	3.27228800	2.88204500	2.12019800
C	3.15761600	1.55297200	2.53982700
C	2.22400400	0.72332600	1.94523900
N	1.40569800	1.13594600	0.96483800
C	0.56645400	2.78686400	-0.53971200
C	0.50322100	4.05765000	-1.10667100
C	-0.40890400	4.33856700	-2.12228500
C	-1.24015300	3.29281500	-2.53468400
C	-1.12999900	2.05013200	-1.93640200
N	-0.24843700	1.78987300	-0.95969200
C	4.26992100	3.81019400	2.73863800
C	-0.50591700	5.69915200	-2.73788000
H	-0.85122800	-1.78695900	2.52882300
H	-0.14985300	-3.98327900	3.45956300
H	1.64436800	-5.28488300	2.30535500
H	3.29602800	-5.41564000	0.37498400
H	4.26145600	-4.39513300	-1.64839000
H	4.31339100	-2.46417600	-3.30208700
H	3.37626100	-0.25032700	-3.98723400
H	1.56385700	0.77688800	-2.63169300
H	-0.59683400	-1.89347200	-2.52363100
H	-2.61095300	-3.00690200	-3.46313700
H	-4.81443300	-2.72172300	-2.31872100
H	-6.11179700	-1.68614300	-0.39435100
H	-6.12213400	-0.29021100	1.63584300
H	-4.84220000	1.13957100	3.30183200
H	-2.64503500	2.10859500	3.99817600
H	-0.61608700	1.62388300	2.64610800
H	2.47817800	4.32222900	0.74617300
H	3.79053000	1.15908600	3.32862200
H	2.11379600	-0.30878100	2.25742000
H	1.16634900	4.84067500	-0.75845900
H	-1.97288800	3.43801600	-3.32151000
H	-1.75819100	1.22235800	-2.24443200
H	0.30326600	6.35063800	-2.40323800
H	-1.45787400	6.16877300	-2.46884600
H	-0.47506000	5.63420600	-3.82934700
H	5.28477600	3.42546400	2.60120800
H	4.10038400	3.89662000	3.81620100
H	4.21682500	4.80776400	2.29847600

Table S3. Cartesian coordinates of the optimized structure of complex **3**.

	X	Y	Z
C	-2.95990900	1.45739100	1.64568700
C	-3.96399900	2.41394600	1.84886500
C	-4.27762300	3.29701200	0.83843100
C	-3.58135300	3.21976500	-0.38393100
C	-3.82628000	4.08976800	-1.49461600
C	-3.11898000	3.96750300	-2.65083900
C	-2.10802500	2.96383600	-2.79611500
C	-1.34710700	2.78479700	-3.96830200
C	-0.39896700	1.78549600	-4.00844800
C	-0.20846700	0.96578700	-2.88747000
C	-1.84926300	2.09620200	-1.71632800
C	-2.58966500	2.22597200	-0.50312100
C	-0.20847700	-0.96578800	2.88747000
C	-0.39898600	-1.78549300	4.00845000
C	-1.34713200	-2.78478800	3.96830400
C	-2.10804500	-2.96382700	2.79611400
C	-3.11900500	-3.96749000	2.65083700
C	-3.82630000	-4.08975500	1.49461100
C	-3.58136500	-3.21975600	0.38392500
C	-4.27763100	-3.29700200	-0.83844000
C	-3.96400000	-2.41393900	-1.84887400
C	-2.95990700	-1.45738700	-1.64569400
C	-2.58967300	-2.22596700	0.50311600
C	-1.84927500	-2.09619800	1.71632600
Ru	-0.78219500	-0.00000100	-0.00000100
N	-2.28539300	1.36210300	0.50369400
N	-2.28539500	-1.36210000	-0.50369900
N	-0.91194200	-1.11014100	1.76844800
N	-0.91193500	1.11014100	-1.76845000
C	2.05739200	-0.66425700	-0.31634600
C	3.22242900	-1.36150000	-0.62729100
C	3.10534200	-2.60656500	-1.22357200
C	1.85510600	-3.13916700	-1.50235400
C	0.74457800	-2.38206700	-1.16110100
N	0.83186300	-1.17644100	-0.58315100
C	2.05739200	0.66425200	0.31634900
C	3.22243100	1.36149300	0.62729600
C	3.10534500	2.60655700	1.22357700
C	1.85511000	3.13916200	1.50235700
C	0.74458000	2.38206400	1.16110300
N	0.83186400	1.17643700	0.58315200
Br	4.69898900	-3.60306300	-1.66699600
Br	4.69899300	3.60305300	1.66700200
H	-2.69178700	0.75514800	2.42677600
H	-4.47823500	2.44364400	2.80248500
H	-5.05054800	4.04741600	0.97246100
H	-4.59117500	4.85348300	-1.39384900
H	-3.31075100	4.63153800	-3.48778000
H	-1.51426600	3.43141700	-4.82430800
H	0.20512100	1.61696300	-4.89245600

H	0.52832200	0.17060800	-2.89958300
H	0.52831700	-0.17061500	2.89958300
H	0.20509900	-1.61696000	4.89246000
H	-1.51429800	-3.43140400	4.82431100
H	-3.31078200	-4.63152200	3.48777800
H	-4.59119800	-4.85346700	1.39384200
H	-5.05055800	-4.04740400	-0.97247100
H	-4.47823300	-2.44363600	-2.80249600
H	-2.69178100	-0.75514500	-2.42678200
H	4.19826000	-0.94813400	-0.40953300
H	1.73098500	-4.10889300	-1.96798100
H	-0.25478900	-2.74960300	-1.36091800
H	4.19826100	0.94812500	0.40953900
H	1.73098900	4.10888700	1.96798400
H	-0.25478700	2.74960100	1.36091800

Table S4. Cartesian coordinates of the optimized structure of complex **4**.

	X	**Y**	**Z**
C	2.67238300	-1.29449200	1.77240700
C	3.66829400	-2.23527000	2.06874500
C	3.96207400	-3.22620600	1.15710600
C	3.25461300	-3.27192300	-0.06043200
C	3.47848000	-4.26014700	-1.07213300
C	2.75978600	-4.25701700	-2.22773600
C	1.75826000	-3.26312600	-2.47172600
C	0.98542300	-3.20576200	-3.64817800
C	0.04694400	-2.20654200	-3.78866500
C	-0.12090700	-1.26552900	-2.76361800
C	1.52177500	-2.27912000	-1.49133000
C	2.27267400	-2.28462300	-0.27728700
C	-0.09831600	1.26289600	2.76188100
C	0.08174400	2.20148300	3.78705500
C	1.02701200	3.19380800	3.64286000
C	1.79439000	3.24660400	2.46261400
C	2.80188200	4.23339100	2.21432100
C	3.51452400	4.23236700	1.05495600
C	3.27839600	3.24664400	0.04355400
C	3.97906700	3.19687600	-1.17779500
C	3.67322000	2.20887800	-2.08868200
C	2.67232300	1.27484900	-1.78777800
C	2.29053400	2.26623700	0.26470700
C	1.54571200	2.26534300	1.48250200
Ru	0.48295100	-0.00262700	-0.00261300
N	1.98660200	-1.31399600	0.63323400
N	1.99286200	1.29828900	-0.64487400
N	0.61210700	1.28694800	1.63801900
N	0.59490300	-1.29372200	-1.64326600
C	-2.35513600	-0.61135500	0.39803600
C	-3.51390200	-1.25720200	0.81200300
C	-3.42732100	-2.41716800	1.57421600
C	-2.16212100	-2.91588000	1.87827800
C	-1.04478800	-2.22903400	1.42714000

N	-1.12879700	-1.09928700	0.71261600
C	-2.35185800	0.62571100	-0.39537100
C	-3.50706500	1.27388000	-0.81531900
C	-3.41529400	2.44581300	-1.55858300
C	-2.14721200	2.92593700	-1.88071000
C	-1.03344800	2.22707100	-1.43906100
N	-1.12299800	1.10595000	-0.71177000
C	-4.72361200	-3.06995700	1.97700100
C	-4.71105300	3.07928700	-1.99441100
O	-5.74488200	2.42029100	-1.98950000
N	-4.65058500	4.36503200	-2.38758800
N	-4.66264300	-3.94037000	3.00203700
O	-5.75595000	-2.80636500	1.37073300
H	2.42023900	-0.51063600	2.47757800
H	4.19113800	-2.16785700	3.01581700
H	4.72714300	-3.96796400	1.36497800
H	4.23685900	-5.01649400	-0.89601800
H	2.93534300	-5.01107300	-2.98861600
H	1.13555600	-3.94508700	-4.42887700
H	-0.56657100	-2.13073900	-4.67895200
H	-0.84990000	-0.46857000	-2.85466800
H	-0.83323100	0.47155900	2.85513000
H	-0.52780700	2.12941400	4.68037600
H	1.18659300	3.93115600	4.42354500
H	2.98688100	4.98543200	2.97496100
H	4.27741000	4.98338600	0.87558200
H	4.74838900	3.93324100	-1.38918600
H	4.19040700	2.13859600	-3.03864900
H	2.41075900	0.49340200	-2.49222400
H	-4.49803000	-0.88490500	0.55412000
H	-2.01707100	-3.83532300	2.43427100
H	-0.04554600	-2.58749300	1.64258900
H	-4.49326200	0.88884000	-0.58576200
H	-1.99471400	3.81085700	-2.48811600
H	-0.03262400	2.56485900	-1.67916900
H	-3.84583700	4.94804300	-2.22977800
H	-5.51422500	4.82025900	-2.64026600
H	-3.86038700	-4.01650800	3.60482100
H	-5.52569400	-4.35443100	3.31935200

Table S5. Cartesian coordinates of the optimized structure of complex **5**.

	X	**Y**	**Z**
C	-3.24699200	1.80178400	1.24947200
C	-4.24267300	2.78782100	1.21960900
C	-4.53541800	3.42499900	0.03277500
C	-3.82645500	3.06811200	-1.13105500
C	-4.04862600	3.66798200	-2.41248700
C	-3.32946400	3.28315900	-3.50201300
C	-2.32874800	2.26321600	-3.40466000
C	-1.55470400	1.82115500	-4.49549700
C	-0.61578700	0.83178800	-4.29552800
C	-0.44949200	0.28160400	-3.01704400

C	-2.09372800	1.65730500	-2.15420100
C	-2.84497400	2.06375900	-1.01031100
C	-0.44301300	-0.28189200	3.01493200
C	-0.60500700	-0.83257000	4.29376000
C	-1.54001300	-1.82527300	4.49550100
C	-2.31449400	-2.27015600	3.40611800
C	-3.31149400	-3.29354900	3.50541200
C	-4.03142600	-3.68085600	2.41727400
C	-3.81380200	-3.08021300	1.13542100
C	-4.52393900	-3.43937100	-0.02698900
C	-4.23590100	-2.80097900	-1.21432200
C	-3.24367300	-1.81152300	-1.24611800
C	-2.83595500	-2.07255500	1.01276100
C	-2.08389500	-1.66353300	2.15518800
Ru	-1.05561300	-0.00134200	-0.00048200
N	-2.55980300	1.44484200	0.16817800
N	-2.55535500	-1.45250200	-0.16622800
N	-1.16230900	-0.67871100	1.96894200
N	-1.16833700	0.67573600	-1.96972000
C	1.79365900	0.72187200	0.16529700
C	2.94540100	1.47369000	0.32610100
C	2.89541500	2.84836400	0.64295000
C	1.59440700	3.38505000	0.78178600
C	0.48992200	2.58134100	0.60853400
N	0.56001800	1.27196800	0.30856300
C	1.79565500	-0.71571200	-0.16923800
C	2.94949600	-1.46395200	-0.33200000
C	2.90317800	-2.83767600	-0.65298800
C	1.60388200	-3.37738700	-0.79490400
C	0.49707200	-2.57781400	-0.61698400
N	0.56361000	-1.26928200	-0.31266500
C	4.11786700	3.58173300	0.79619500
C	4.12782100	-3.56767200	-0.80681400
C	4.19511500	-4.90710700	-1.08585200
C	4.18139400	4.91952200	1.08517600
N	5.29938000	5.64415400	1.23380300
N	5.31438900	-5.62400500	-1.26468600
C	6.59996200	5.02459500	1.09381100
C	5.25299800	7.05779100	1.54452200
C	6.61427800	-4.99759900	-1.15425400
C	5.27215200	-7.06025100	-1.44583000
H	-2.99514900	1.29154900	2.17263000
H	-4.76720900	3.03522600	2.13546000
H	-5.30070900	4.19362200	-0.01523000
H	-4.80585600	4.44146200	-2.49644500
H	-3.50348200	3.74479900	-4.46904300
H	-1.70389800	2.26127600	-5.47673300
H	-0.00055000	0.46713000	-5.11015100
H	0.27996300	-0.49941800	-2.83367100
H	0.28329900	0.50171200	2.83012400
H	0.01039800	-0.46563900	5.10723600
H	-1.68585300	-2.26586200	5.47703200
H	-3.48210700	-3.75570900	4.47280200
H	-4.78586600	-4.45689500	2.50269700

H	-5.28648200	-4.21062500	0.02249400
H	-4.76155000	-3.05000800	-2.12909300
H	-2.99558500	-1.30018900	-2.16968800
H	3.91506000	1.00471400	0.20329400
H	1.42998900	4.42855700	1.02499000
H	-0.50920700	2.98958900	0.71461600
H	3.91785500	-0.99253600	-0.20831800
H	1.44274800	-4.41959100	-1.04573600
H	-0.50095100	-2.98840500	-0.72442000
H	5.03627700	3.01776600	0.66626700
H	5.04450300	-3.00020900	-0.68016000
H	3.28291600	-5.48966600	-1.18517500
H	3.26757100	5.49342300	1.21440600
H	6.72066100	4.58994900	0.09468100
H	6.73790800	4.22980800	1.83632700
H	7.37426900	5.77733600	1.24155000
H	4.21507800	7.38632900	1.61457400
H	5.75146100	7.64283800	0.76384900
H	5.74831600	7.26201000	2.50024400
H	6.68385100	-4.13472000	-1.82524100
H	7.38405000	-5.71700300	-1.43414100
H	6.80782000	-4.65737900	-0.12933300
H	4.23674400	-7.38956200	-1.54452700
H	5.72206400	-7.57804400	-0.59060500
H	5.81749800	-7.34797200	-2.35069400

Table S6. Cartesian coordinates of the optimized structure of complex **6**.

	X	**Y**	**Z**
C	-0.20433800	-1.17647900	-2.17035000
C	-0.83768700	-2.19745200	-2.88108300
C	-2.14772700	-2.55525600	-2.59848900
C	-2.82562400	-1.81031300	-1.59155300
C	-4.19804200	-2.00280500	-1.23596800
C	-4.79827800	-1.25281400	-0.27122500
C	-4.08926500	-0.22937900	0.43408000
C	-4.65964700	0.58031500	1.45798800
C	-3.81925800	1.47587300	2.10313400
C	-2.48188000	1.60417000	1.72416000
C	-2.73076100	-0.02705700	0.11118900
C	-2.10614700	-0.79978900	-0.91914000
C	0.20420800	-1.17670100	2.17037000
C	0.83744300	-2.19788000	2.88091700
C	2.14742600	-2.55578700	2.59822600
C	2.82542100	-1.81071000	1.59146500
C	4.19786000	-2.00320000	1.23596500
C	4.79817800	-1.25310300	0.27135900
C	4.08924000	-0.22958300	-0.43389700
C	4.65971100	0.58018700	-1.45770400
C	3.81938900	1.47588300	-2.10275500
C	2.48200600	1.60420900	-1.72382100
C	2.73073400	-0.02721900	-0.11103600

C	2.10604300	-0.80002500	0.91919100
Ru	0.00002000	1.00417700	0.00010800
N	-0.80906000	-0.49579700	-1.20172100
N	1.94328200	0.88646700	-0.74342000
N	0.80898600	-0.49594900	1.20182400
N	-1.94323900	0.88651600	0.74365000
C	-0.33309400	3.84788000	-0.65614600
C	-0.68410800	5.00726100	-1.34357000
C	-1.31312700	4.93440100	-2.58495800
C	-1.57105400	3.65697700	-3.09169300
C	-1.19826500	2.54107100	-2.36375700
N	-0.58835100	2.62180000	-1.17170100
C	0.33344400	3.84783200	0.65638400
C	0.68459900	5.00717700	1.34381800
C	1.31361300	4.93424500	2.58518800
C	1.57126200	3.65678000	3.09199900
C	1.19835500	2.54092900	2.36405900
N	0.58852700	2.62173200	1.17194900
C	-1.68879800	6.16523500	-3.34905400
C	1.69010700	6.16500400	3.34900100
H	0.82491600	-0.90956800	-2.38243200
H	-0.27621300	-2.73201400	-3.63936400
H	-4.77001500	-2.76145400	-1.75723800
H	-5.83680100	-1.43482700	-0.02066000
H	-4.20273600	2.11552600	2.89031800
H	-1.83054900	2.31694400	2.21726100
H	-0.82500400	-0.90968800	2.38252700
H	0.27592800	-2.73250800	3.63912200
H	4.76979900	-2.76187300	1.75724200
H	5.83673600	-1.43503800	0.02088900
H	4.20292400	2.11562800	-2.88983600
H	1.83073700	2.31707900	-2.21686700
H	-0.46971000	5.97917200	-0.91455900
H	-2.06111100	3.52524800	-4.05076300
H	-1.38408100	1.54090100	-2.73760400
H	0.47025800	5.97911100	0.91483800
H	2.06115900	3.52499700	4.05114500
H	1.38394300	1.54073100	2.73794600
H	1.52118100	7.06976000	2.76214100
H	2.74308900	6.13076400	3.64399700
H	1.09967500	6.23704100	4.26849500
H	-2.73948600	6.12794100	-3.65161400
H	-1.09201100	6.24102500	-4.26417200
H	-1.52692200	7.06950000	-2.75945000
C	6.08425900	0.50396200	-1.84614200
C	6.43095000	0.38449700	-3.19851800
C	7.10336800	0.60773200	-0.88913300
C	7.76736900	0.35301000	-3.58310200
H	5.64807500	0.29762100	-3.94683800
C	8.43872000	0.58488500	-1.27870900
H	6.84922300	0.73662600	0.15901700
C	8.77400100	0.45296200	-2.62473100
H	8.02230200	0.24873600	-4.63344600
H	9.21836100	0.67673600	-0.52853600

H	9.81699300	0.43141300	-2.92625900
C	2.77721700	-3.67179100	3.33586400
C	3.38981300	-4.73553600	2.65898400
C	2.71668100	-3.70072900	4.73534200
C	3.93544100	-5.79983500	3.36982000
H	3.41301300	-4.74291600	1.57305200
C	3.27176800	-4.76207200	5.44273700
H	2.24914500	-2.87774100	5.26868200
C	3.88231400	-5.81358300	4.76216000
H	4.39779300	-6.62279700	2.83314500
H	3.22827600	-4.76644100	6.52771700
H	4.31273600	-6.64317000	5.31506300
C	-6.08420300	0.50413400	1.84642500
C	-6.43087800	0.38386300	3.19872800
C	-7.10330200	0.60874200	0.88949800
C	-7.76729800	0.35236500	3.58332200
H	-5.64799300	0.29638000	3.94696900
C	-8.43864900	0.58587700	1.27909400
H	-6.84916700	0.73837800	-0.15856700
C	-8.77392800	0.45311400	2.62503600
H	-8.02222000	0.24746100	4.63360600
H	-9.21829100	0.67838100	0.52900200
H	-9.81691900	0.43155200	2.92656400
C	-2.77763800	-3.67097600	-3.33643600
C	-3.39106200	-4.73445800	-2.65989200
C	-2.71642300	-3.69993100	-4.73589000
C	-3.93677300	-5.79852600	-3.37100300
H	-3.41492300	-4.74173200	-1.57397900
C	-3.27159100	-4.76103600	-5.44357200
H	-2.24831100	-2.87712300	-5.26900200
C	-3.88291800	-5.81230200	-4.76331500
H	-4.39977400	-6.62127900	-2.83456600
H	-3.22755900	-4.76540700	-6.52853000
H	-4.31340400	-6.64170500	-5.31644300

Table S7. Cartesian coordinates of the optimized structure of complex **7**.

	X	**Y**	**Z**
C	-0.79242200	-1.98975200	2.04237000
C	-1.63210200	-2.95676000	2.59828300
C	-2.85947500	-3.25014500	2.02177900
C	-3.19790600	-2.56234100	0.82163200
C	-4.38992100	-2.80175100	0.06712700
C	-4.66066800	-2.11624900	-1.07750800
C	-3.76177600	-1.12927000	-1.59259700
C	-3.99399800	-0.37741000	-2.77968800
C	-3.06059800	0.59470400	-3.10917100
C	-1.91778100	0.78499800	-2.32985300
C	-2.58111200	-0.86950600	-0.86502200
C	-2.28962900	-1.60032900	0.33120000
C	1.91754400	0.78562200	2.33002000
C	3.06047200	0.59580100	3.10929700
C	3.99438100	-0.37575500	2.77961800

C	3.76258900	-1.12747700	1.59235600
C	4.66205200	-2.11381600	1.07703400
C	4.39165200	-2.79926200	-0.06771800
C	3.19944600	-2.56042800	-0.82210500
C	2.86133100	-3.24826200	-2.02232000
C	1.63374700	-2.95552300	-2.59869300
C	0.79357000	-1.98903500	-2.04261900
C	2.29065000	-1.59900400	-0.33148500
C	2.58176600	-0.86823300	0.86486000
Ru	0.00001000	0.18367700	0.00004700
N	-1.11021300	-1.30780100	0.94633800
N	1.11104600	-1.30703300	-0.94652500
N	1.66347500	0.06386700	1.24287400
N	-1.66333100	0.06318800	-1.24282900
C	-0.50282300	3.03536600	0.54115400
C	-1.03199700	4.18908700	1.09504000
C	-1.99022800	4.14247900	2.12992600
C	-2.35380400	2.84322900	2.55332700
C	-1.79108200	1.73656300	1.95762000
N	-0.88080700	1.80312200	0.96933800
C	0.50120300	3.03578200	-0.54044500
C	1.02969600	4.18992800	-1.09409800
C	1.98791700	4.14408700	-2.12903100
C	2.35226500	2.84513700	-2.55269200
C	1.79021700	1.73802000	-1.95719100
N	0.87991100	1.80385200	-0.96888900
C	-2.51350000	5.36676100	2.66300600
C	2.51041300	5.36878800	-2.66190700
C	3.47075600	5.43497300	-3.63604400
C	-3.47430400	5.43215400	3.63673700
N	-3.96865800	6.54940200	4.19123700
N	3.96433600	6.55265300	-4.19035100
C	-3.50880600	7.85166500	3.75949900
C	-5.09301700	6.50314400	5.10299600
C	3.50407500	7.85454600	-3.75792700
C	5.08799800	6.50725400	-5.10300800
H	0.15541500	-1.74390700	2.50822100
H	-1.32501900	-3.45291400	3.51248100
H	-5.08824600	-3.55234300	0.41843300
H	-5.58083600	-2.31436200	-1.61465400
H	-3.19057100	1.19671900	-4.00185700
H	-1.17432900	1.52577900	-2.60235600
H	1.17368100	1.52594000	2.60266400
H	3.19012700	1.19770200	4.00210700
H	5.58238800	-2.31144700	1.61407100
H	5.09040700	-3.54937900	-0.41918700
H	1.32686900	-3.45175700	-3.51291800
H	-0.15441600	-1.74365700	-2.50841600
H	-0.71067800	5.15748300	0.72881600
H	-3.07279300	2.68270800	3.34863100
H	-2.06667800	0.73848200	2.28028900
H	0.70780700	5.15807200	-0.72770200
H	3.07133800	2.68521600	-3.34803700
H	2.06640500	0.74015600	-2.28002100

H	-2.11439000	6.28401000	2.24140600
H	2.11097900	6.28570400	-2.23988700
H	3.90462000	4.52198900	-4.03586600
H	-3.90792400	4.51882600	4.03603200
H	-3.83249600	8.07292800	2.73452800
H	-2.41587800	7.90276500	3.79724900
H	-3.91405200	8.61364300	4.42591600
H	-5.29800100	5.46888400	5.38360600
H	-5.99458000	6.92380600	4.64158400
H	-4.87042900	7.07350500	6.01037700
H	2.41111200	7.90521300	-3.79528200
H	3.90878200	8.61696900	-4.42416000
H	3.82802600	8.07551200	-2.73297800
H	5.29340300	5.47317400	-5.38397200
H	5.98965600	6.92839300	-4.64222400
H	4.86435200	7.07763800	-6.01011900
C	-5.16755400	-0.59254900	-3.65354800
C	-5.94945300	0.50099700	-4.04841300
C	-5.48500900	-1.86723700	-4.14295300
C	-7.03403500	0.32100800	-4.90073500
H	-5.71464200	1.49175100	-3.66939900
C	-6.56531800	-2.04196700	-5.00212000
H	-4.86739100	-2.71896900	-3.87270000
C	-7.34487600	-0.95026300	-5.37913100
H	-7.63828000	1.17567000	-5.18993600
H	-6.79401700	-3.03315700	-5.38207200
H	-8.19016300	-1.08947600	-6.04645600
C	-3.74978200	-4.24363100	2.65963600
C	-5.08562900	-3.93836700	2.95538300
C	-3.24165000	-5.49649700	3.02714100
C	-5.89485000	-4.87092900	3.59661000
H	-5.48299400	-2.95817700	2.70800900
C	-4.05618100	-6.42944100	3.66065500
H	-2.20903700	-5.74381800	2.79701400
C	-5.38436800	-6.11937500	3.94629500
H	-6.92511600	-4.61817800	3.82859000
H	-3.65253300	-7.40096600	3.92966400
H	-6.01895300	-6.84729000	4.44292100
C	3.75222000	-4.24110600	-2.66037200
C	3.24500300	-5.49441700	-3.02759900
C	5.08772300	-3.93476500	-2.95655800
C	4.06011400	-6.42675600	-3.66126300
H	2.21266100	-5.74255700	-2.79714100
C	5.89751500	-4.86672300	-3.59794300
H	5.48435300	-2.95422000	-2.70940500
C	5.38795900	-6.11562700	-3.94733900
H	3.65718300	-7.39864000	-3.93005100
H	6.92750200	-4.61314500	-3.83026400
H	6.02299100	-6.84307000	-4.44408300
C	5.16800300	-0.59055100	3.65347500
C	5.48587000	-1.86518800	4.14275100
C	5.94951900	0.50321700	4.04846700
C	6.56621900	-2.03964000	5.00192400
H	4.86852700	-2.71709700	3.87241900

C	7.03414400	0.32350400	4.90079600
H	5.71437200	1.49392800	3.66954900
C	7.34540200	-0.94771200	5.37906400
H	6.79524300	-3.03079100	5.38178200
H	7.63809300	1.17834000	5.19010200
H	8.19072100	-1.08671100	6.04639400

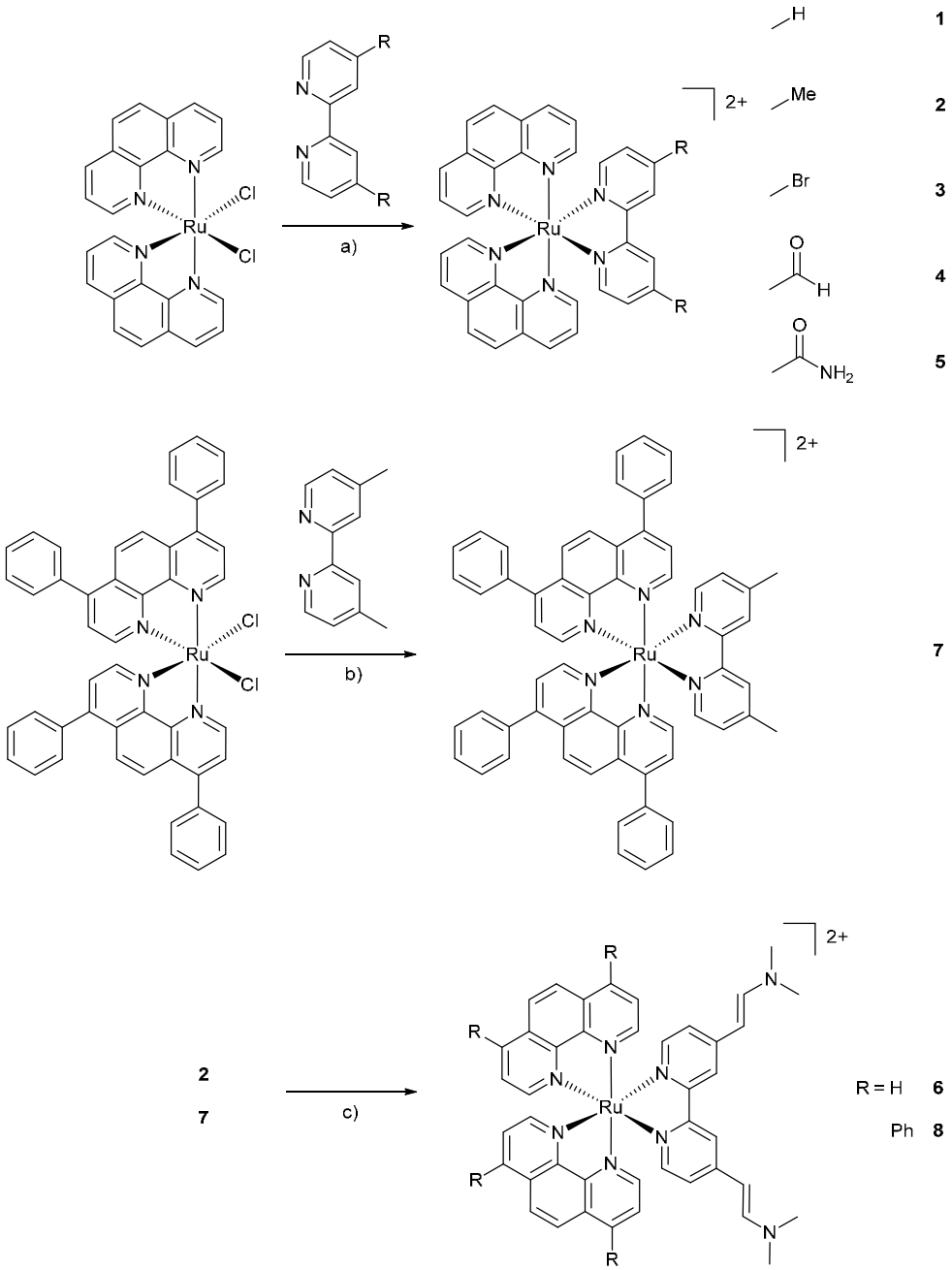

Scheme S1. Synthesis of the desired complexes **1**-**7**. a) EtOH/H_2O (1:1), 18 h reflux under N_2 atmosphere. b) EtOH/H_2O (1:1), 18 h reflux under N_2 atmosphere. c) *tert*-Butoxy bis(dimethylamino)methane, 140 °C, 16 h under N_2 atmosphere.

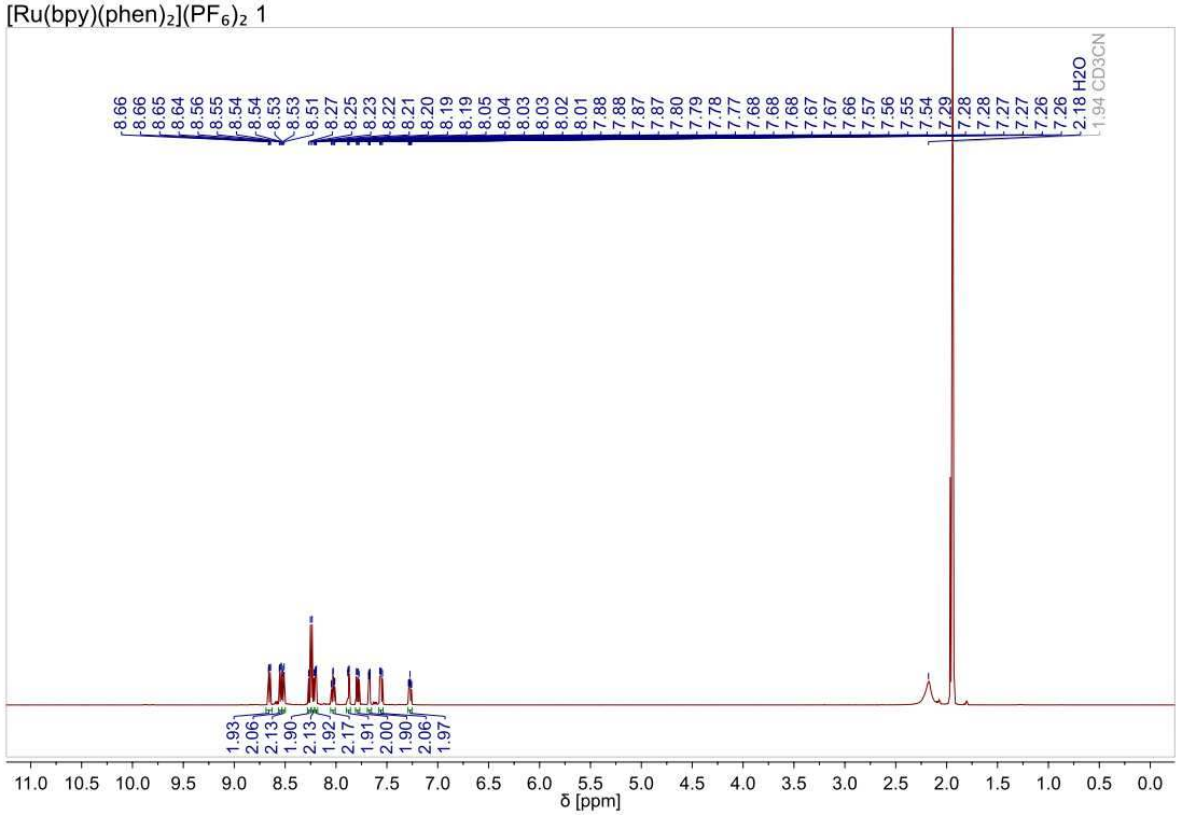

Figure S1. ^{1}H NMR spectrum of **1** in CD_3CN, 500 MHz.

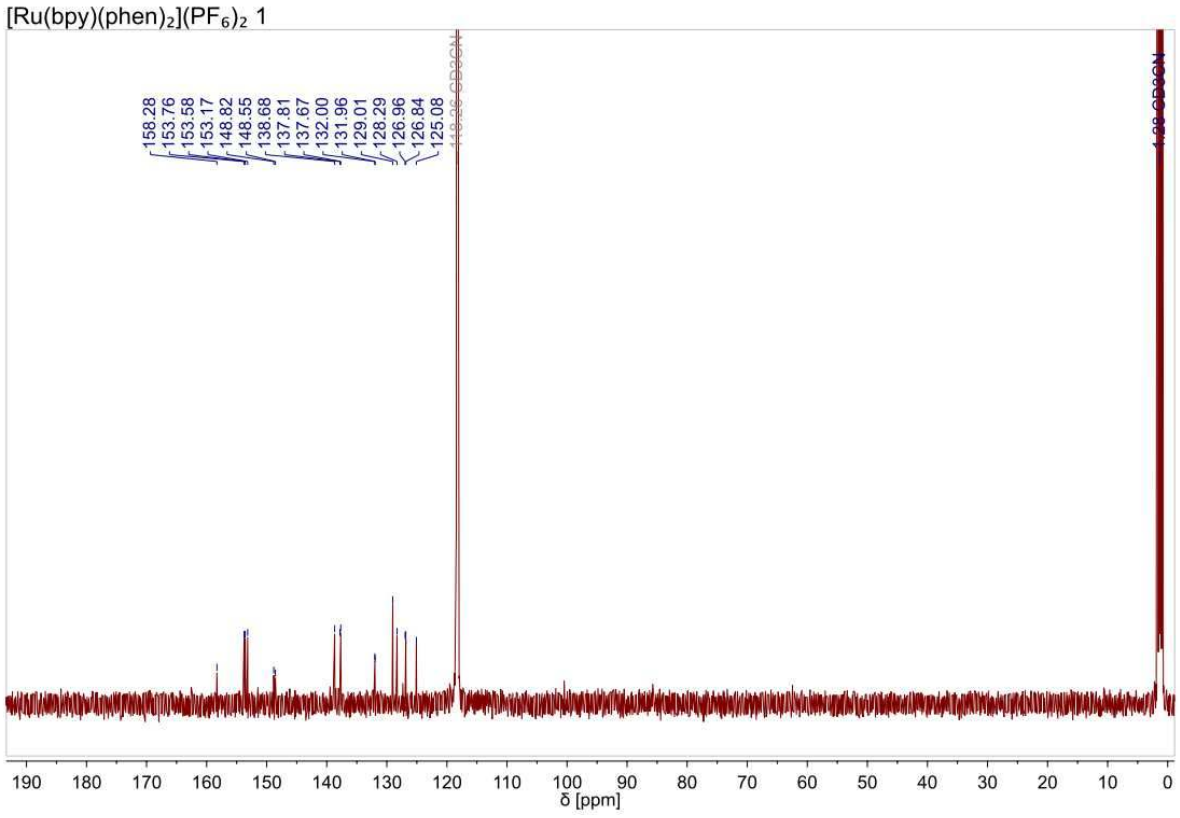

Figure S2. ^{13}C NMR spectrum of **1** in CD_3CN, 125 MHz.

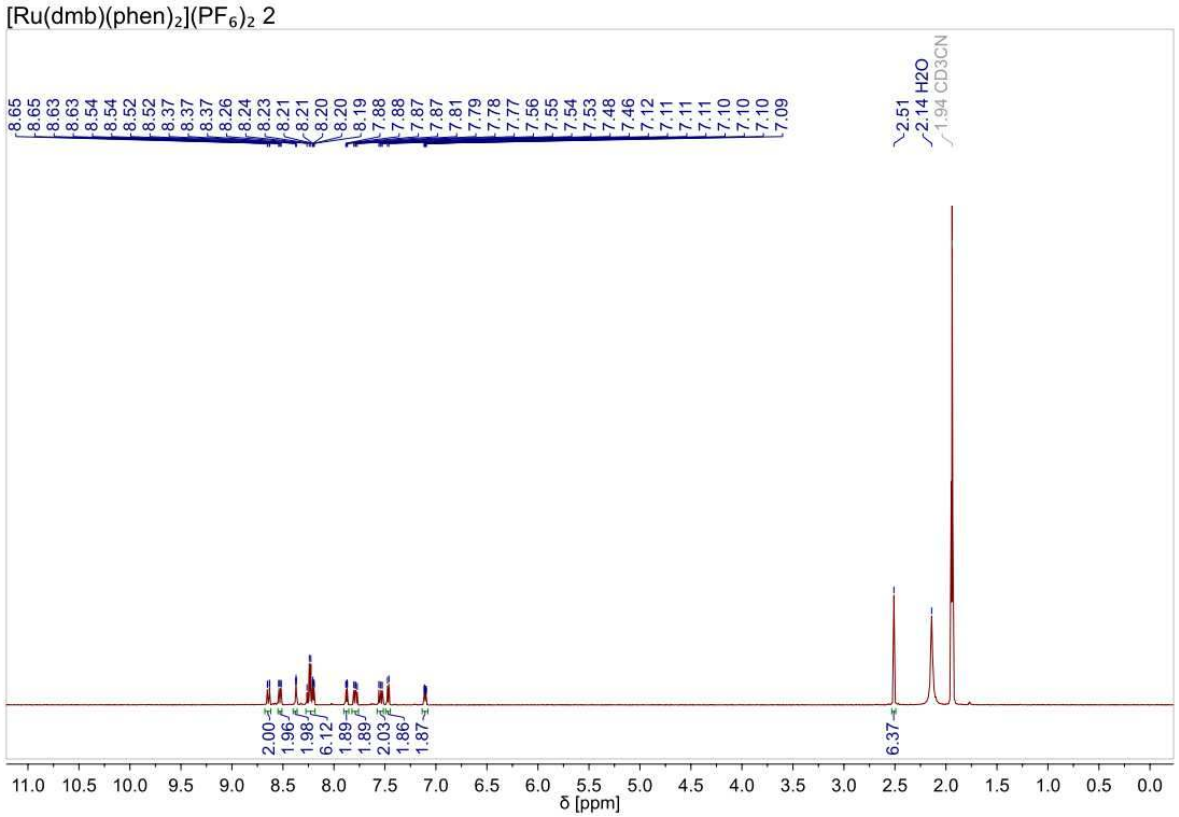

Figure S3. ^{1}H NMR spectrum of **2** in CD_3CN, 400 MHz.

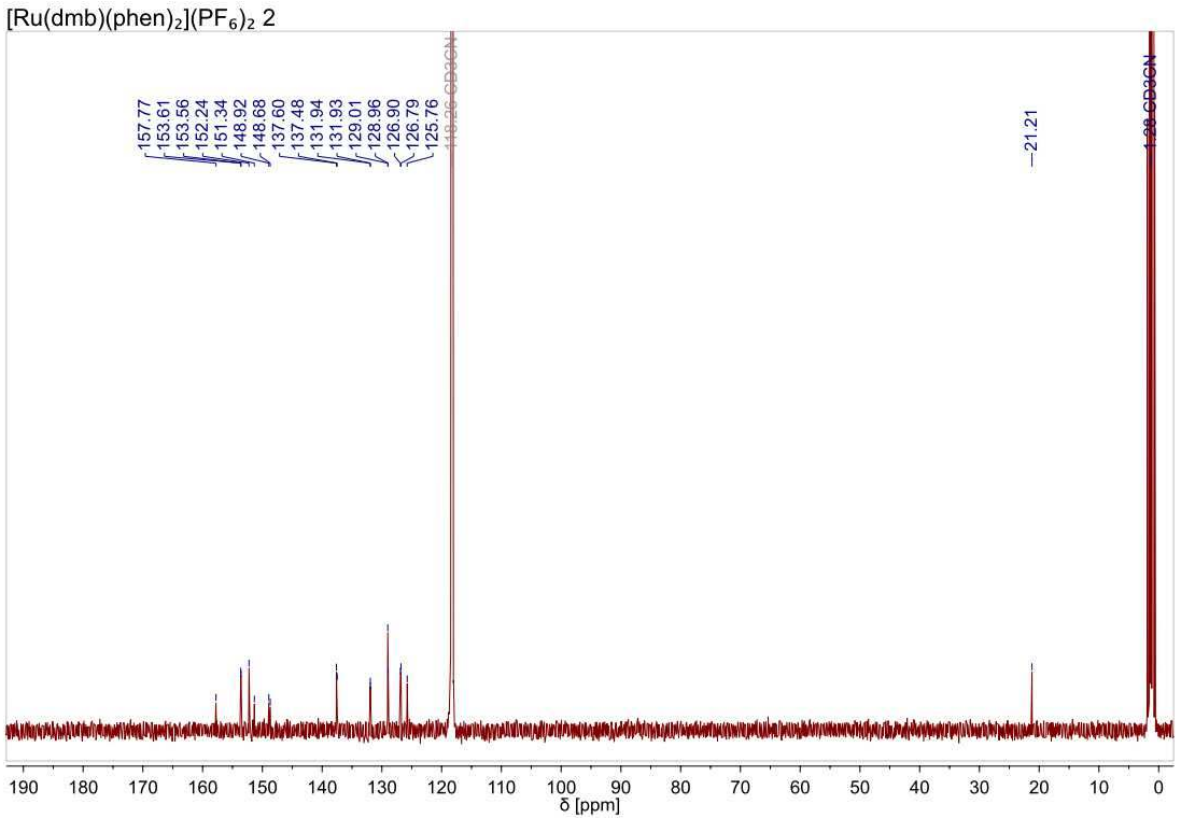

Figure S4. ^{13}C NMR spectrum of **2** in CD_3CN, 100 MHz.

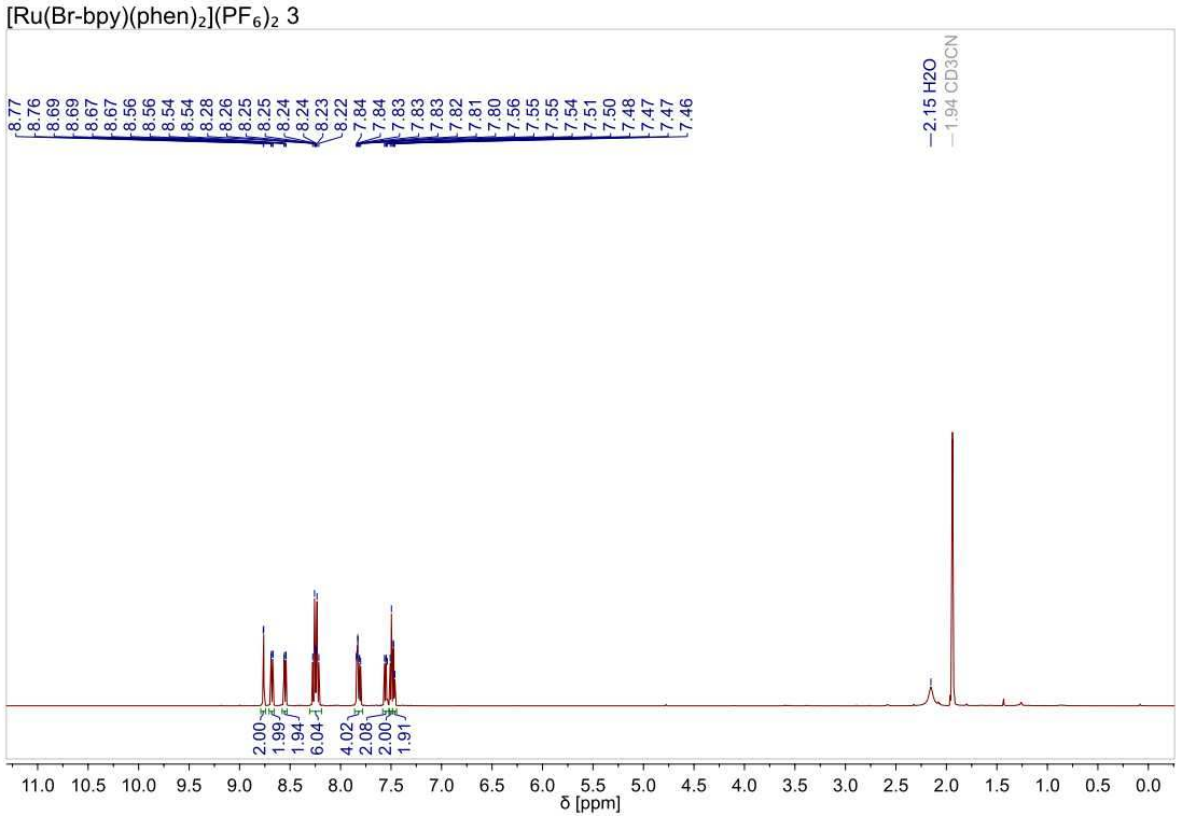

Figure S5. ^{1}H NMR spectrum of **3** in CD_3CN, 500 MHz.

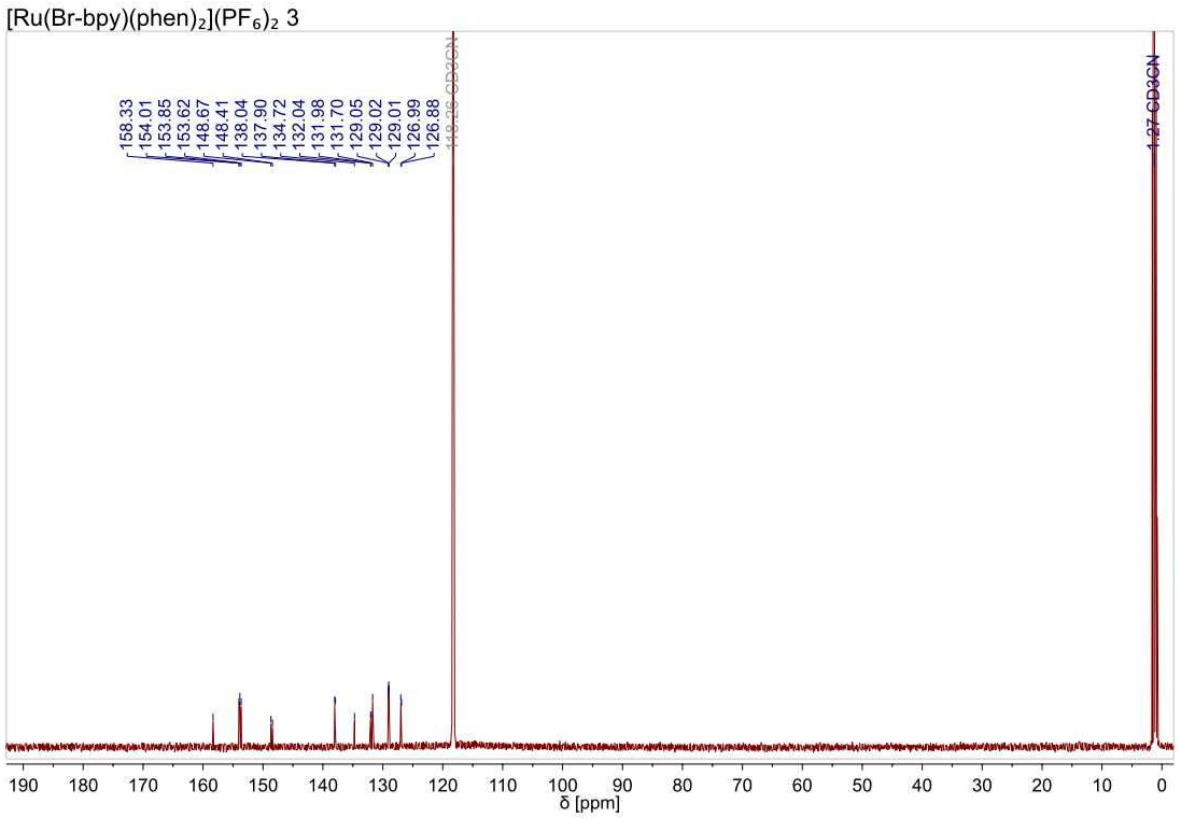

Figure S6. ^{13}C NMR spectrum of **3** in CD_3CN, 125 MHz.

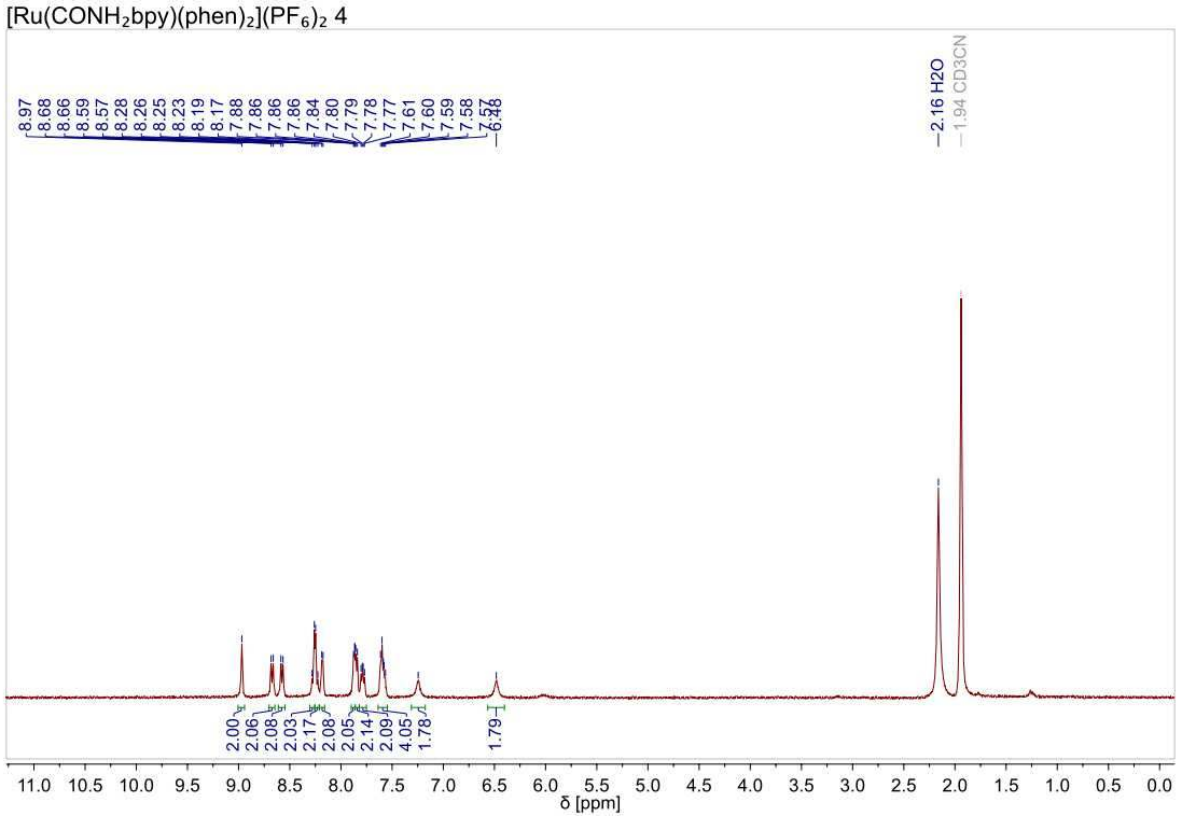

Figure S7. ^{1}H NMR spectrum of **4** in CD_3CN, 400 MHz.

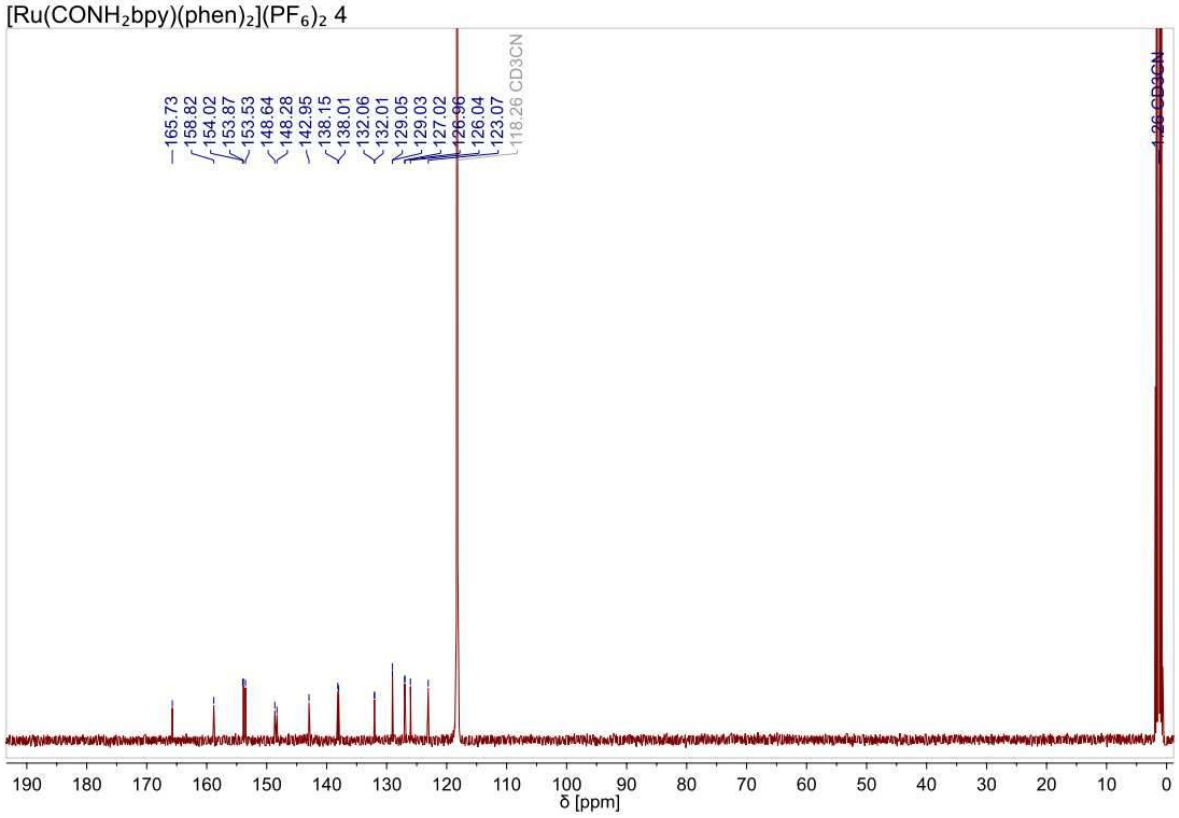

Figure S8. ^{13}C NMR spectrum of **4** in CD_3CN, 100 MHz.

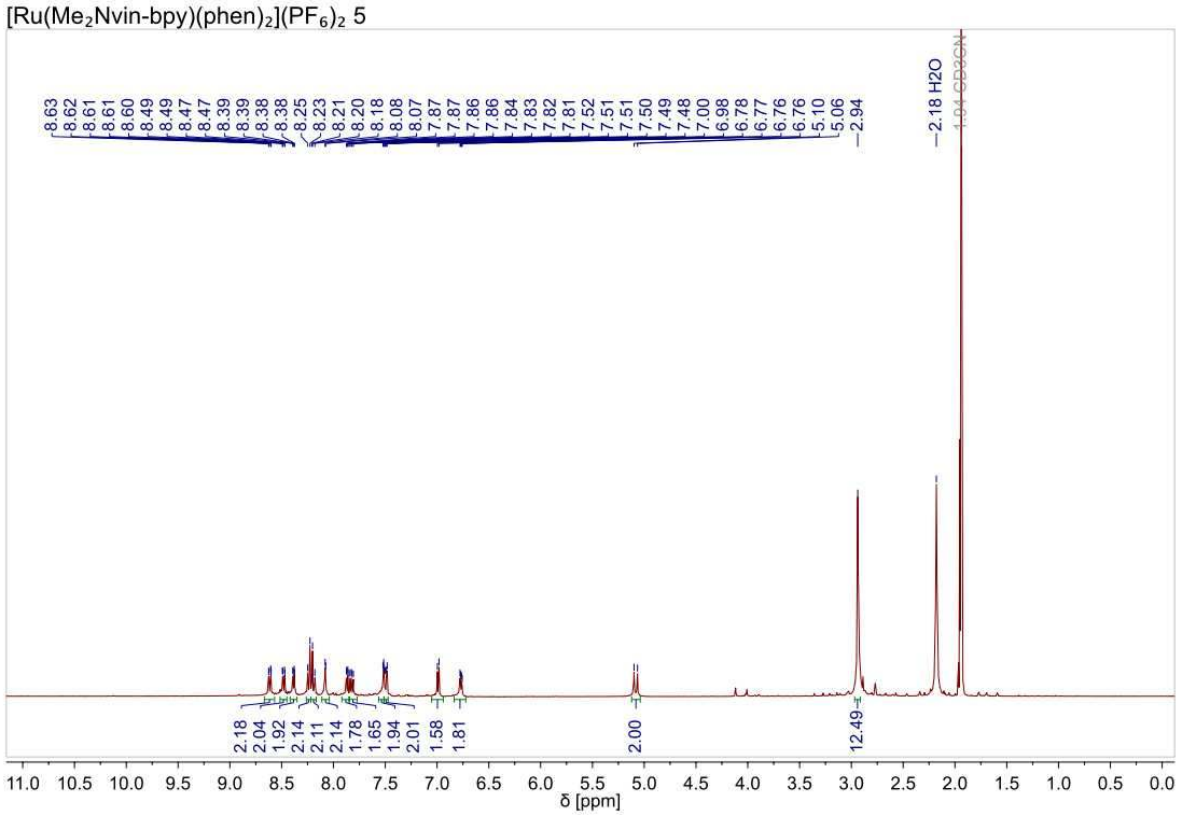

Figure S9. ^{1}H NMR spectrum of **5** in CD_3CN, 400 MHz.

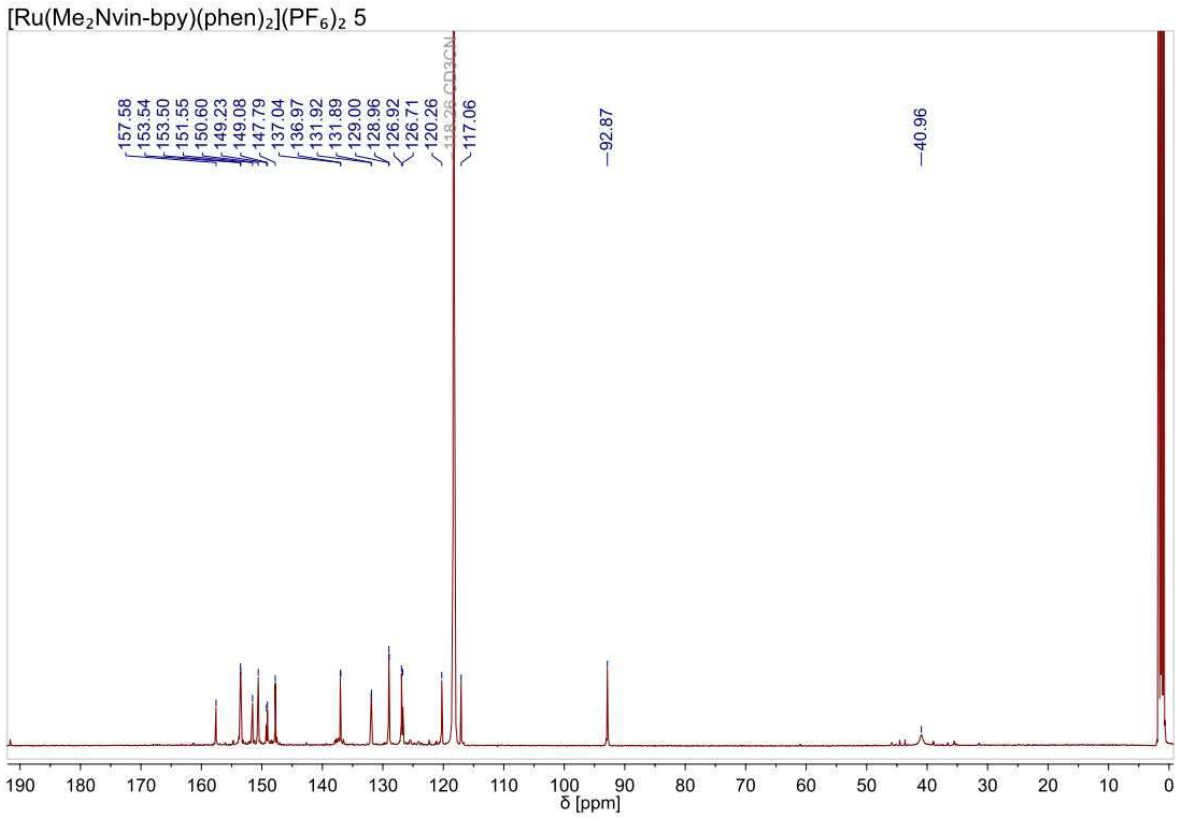

Figure S10. ^{13}C NMR spectrum of **5** in CD_3CN, 125 MHz.

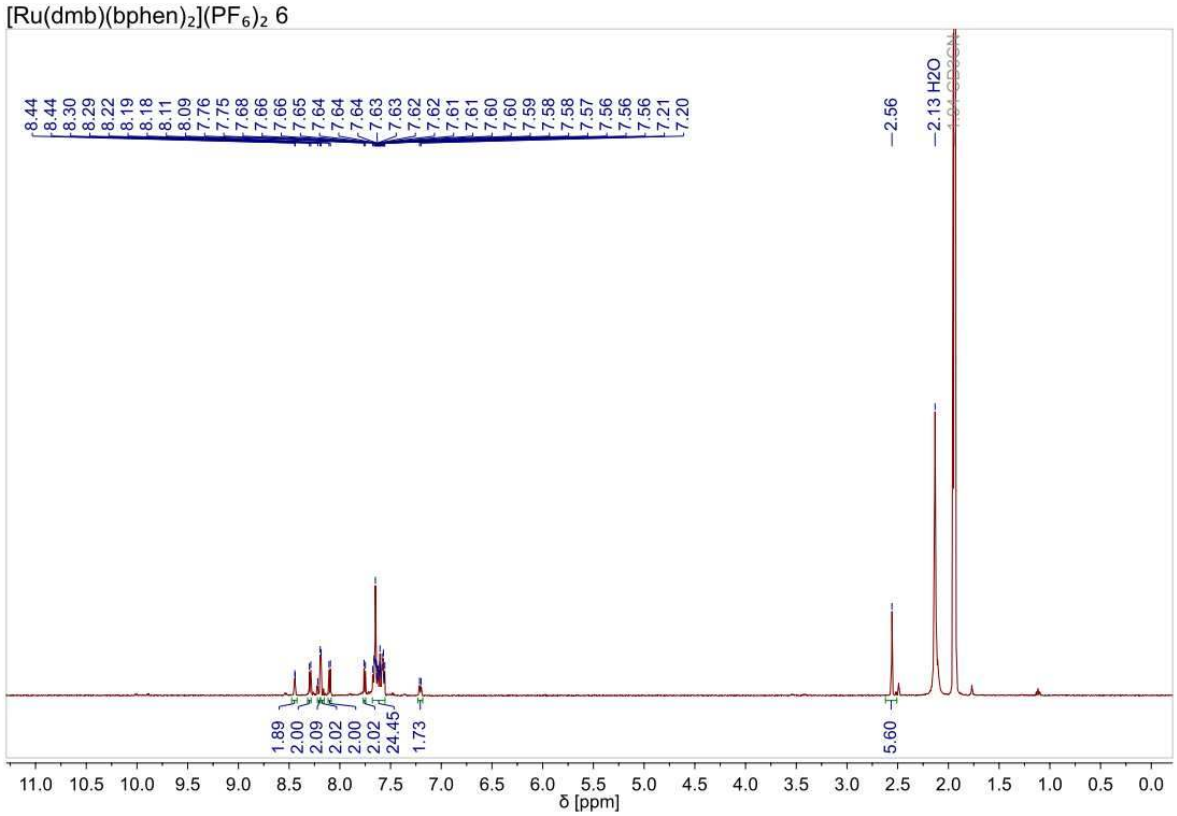

Figure S11. ^{1}H NMR spectrum of **6** in CD_3CN, 400 MHz.

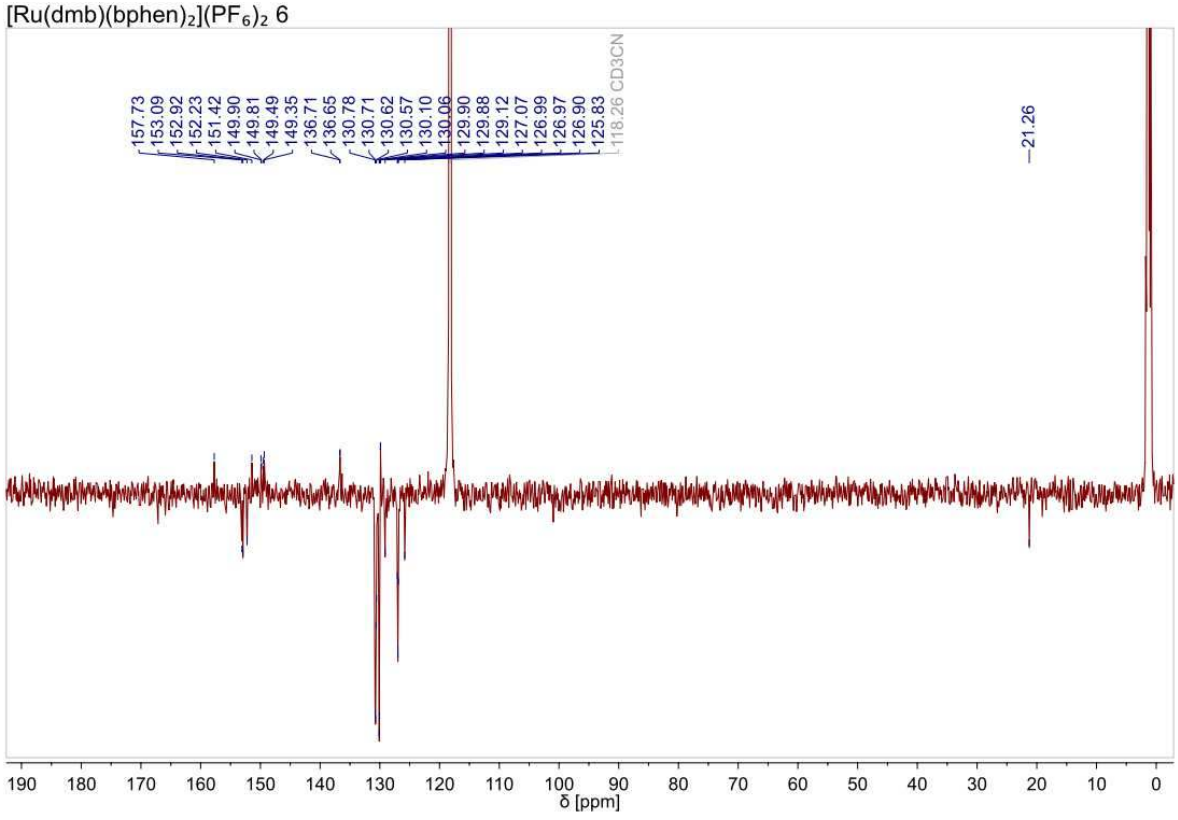

Figure S12. ^{13}C NMR spectrum of **6** in CD_3CN, 125 MHz.

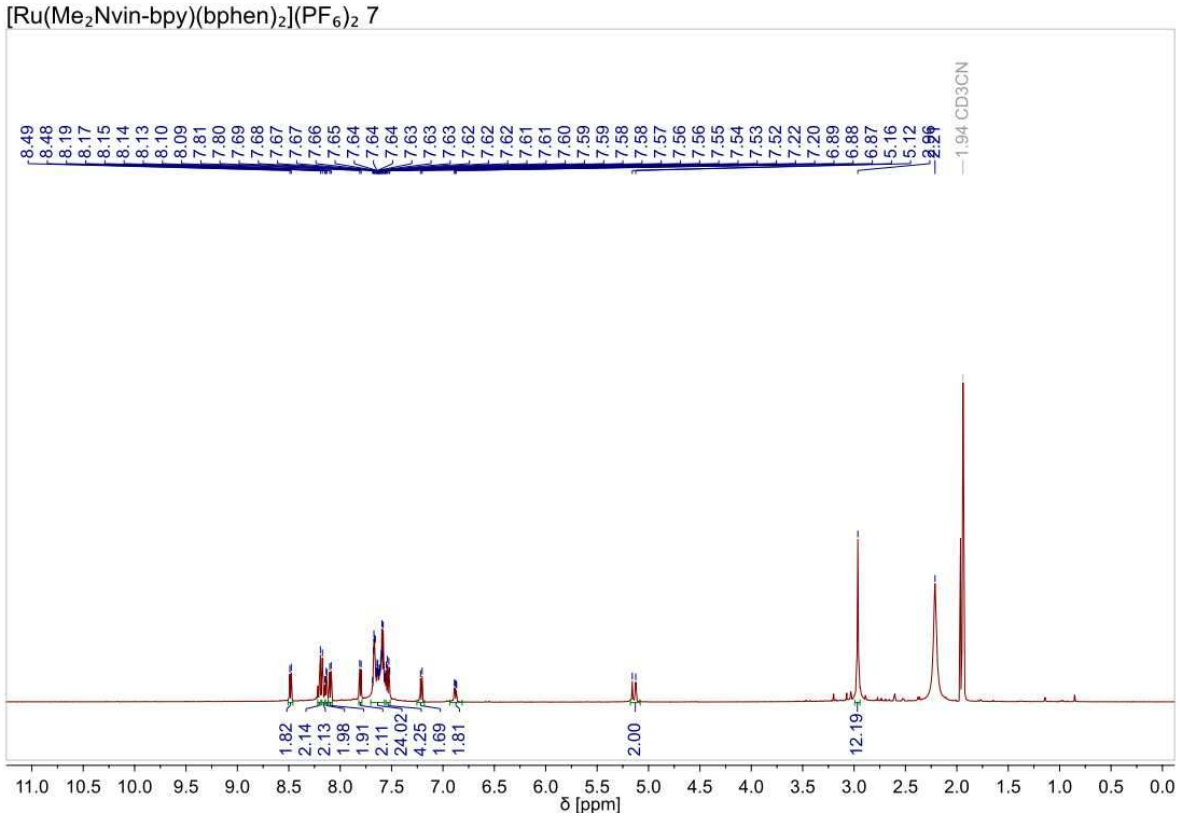

Figure S13. ^{1}H NMR spectrum of **7** in CD_3CN, 500 MHz.

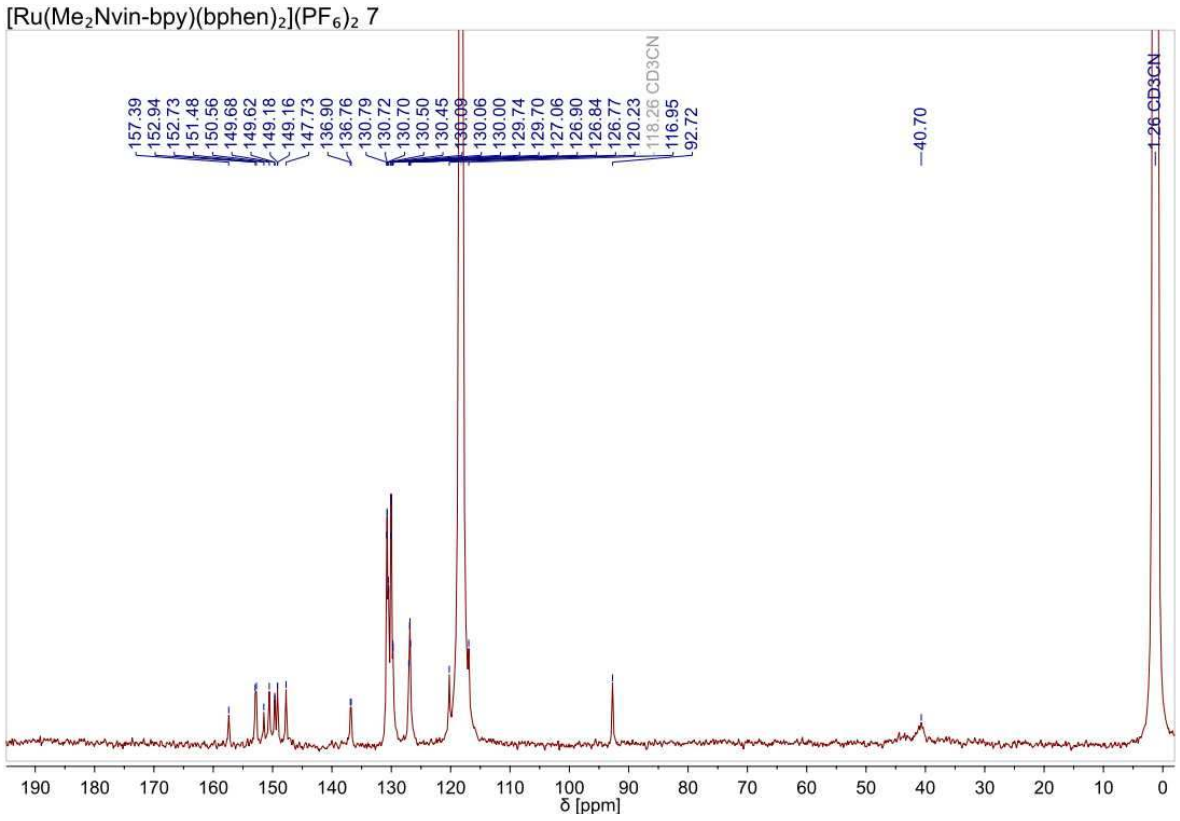

Figure S14. ^{1}H NMR spectrum of **7** in CD_3CN, 125 MHz.

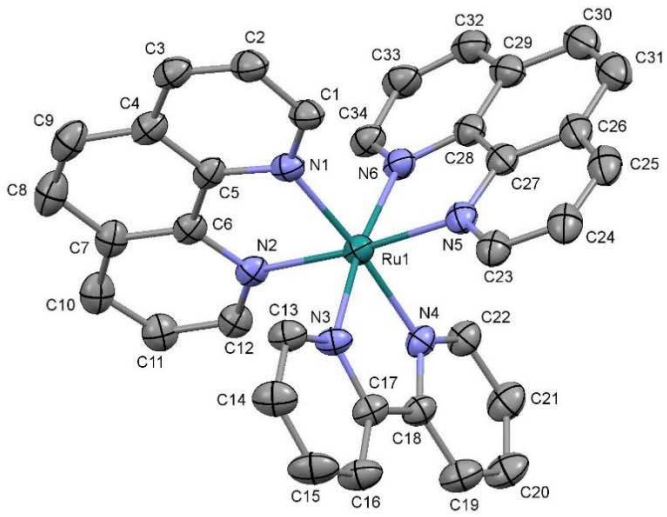

Figure S15. The molecular structure of **1** with displacement ellipsoids drawn at the 20% probability level. Solvent molecules, counterions and hydrogen atoms are excluded for clarity.

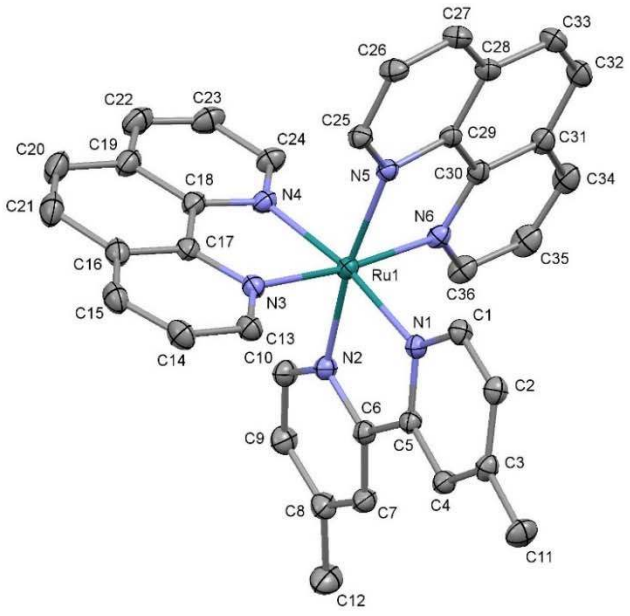

Figure S16. The molecular structure of **2** with displacement ellipsoids drawn at the 20% probability level. Solvent molecules, counterions and hydrogen atoms are excluded for clarity.

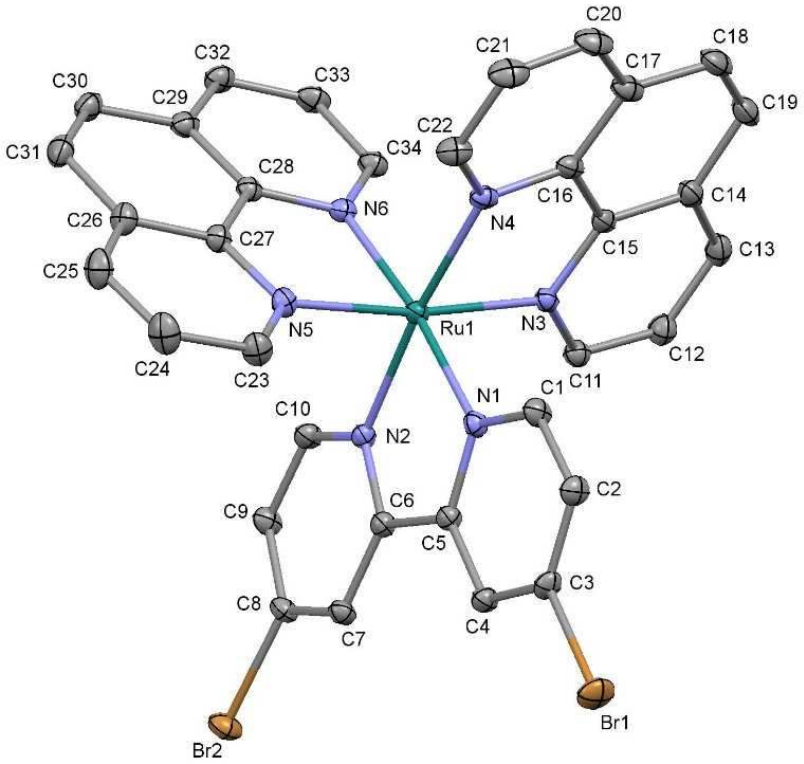

Figure S17. The molecular structure of **3** with displacement ellipsoids drawn at the 20% probability level. Solvent molecules, counterions and hydrogen atoms are excluded for clarity.

Table S8. Crystal data and structure refinement parameters for **1** and **2**.

	1	**2**
CCDC number	1969709	1969708
Empirical formula	$C_{38}H_{30}F_{12}N_8P_2Ru$	$C_{41}H_{38.5}F_{12}N_6O_{1.25}P_2Ru$
Formula weight	989.71	1026.29
Temperature/K	183(1)	183(1)
Crystal system	monoclinic	triclinic
Space group	$P2_1/c$	P-1
a/Å	12.4678(3)	12.8029(3)
b/Å	27.4167(4)	13.1575(2)
c/Å	13.2004(3)	16.2010(4)
α/°	90	79.9877(16)
β/°	118.159(3)	75.692(2)
γ/°	90	62.241(2)
Volume/Å^3	3978.16(16)	2334.63(10)
Z	4	2
ρ_{calc}g/cm^3	1.652	1.460
μ/mm^{-1}	4.832	4.143
F(000)	1984.0	1037.0
Crystal size/mm^3	0.11 × 0.06 × 0.04	0.39 × 0.15 × 0.03
Radiation	CuKα (λ = 1.54184)	CuKα (λ = 1.54184)
2Θ range for data collection/°	6.448 to 148.99	7.6 to 149.0
Index ranges	$-15 \le h \le 14$, $-30 \le k \le 34$, $-16 \le l \le 16$	$-15 \le h \le 15$, $-16 \le k \le 15$, $-20 \le l \le 20$
Reflections collected	30861	44520
Independent reflections	8116 [R_{int} = 0.0339, R_{sigma} = 0.0251]	9539 [R_{int} = 0.0221, R_{sigma} = 0.0130]
Data/restraints/parameters	8116/114/524	9539/86/627
Goodness-of-fit on F^2	1.150	1.089
Final R indexes [I>=2σ (I)]	R_1 = 0.0756, wR_2 = 0.1785	R_1 = 0.0491, wR_2 = 0.1495
Final R indexes [all data]	R_1 = 0.0782, wR_2 = 0.1799	R_1 = 0.0523, wR_2 = 0.1562
Largest diff. peak/hole / e Å^{-3}	1.13/-0.79	1.36/-0.35

Table S9. Crystal data and structure refinement parameters for **3**.

	3
CCDC number	1969710
Empirical formula	$C_{38}H_{28}Br_2F_{12}N_8P_2Ru$
Formula weight	1147.51
Temperature/K	183(1)
Crystal system	triclinic
Space group	P-1
a/Å	11.4219(3)
b/Å	12.3760(3)
c/Å	15.0464(4)
α/°	90.834(2)
β/°	98.147(2)
γ/°	101.020(2)
Volume/Å^3	2064.73(10)
Z	2
ρ_{calc}g/cm^3	1.846
μ/mm^{-1}	2.488
F(000)	1128.0
Crystal size/mm^3	0.29 × 0.25 × 0.17
Radiation	MoKα (λ = 0.71073)
2Θ range for data collection/°	4.42 to 55.75
Index ranges	-15 ≤ h ≤ 15, -16 ≤ k ≤ 16, -19 ≤ l ≤ 19
Reflections collected	38483
Independent reflections	9850 [R_{int} = 0.0490, R_{sigma} = 0.0378]
Data/restraints/parameters	9850/312/643
Goodness-of-fit on F^2	1.031
Final R indexes [I>=2σ (I)]	R_1 = 0.0398, wR_2 = 0.1020
Final R indexes [all data]	R_1 = 0.0488, wR_2 = 0.1096
Largest diff. peak/hole / e Å^{-3}	0.79/-0.61

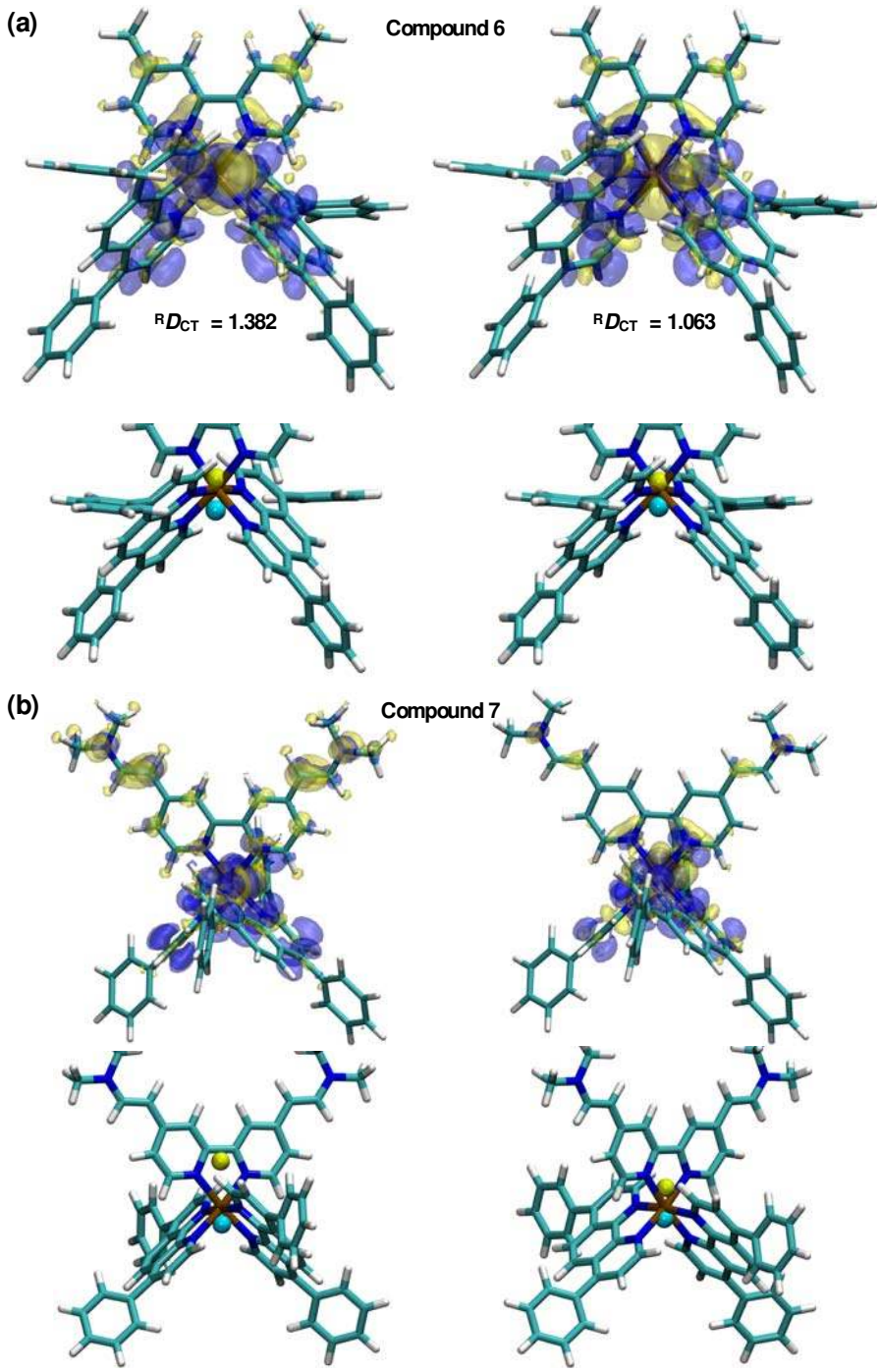

Figure S18. Difference density plots calculated between ES and GS (top row) computed for the first vertical transition and the first bright state MLCT transition of **6 (a)** and **7 (b)**. For **7** both transitions are of MLCT type while the first one of **6 (a)** is an inter-ligand charge transfer π-π* transition. Yellow regions are characterized by an increase in density upon excitation while blue ones show a decrease in electron density. The barycenters are depicted as spheres (bottom rows) and the corresponding distances of charge transfer $^{R}D_{CT}$ (in Å) are stated above. Atoms color scheme: C - green; H - white; N - blue; O - red, Ru - brown.

Table S10. Spectroscopic properties of complexes **1**-**7** in CH_3CN at room temperature.

	UV/Vis Absorption λ [nm] (ε [M^{-1} cm^{-1} × 10^3])	Emission λ_{em} [nm]	Φ_{em}	Lifetime [ns]	
				Air sat.	degassed
1	200 (73.2), 225 (64.3), 264 (86.5), 284 (44.1), 446 (15.0)	600	0.027	130	766
2	202 (77.9), 222 (61.5), 264 (81.7), 280 (43.9), 421 (12.8), 449 (13.9)	606	0.050	110	918
3	201 (72.9), 223 (91.0), 263 (95.2), 289 (45.1), 388 (11.5), 441 (14.8)	645	0.014	207	617
4	201 (100.1), 223 (91.3), 263 (105.8), 308 (28.2), 386 (13.8), 438 (16.7), 441 (16.8)	654	0.020	326	1387
5	201 (89.3), 224 (81.2), 265 (91.1), 379 (25.6), 458 (23.1)	703	<0.001	75	339
6	192 (183.4), 279 (126.3), 441 (23.2), 457 (23.2)	623	0.021	161	1096
7	192 (168.8), 280 (102.5), 371 (35.0), 465 (30.1)	694	<0.001	55	312

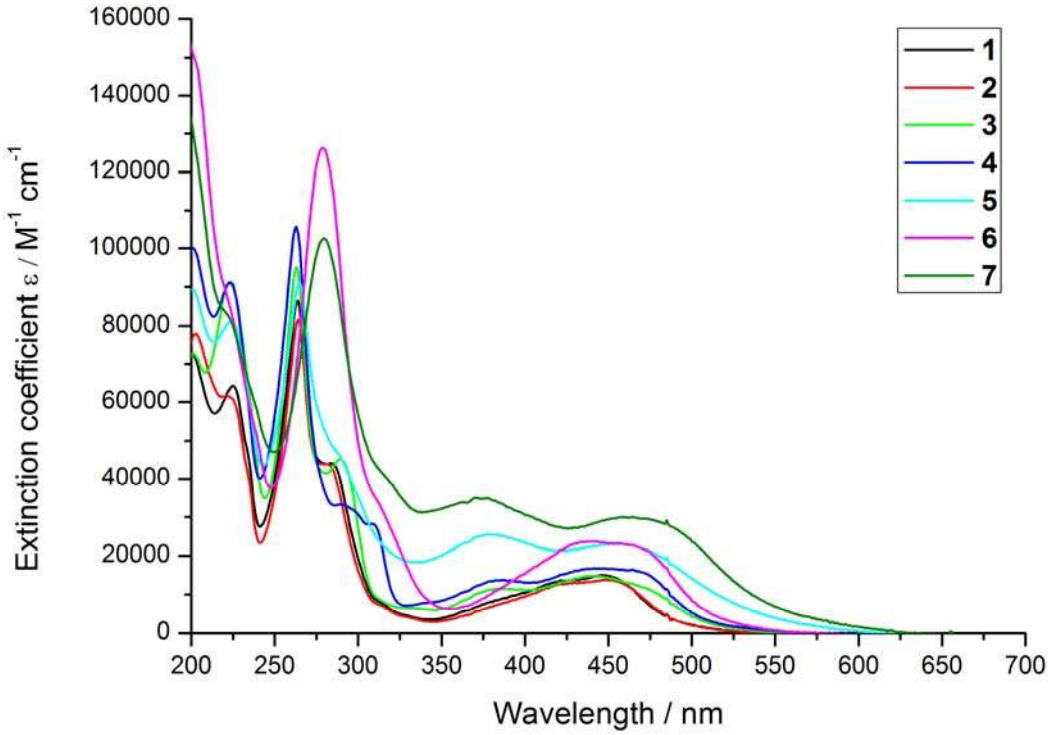

Figure S19. Measured UV/Vis spectra of the complexes **1-7** in CH_3CN.

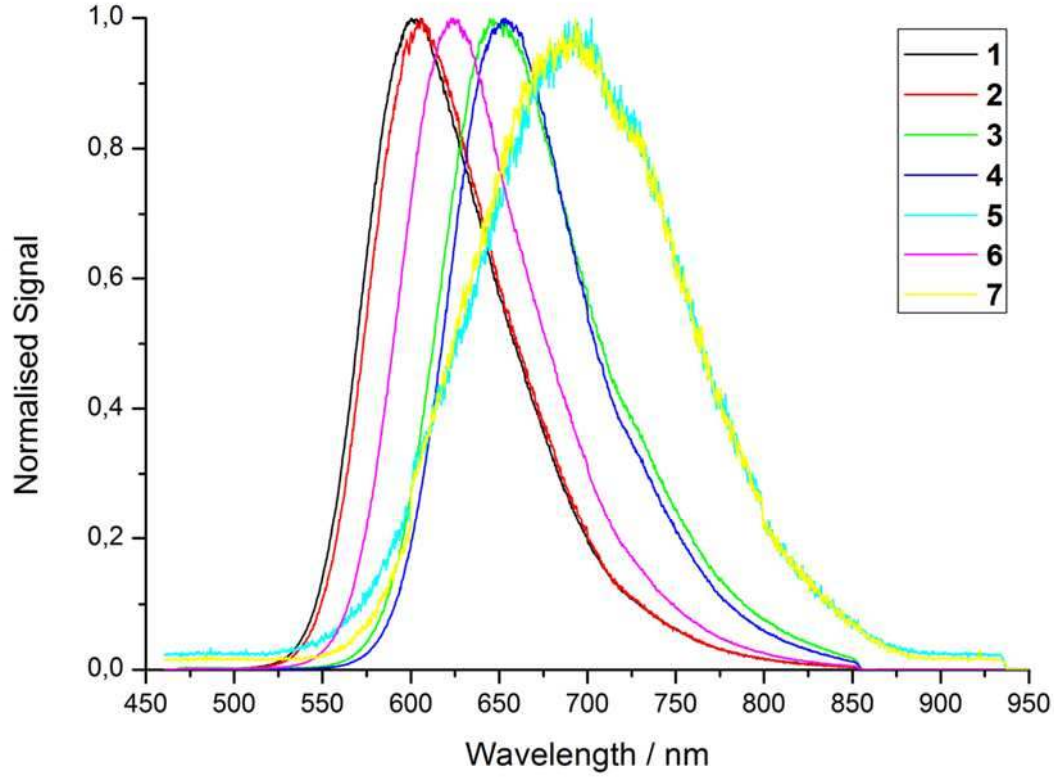

Figure S20. Normalised emission spectra of the complexes **1-7** in CH_3CN.

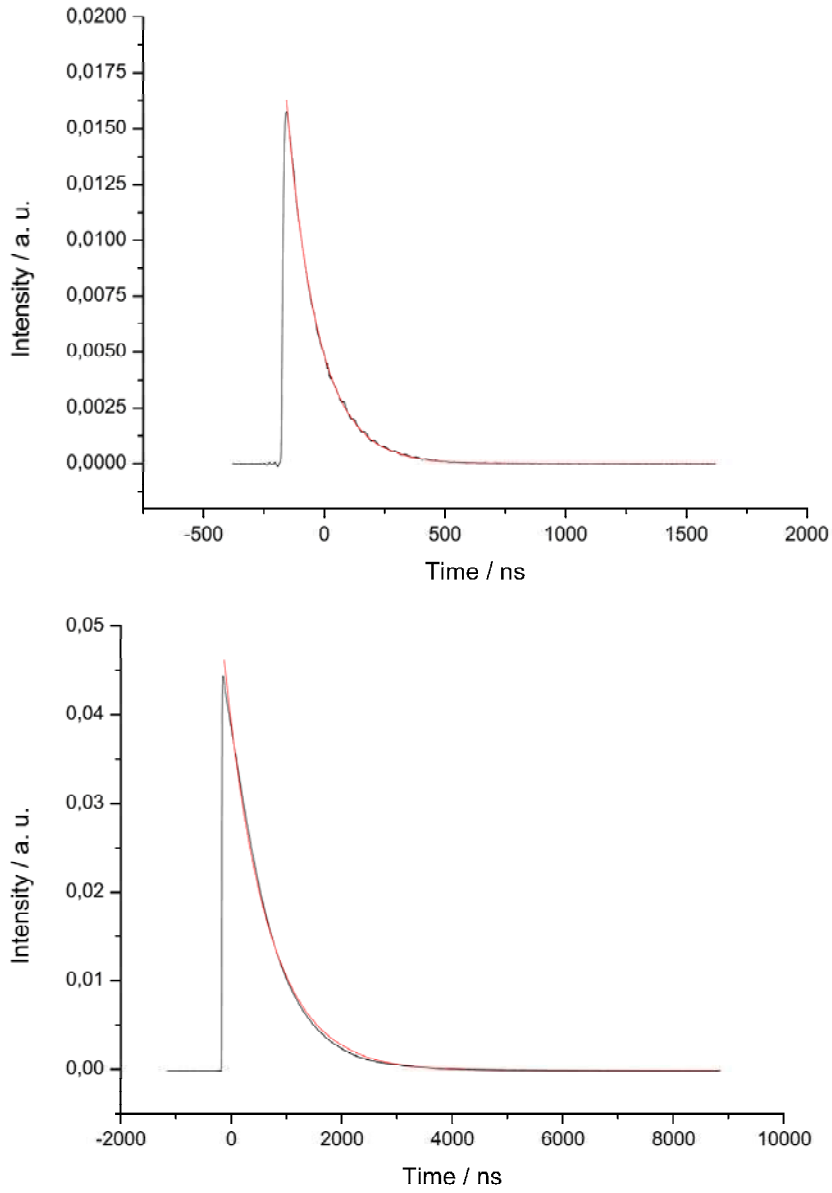

Figure S21. Lifetime spectra of the complexes **1** in aerated (above) and degassed (below) CH_3CN.

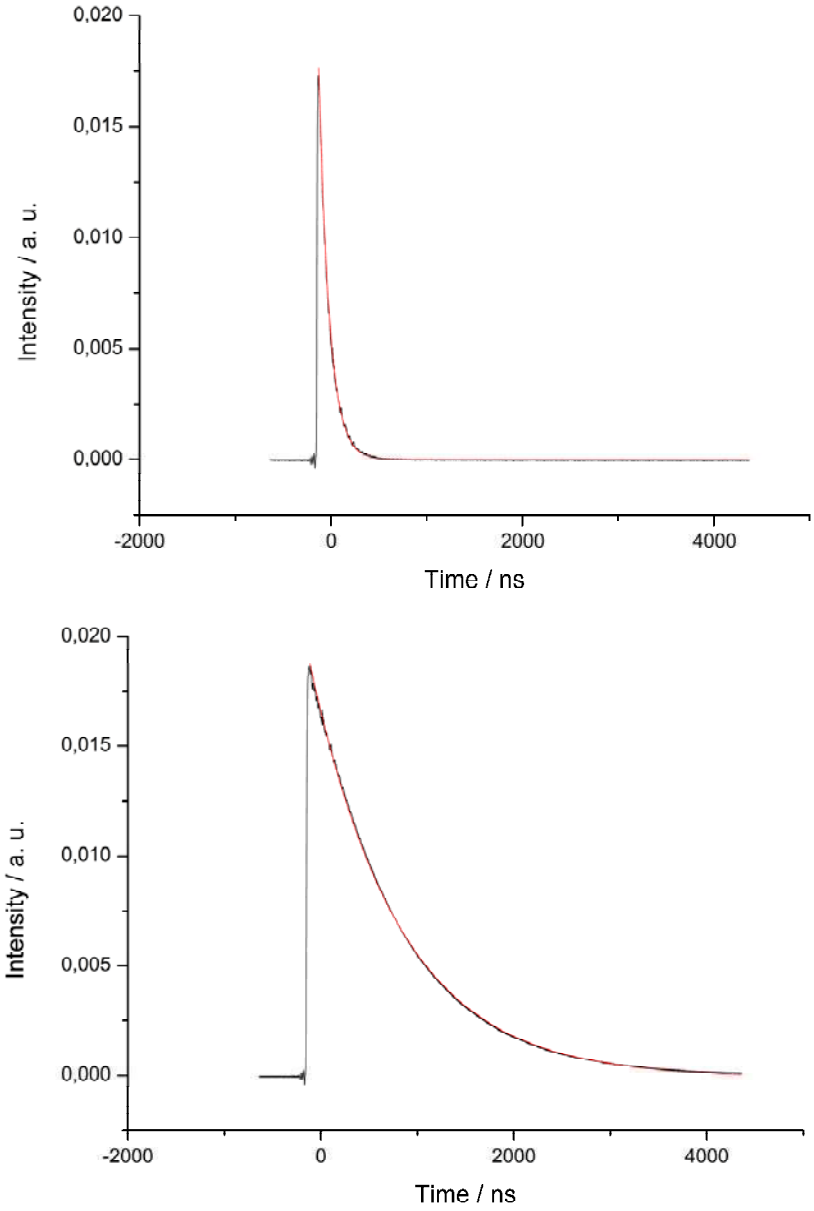

Figure S22. Lifetime spectra of the complexes **2** in aerated (above) and degassed (below) CH_3CN.

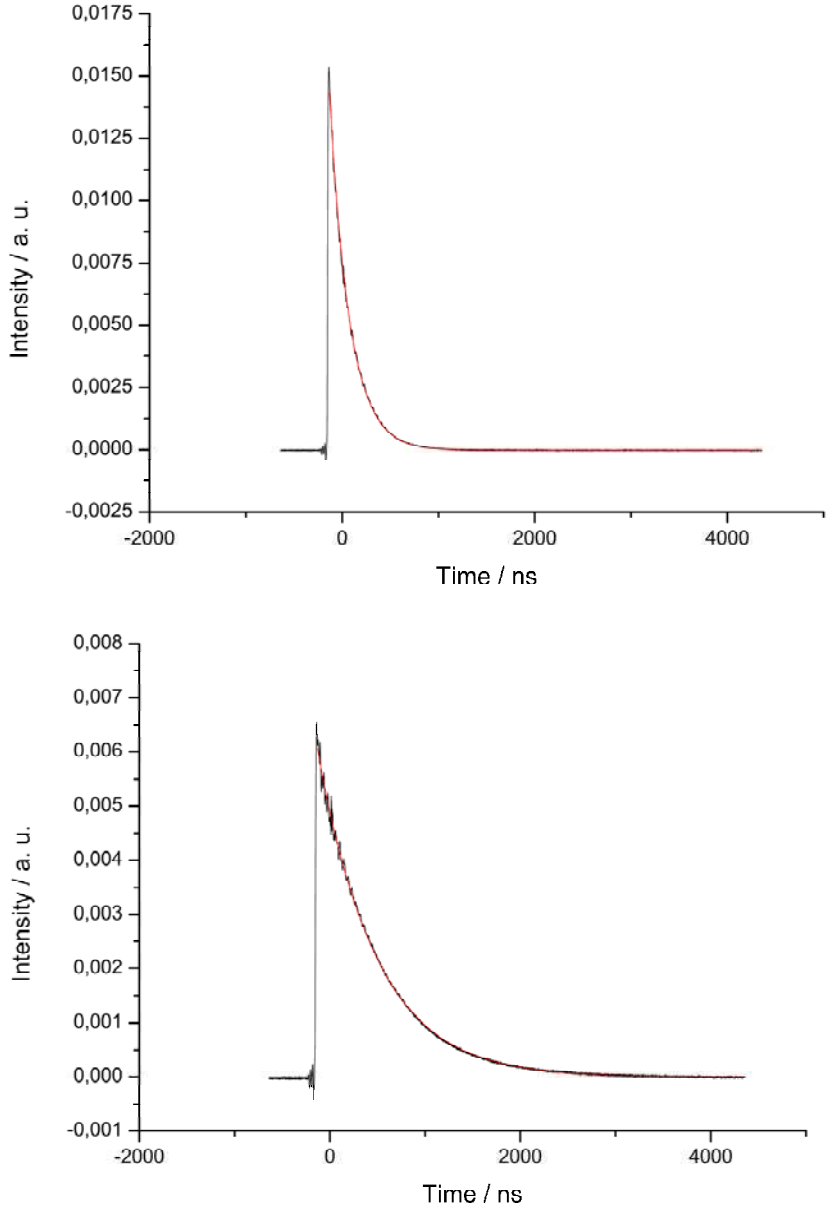

Figure S23. Lifetime spectra of the complexes **3** in aerated (above) and degassed (below) CH_3CN.

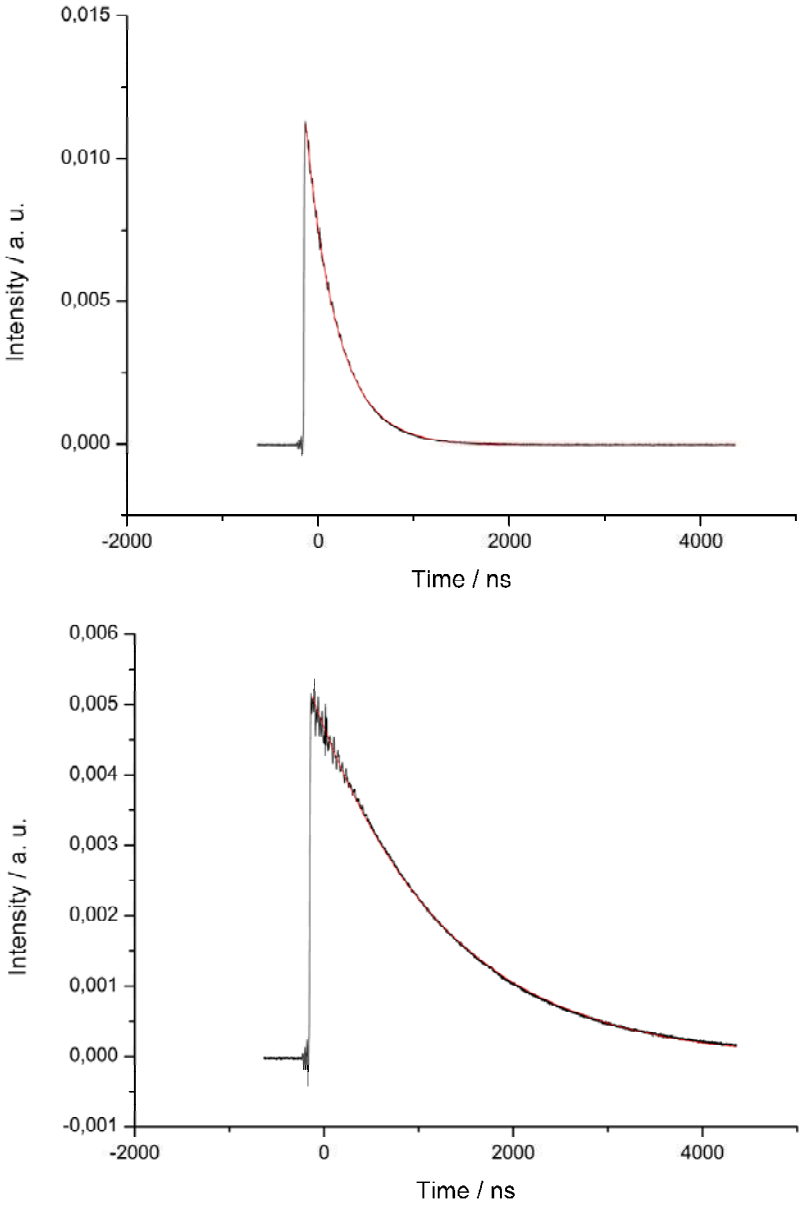

Figure S24. Lifetime spectra of the complexes **4** in aerated (above) and degassed (below) CH_3CN.

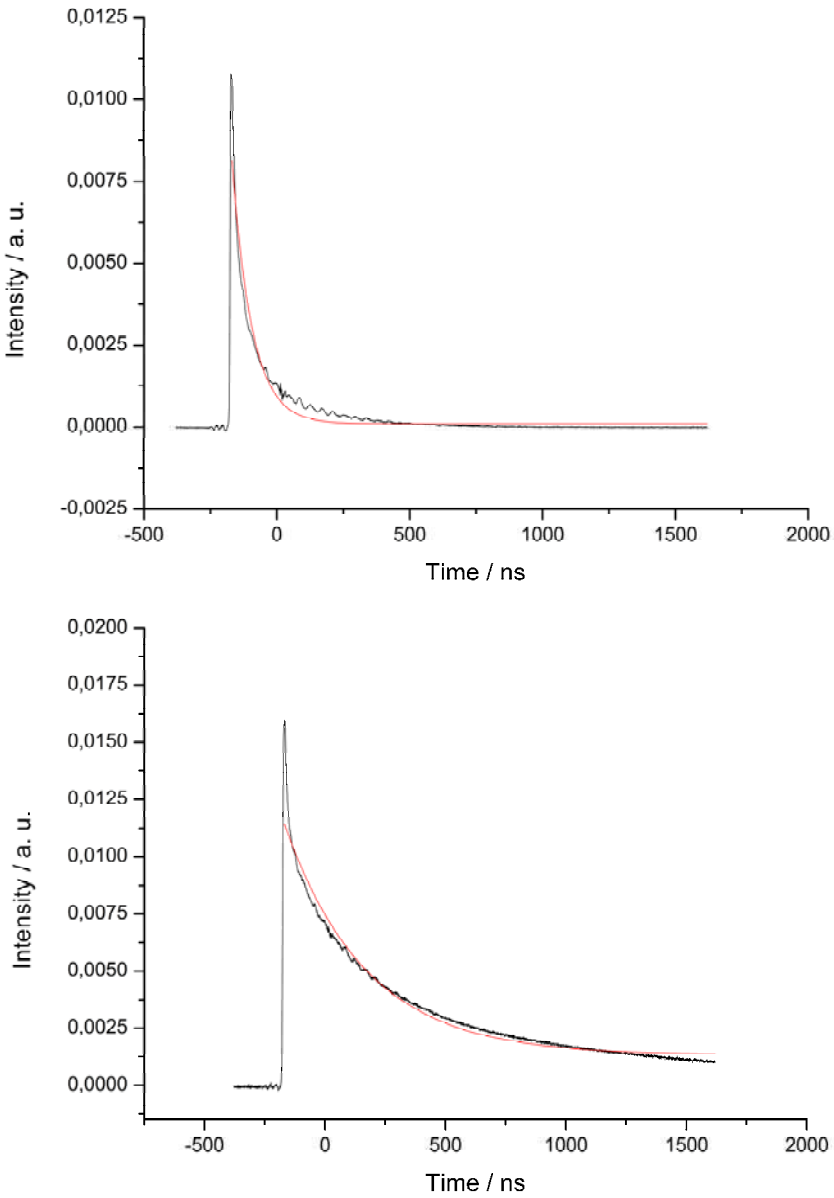

Figure S25. Lifetime spectra of the complexes **5** in aerated (above) and degassed (below) CH_3CN.

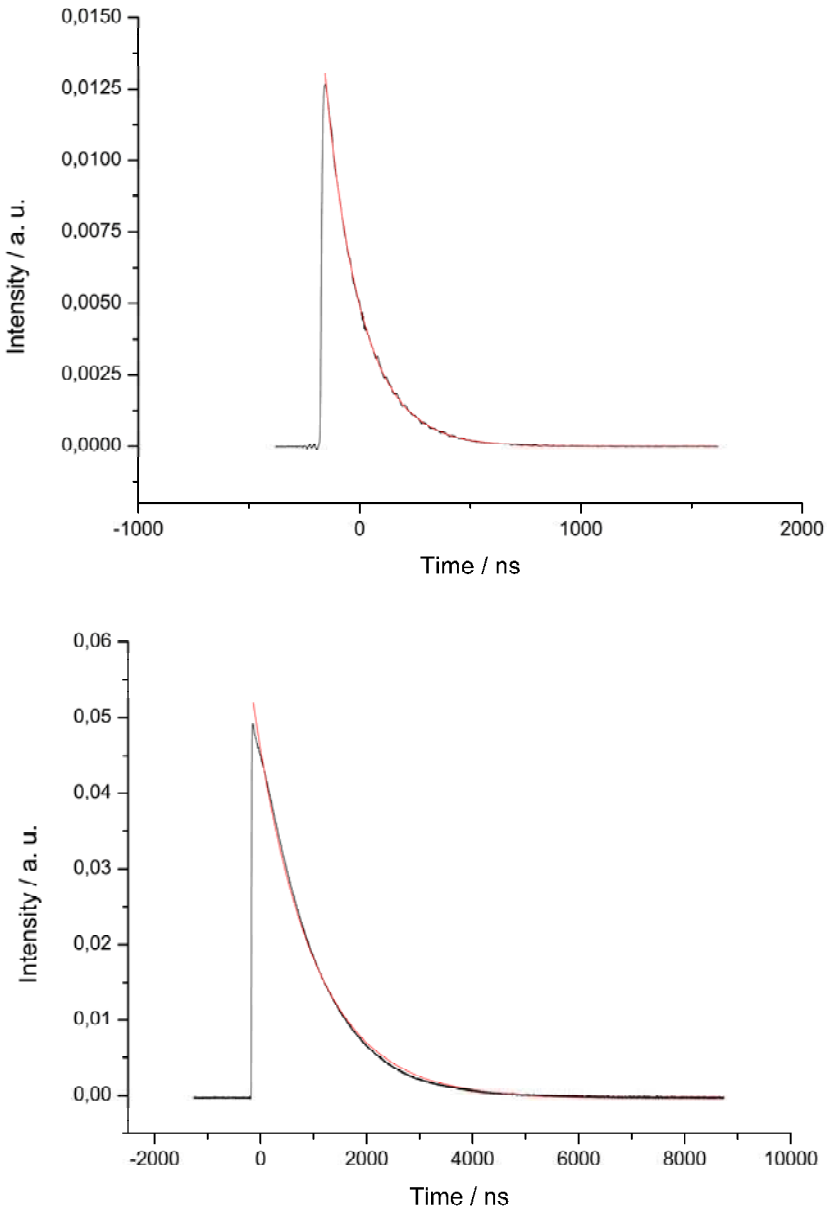

Figure S26. Lifetime spectra of the complexes **6** in aerated (above) and degassed (below) CH_3CN.

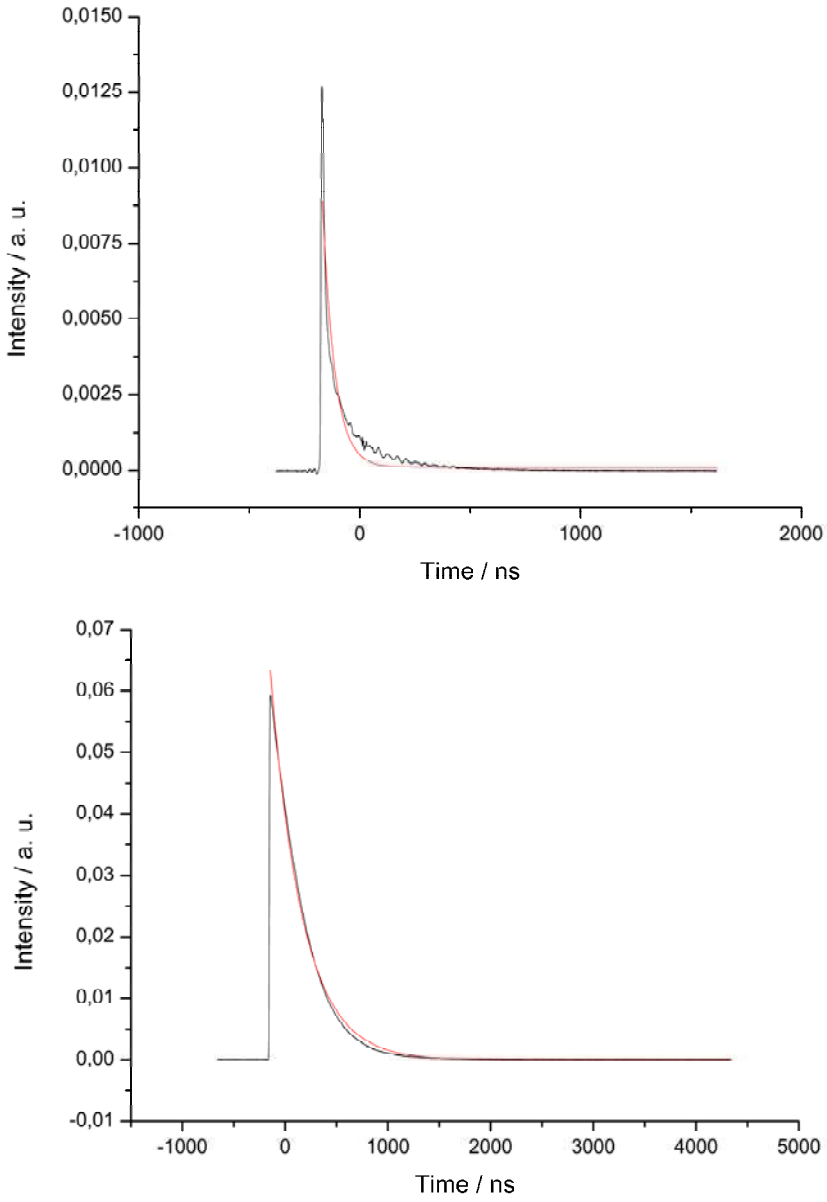

Figure S27. Lifetime spectra of the complexes **7** in aerated (above) and degassed (below) CH_3CN.

Table S11. Singlet oxygen quantum yields ($\Phi(^1O_2)$) in CH_3CN and aqueous solution determined by direct and indirect methods by excitation at 450 nm. Average of three independent measurements, ±10%.

Compound	CH_3CN Direct	CH_3CN Indirect	D_2O Direct	PBS indirect
1	0.57	0.54	0.27	0.36
2	0.69	0.53	0.31	0.34
3	0.55	0.56	n.d.	0.21
4	0.62	0.59	0.25	0.26
5	0.24	0.30	n.d.	0.21
6	0.61	0.63	n.d.	0.05
7	0.22	0.35	n.d.	0.07

n.d. = not determinable, $\Phi(^1O_2)$ <0.20.

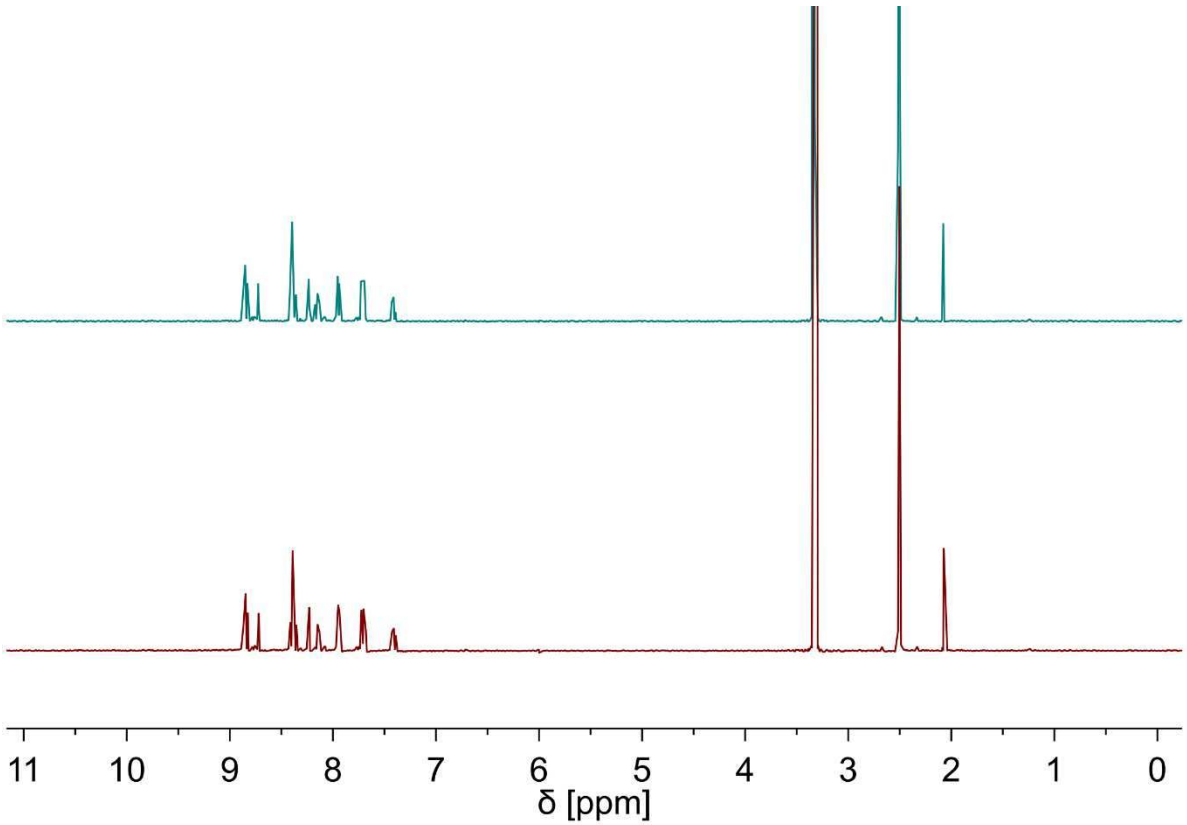

Figure S28. ^1H NMR spectrum of **1** in DMSO-d_6 after preparation (green) and 7 days (red).

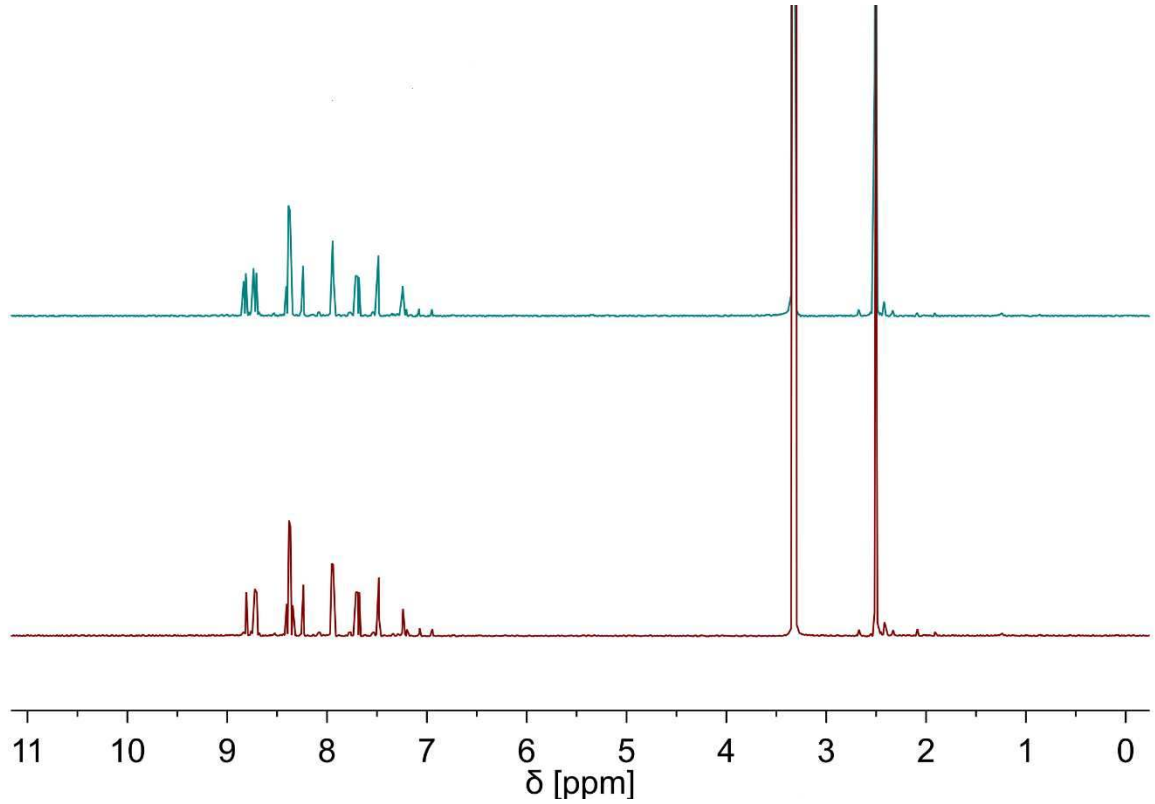

Figure S29. ^{1}H NMR spectrum of **2** in DMSO-d_6 after preparation (green) and 7 days (red).

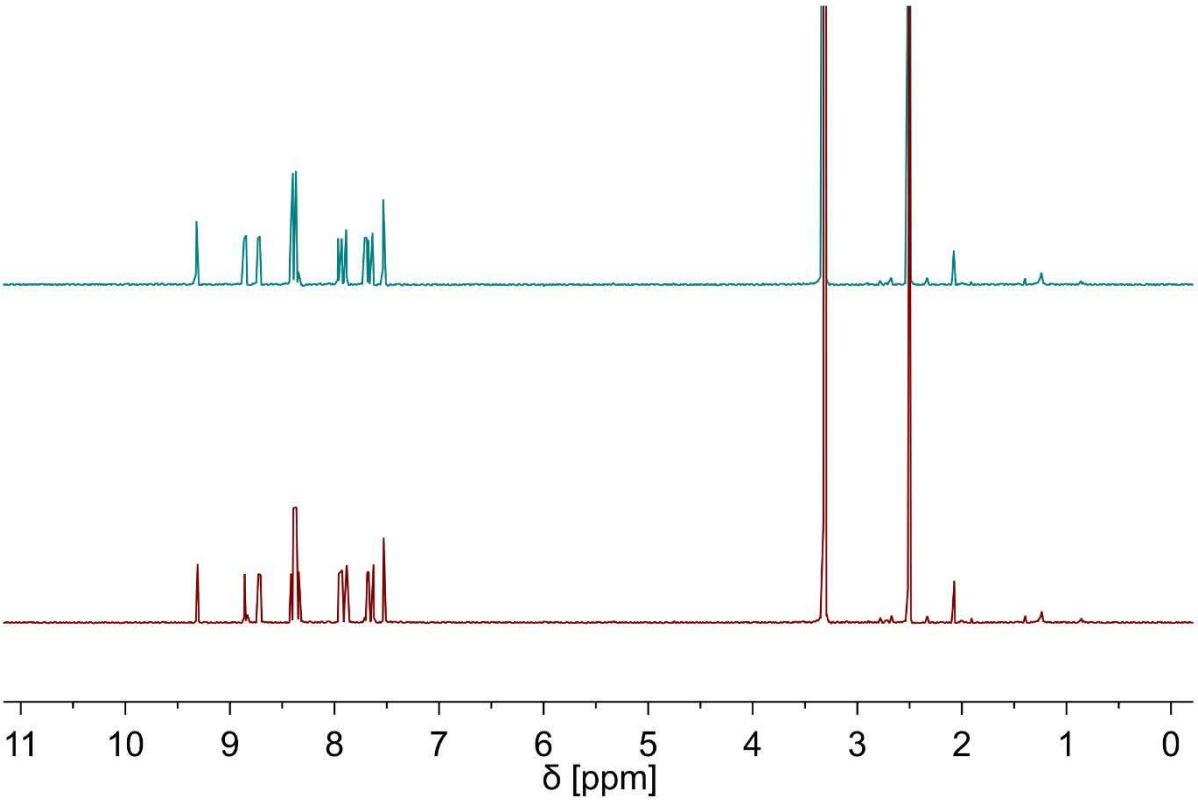

Figure S30. ^{1}H NMR spectrum of **3** in DMSO-d_6 after preparation (green) and 7 days (red).

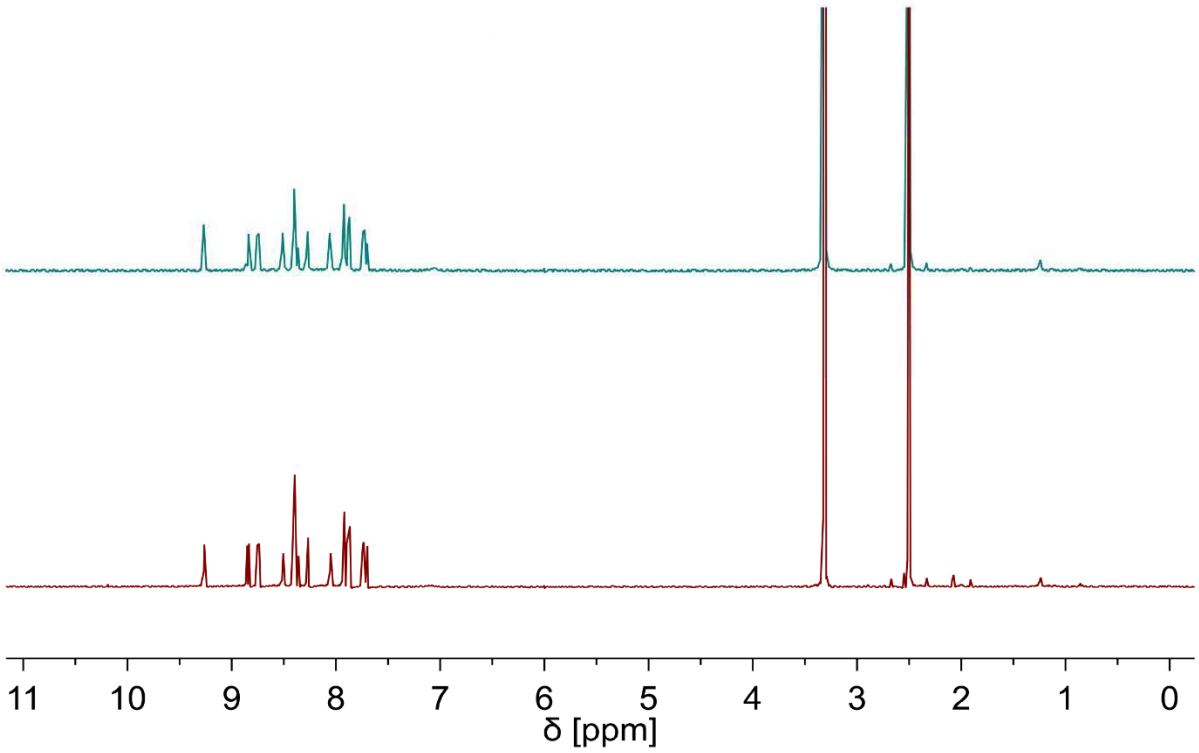

Figure S31. ^{1}H NMR spectrum of **4** in DMSO-d$_6$ after preparation (green) and 7 days (red).

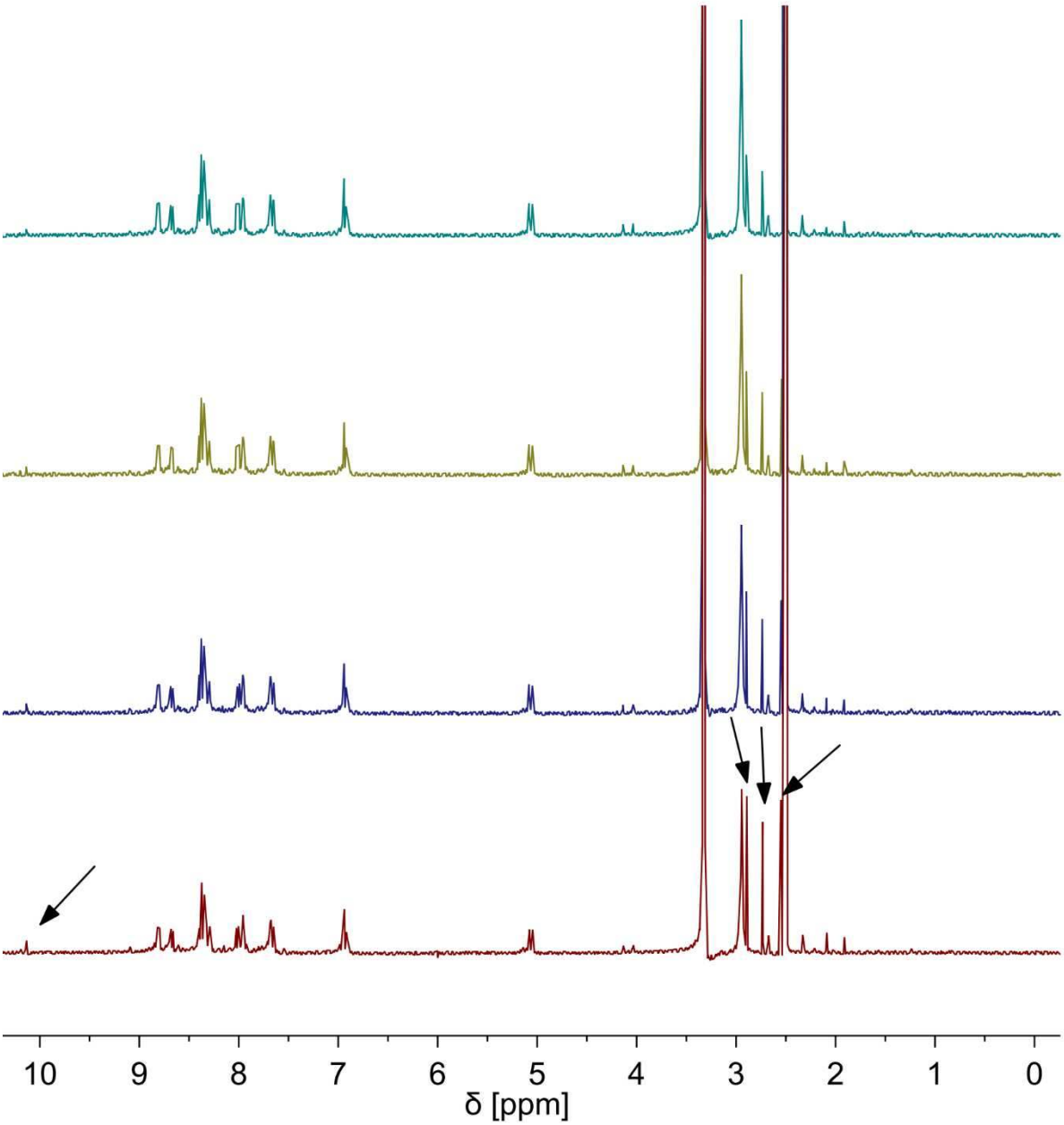

Figure S32. ^{1}H NMR spectrum of **5** in DMSO-d_6 after preparation (green), 1 day (olive), 2 days (blue) and 7 days (red).

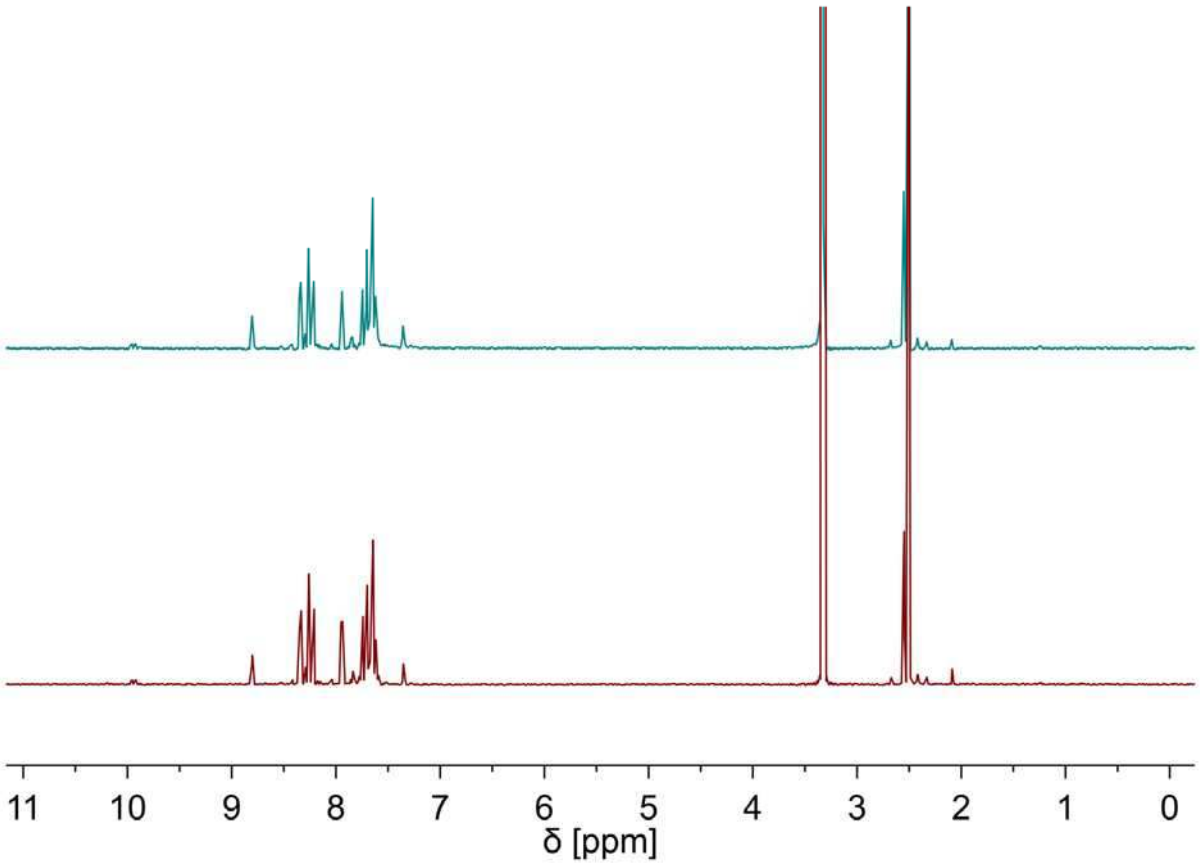

Figure S33. ^{1}H NMR spectrum of **6** in DMSO-d$_6$ after preparation (green) and 7 days (red).

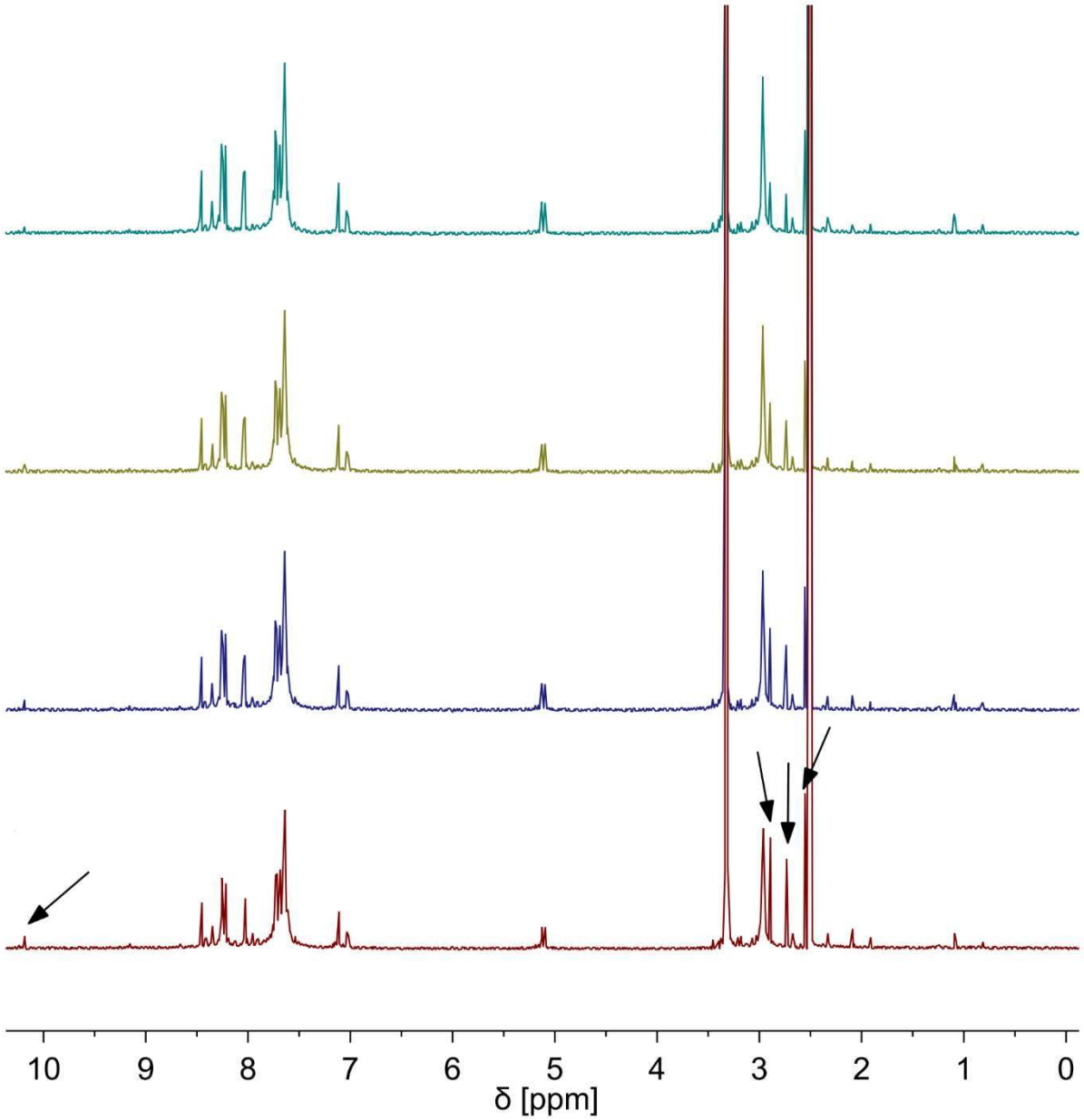

Figure S34. ^{1}H NMR spectrum of **7** in DMSO-d_6 after preparation (green), 1 day (olive), 2 days (blue) and 7 days (red).

Caffeine	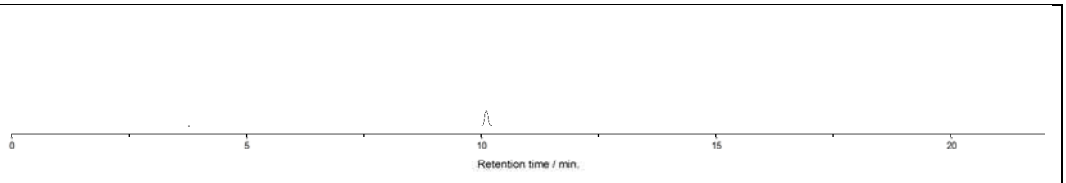
48 h	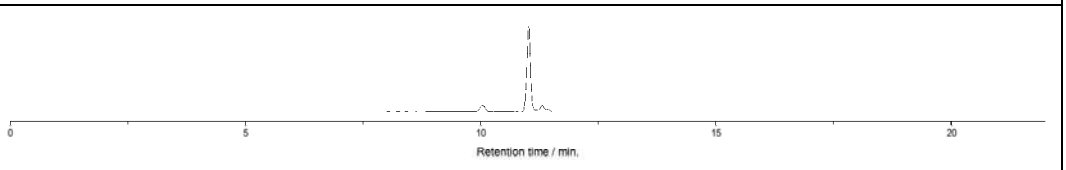

Figure S35. HPLC chromatogram (Method M1) of Caffeine (internal standard) and **1** after 48 h incubation in human pooled plasma.

Caffeine	
48 h	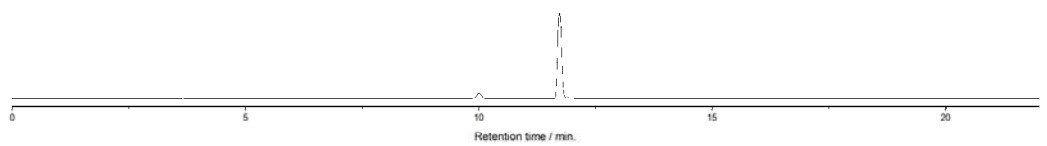

Figure S36. HPLC chromatogram (Method M1) of Caffeine (internal standard) and **2** after 48 h incubation in human pooled plasma.

Caffeine	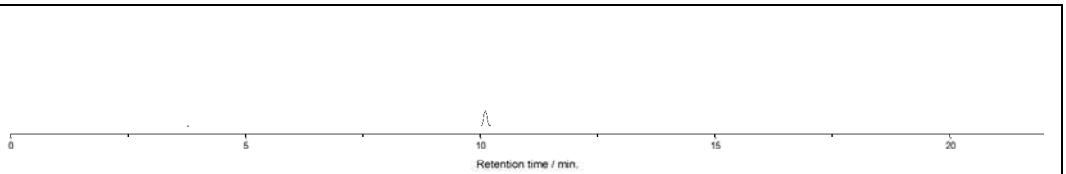
48 h	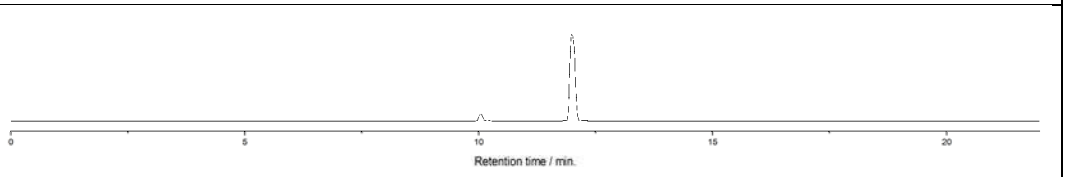

Figure S37. HPLC chromatogram (Method M1) of Caffeine (internal standard) and **3** after 48 h incubation in human pooled plasma.

Caffeine	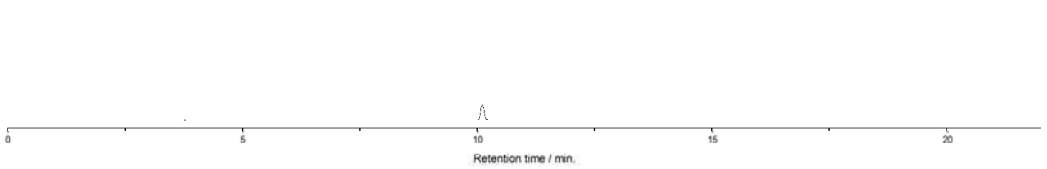

48 h	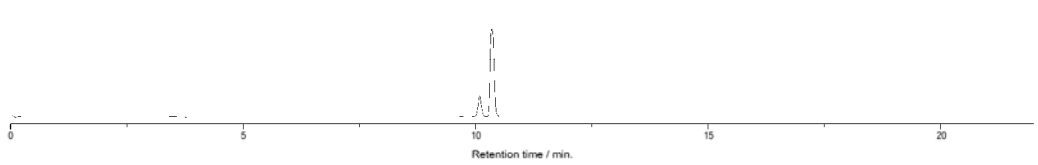

Figure S38. HPLC chromatogram (Method M1) of Caffeine (internal standard) and **4** after 48 h incubation in human pooled plasma.

Caffeine	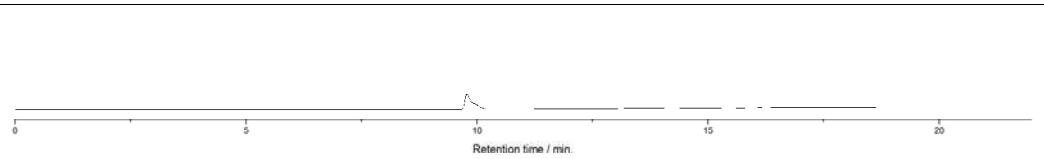
0 h	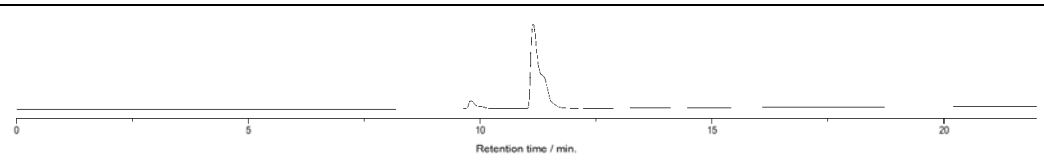
4 h	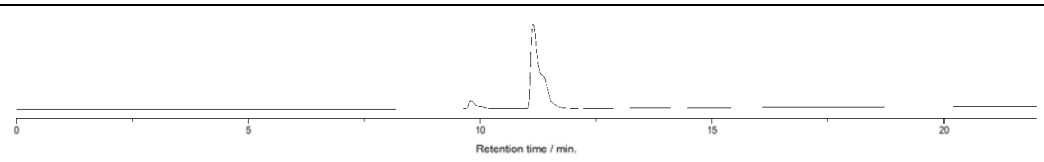
12 h	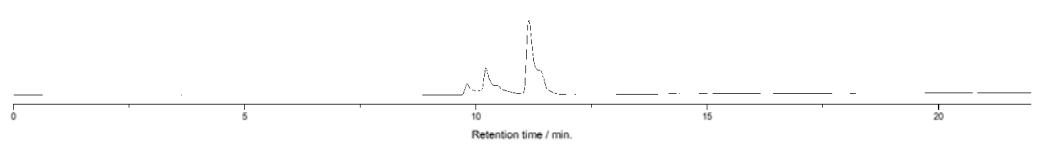
24 h	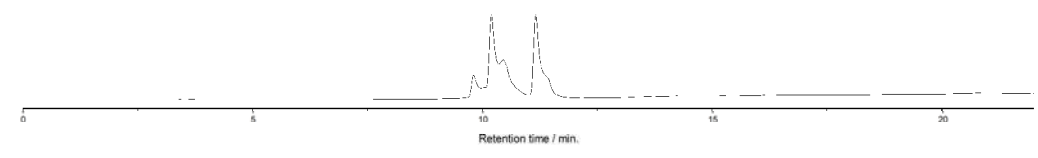
48 h	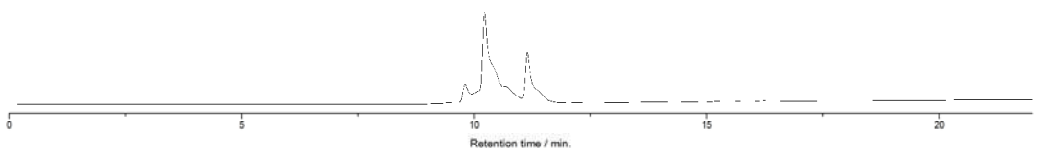

Figure S39. HPLC chromatogram (Method M2) of Caffeine (internal standard) and **5** after 0 h, 4 h, 12 h, 24 h and 48 h incubation in human pooled plasma.

Caffeine	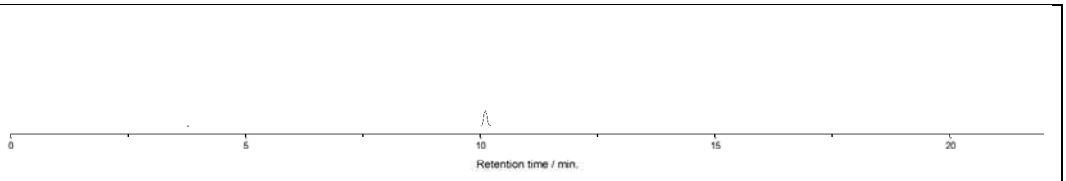
48 h	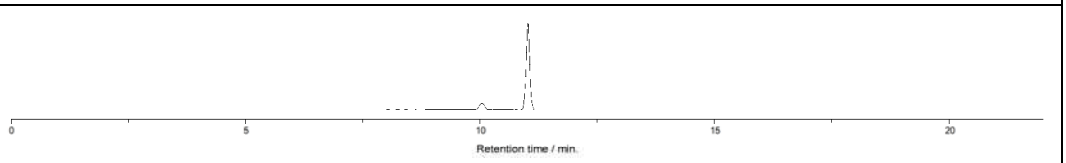

Figure S40. HPLC chromatogram (Method M1) of Caffeine (internal standard) and **6** after 48 h incubation in human pooled plasma.

Caffeine	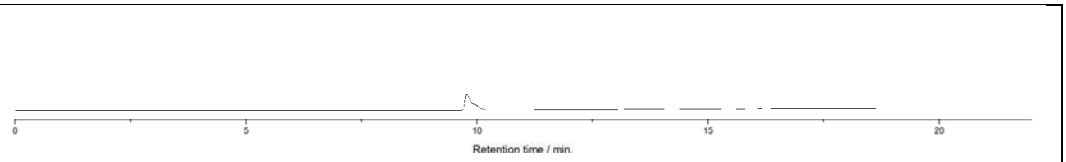
0 h	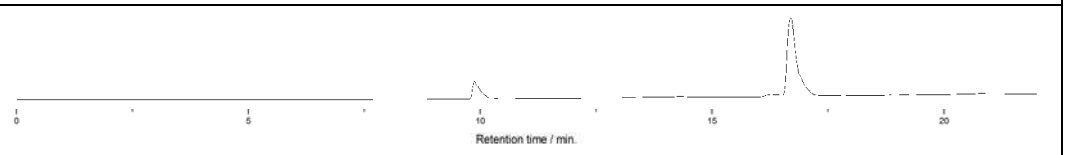
4 h	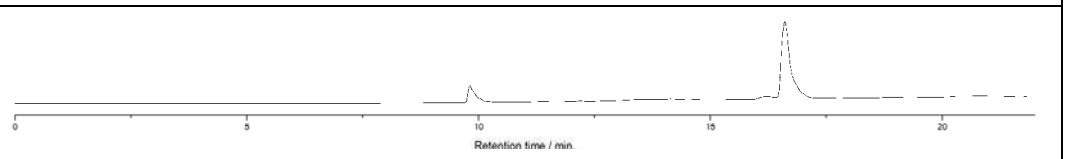
12 h	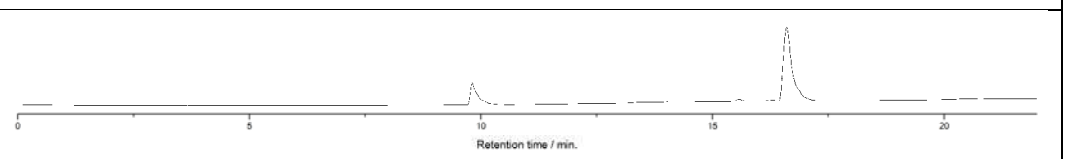
24 h	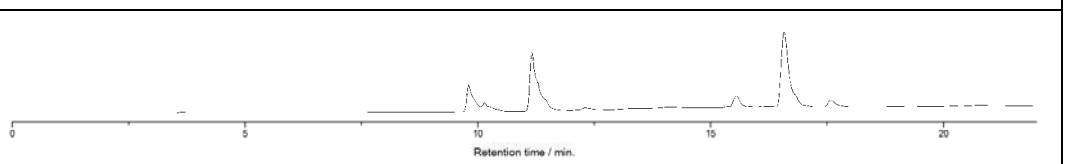
48 h	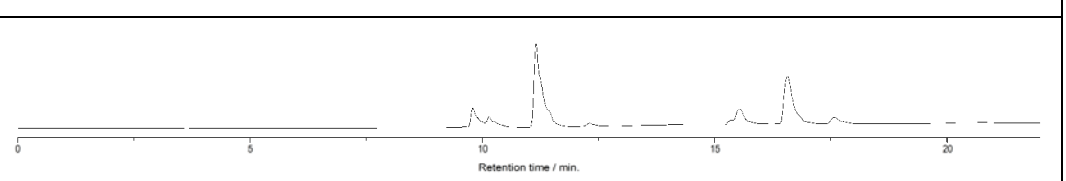

Figure S41. HPLC chromatogram (Method M2) of Caffeine (internal standard) and **7** after 0 h, 4 h, 12 h, 24 h and 48 h incubation in human pooled plasma.

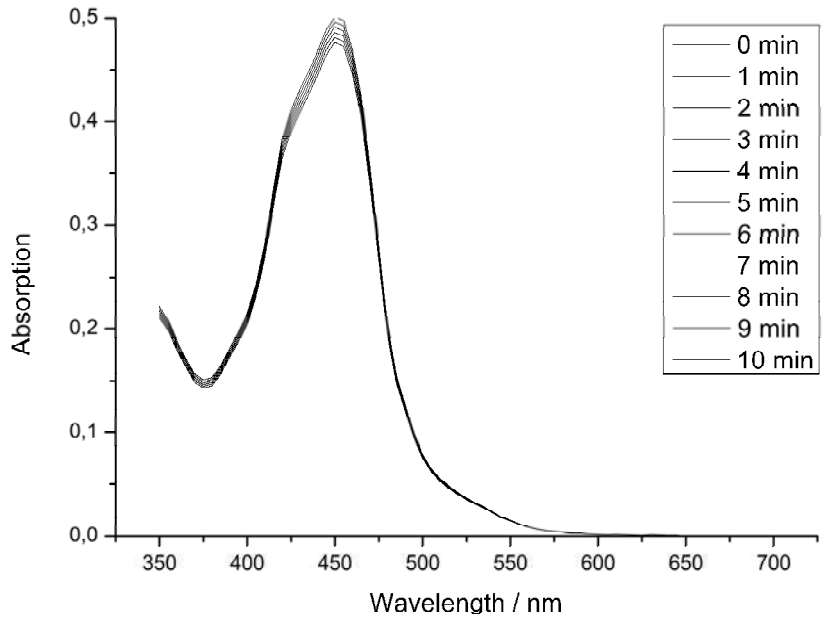

Figure S42. Temporal change of the UV/Vis spectra of $[Ru(bipy)_3]Cl_2$ by irradiation at 450 nm in CH_3CN.

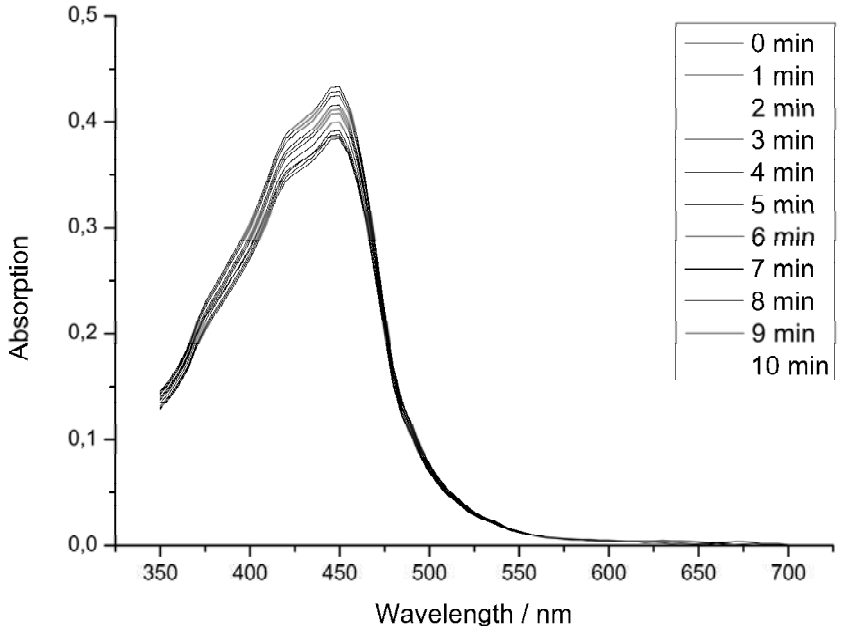

Figure S43. Temporal change of the UV/Vis spectra of complex **1** by irradiation at 450 nm in CH_3CN.

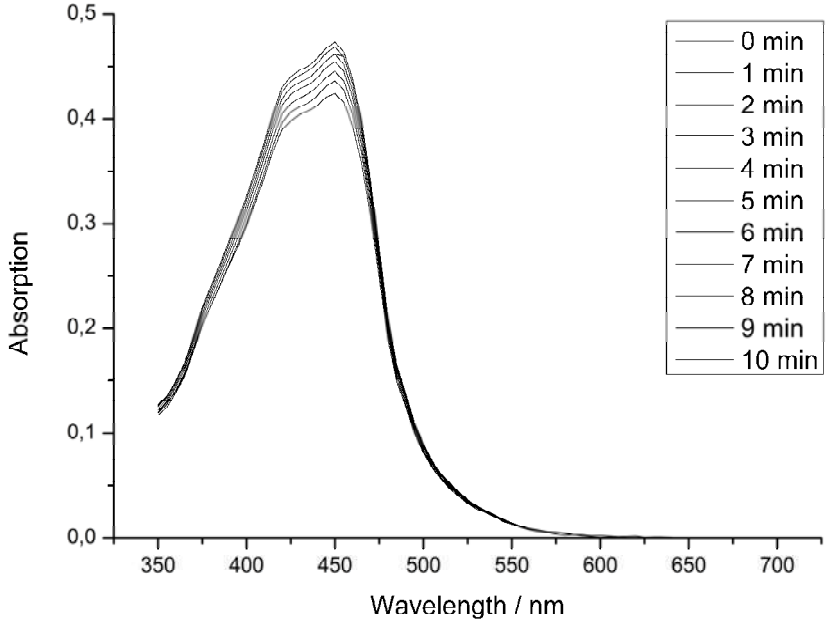

Figure S44. Temporal change of the UV/Vis spectra of complex **2** by irradiation at 450 nm in CH_3CN.

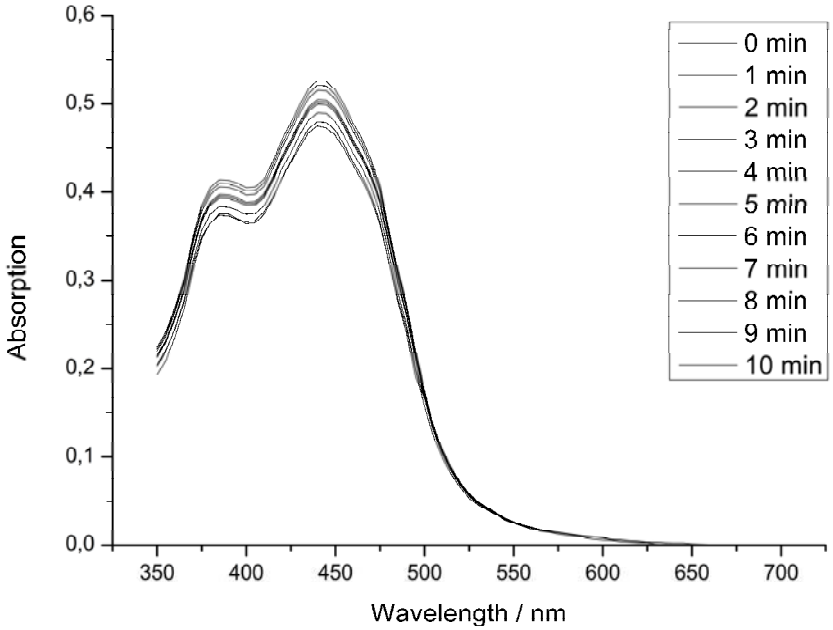

Figure S45. Temporal change of the UV/Vis spectra of complex **3** by irradiation at 450 nm in CH_3CN.

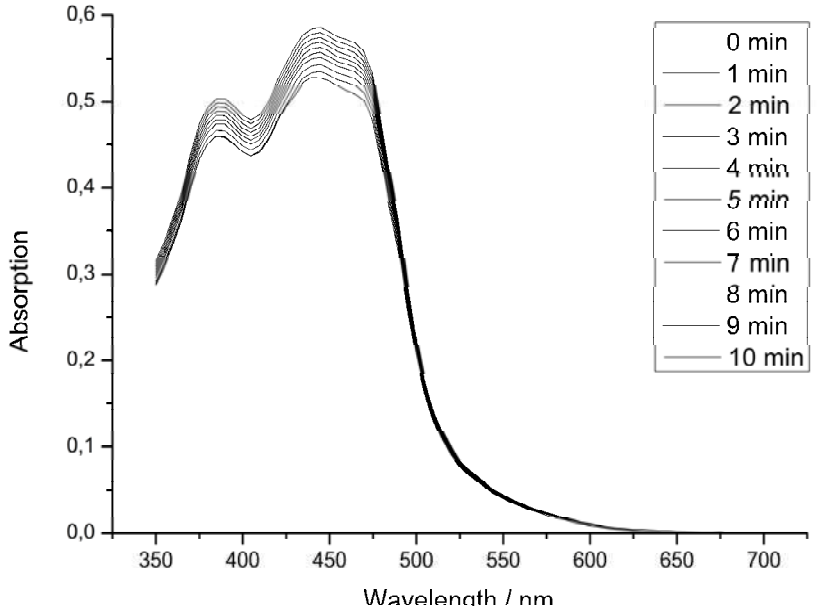

Figure S46. Temporal change of the UV/Vis spectra of complex **4** by irradiation at 450 nm in CH_3CN.

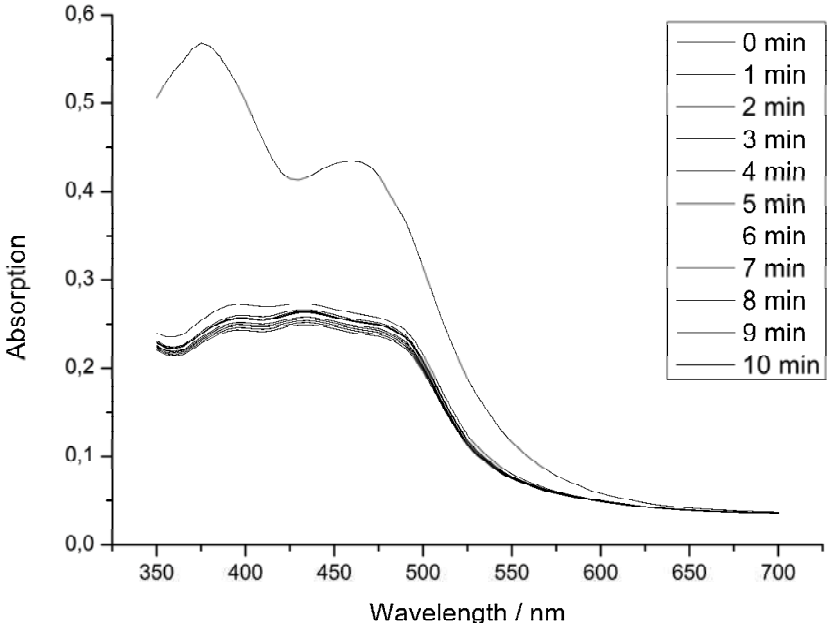

Figure S47. Temporal change of the UV/Vis spectra of complex **5** by irradiation at 450 nm in CH_3CN.

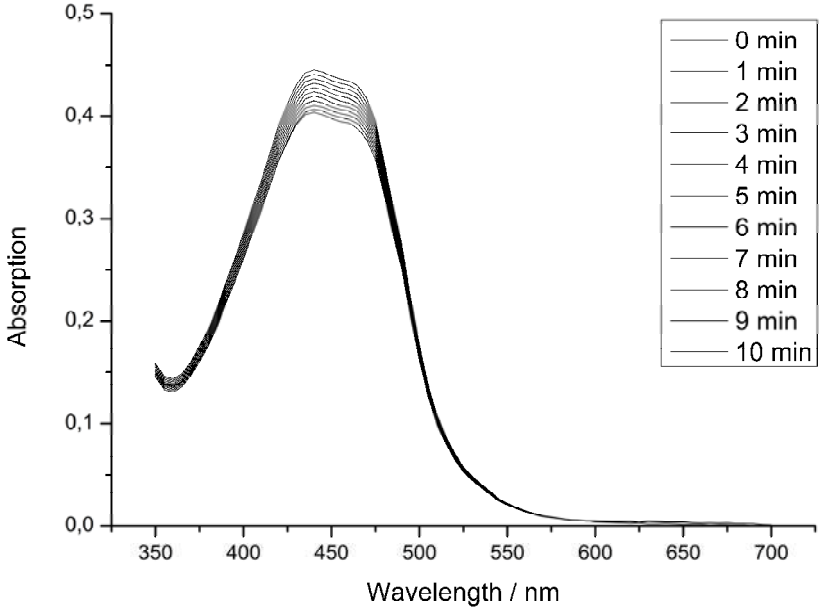

Figure S48. Temporal change of the UV/Vis spectra of complex **6** by irradiation at 450 nm in CH_3CN.

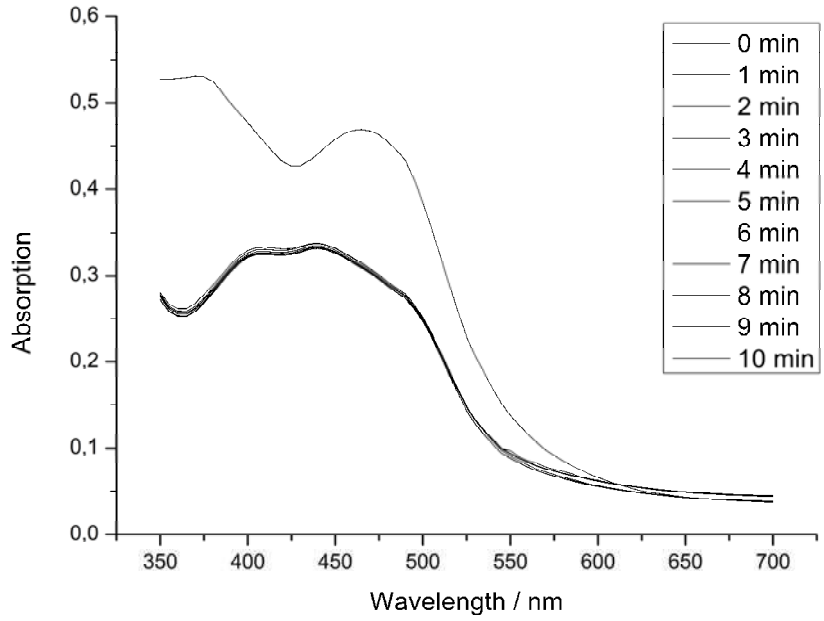

Figure S49. Temporal change of the UV/Vis spectra of complex **7** by irradiation at 450 nm in CH_3CN.

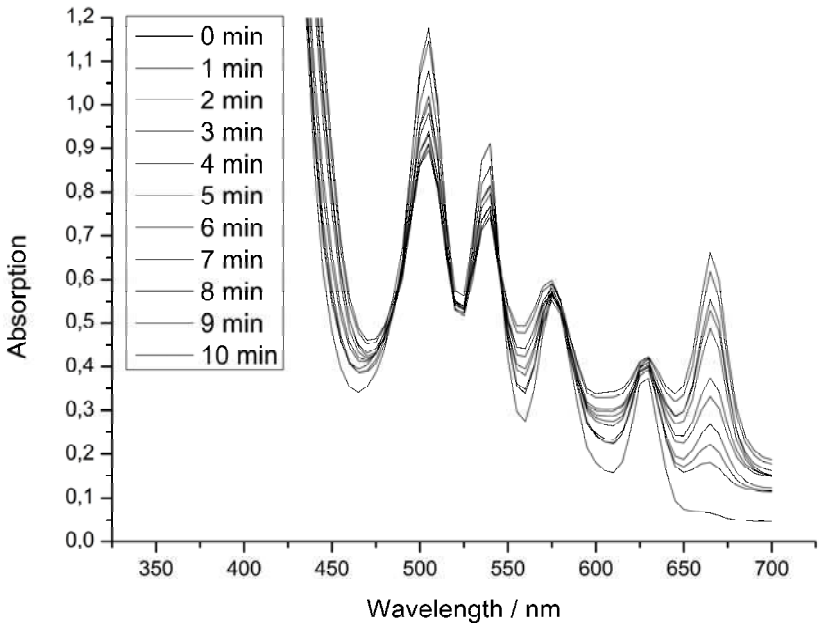

Figure S50. Temporal change of the UV/Vis spectra of Protoporphyrin IX by irradiation at 450 nm in CH_3CN.

Table S12. Distribution coefficients of **1**-**7** between an organic octanol and aqueous phosphate buffer saline phase.

Compound	log*P*
1	+0.2 ± 0.2
2	+0.3 ± 0.2
3	+0.4 ± 0.3
4	+0.2 ± 0.2
5	+0.7 ± 0.3
6	+1.4 ± 0.3
7	+1.7 ± 0.2

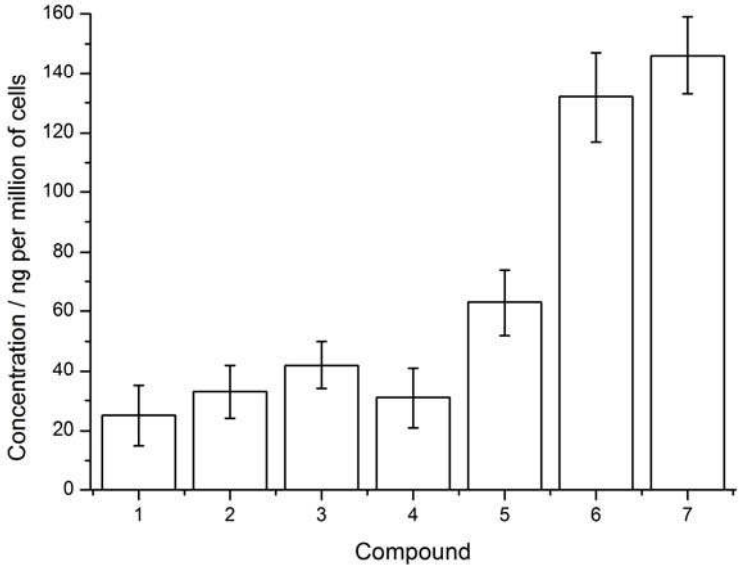

Figure S51. Comparison of the cellular uptake of complexes **1**–**7** after 4 h incubation in HeLa cells.

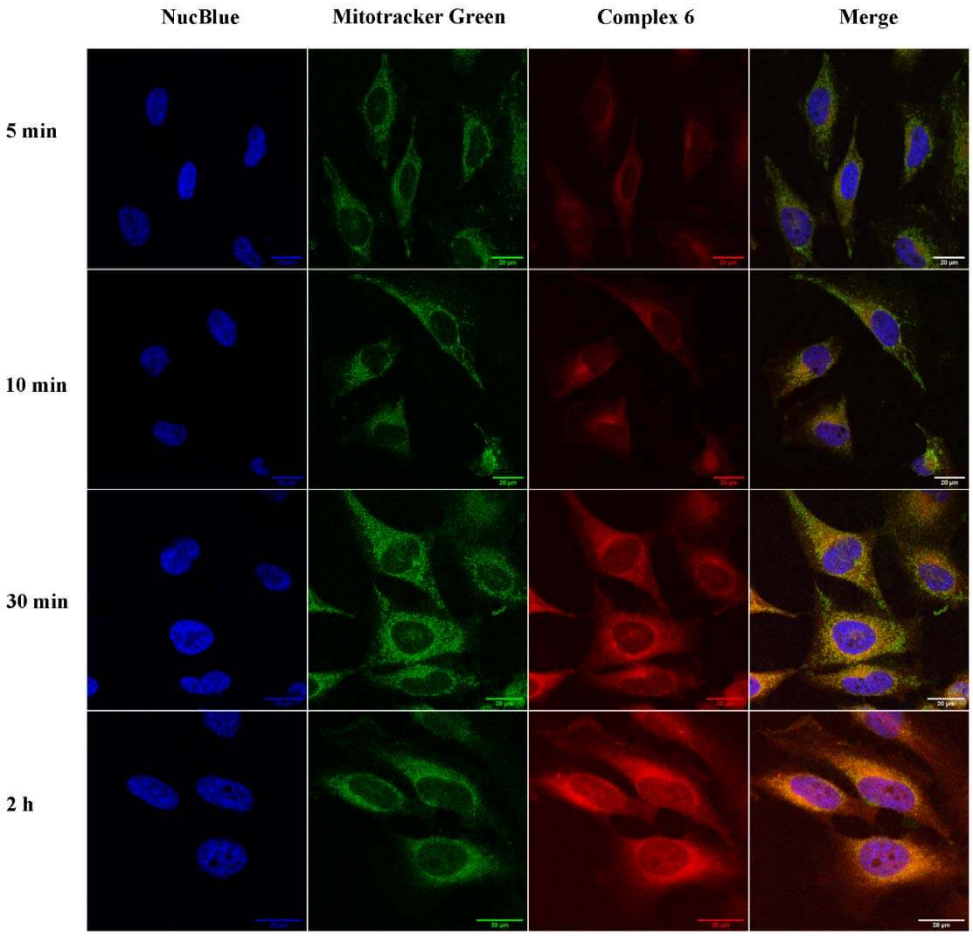

Figure 52. Time-dependent accumulation of complex **6** (14 μM) in HeLa cell line. DNA visualised by NucBlue staining, mitochondria visualised using Mitotracker Green FM (100 nm), complex **6** shown in red. Scale bar, 20 μm.

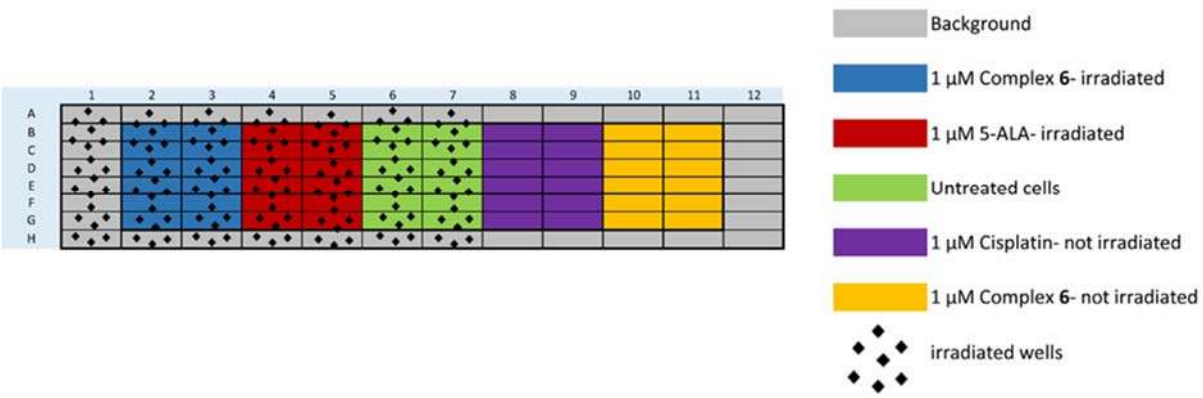

Figure S53. Plate arrangement for Seahorse Mito Stress and Glycolysis Stress experiments.

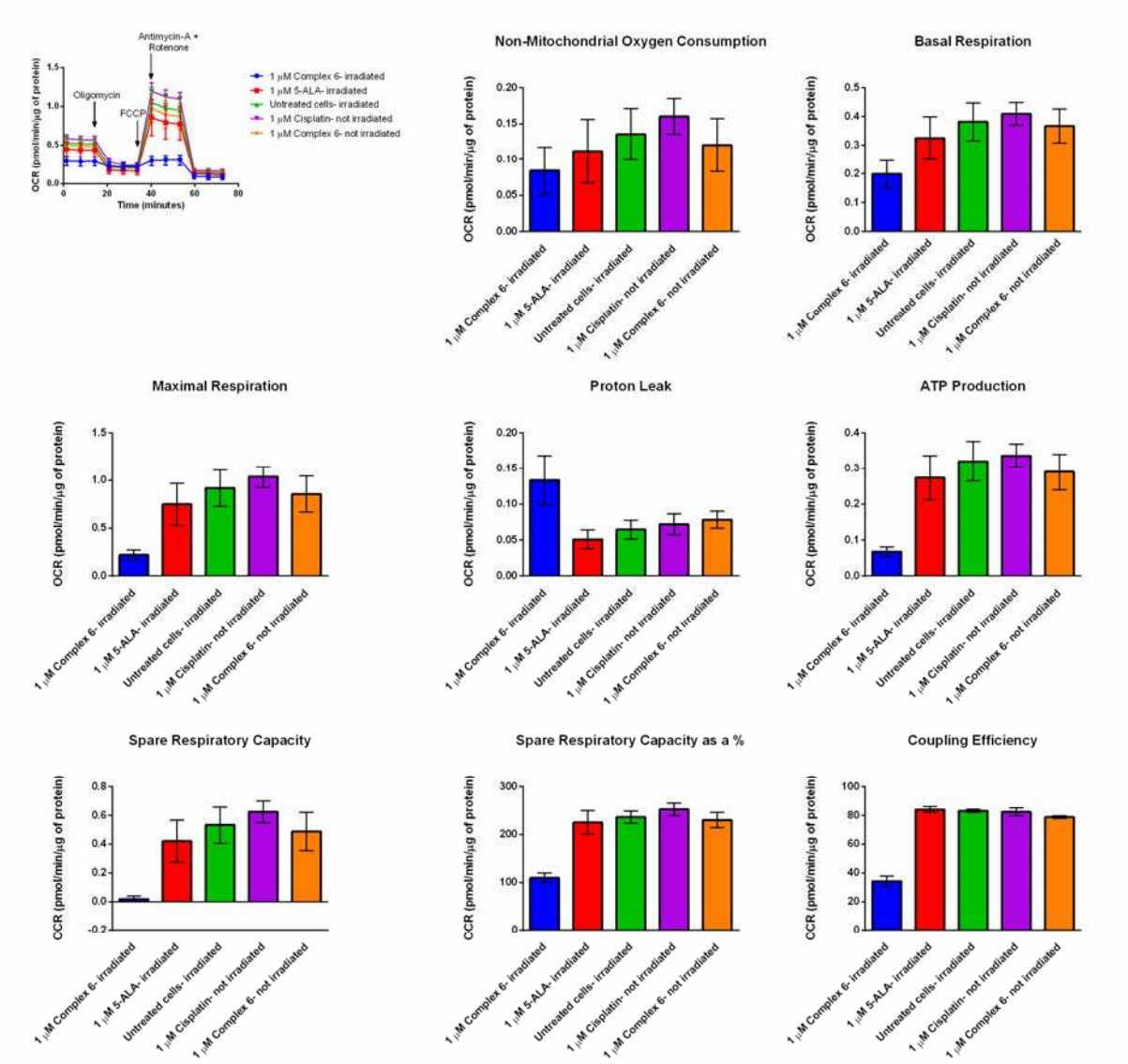

Figure S54. Oxygen consumption rates and different respiration parameters in CT-26 cells alone or after treatment with various test compounds.

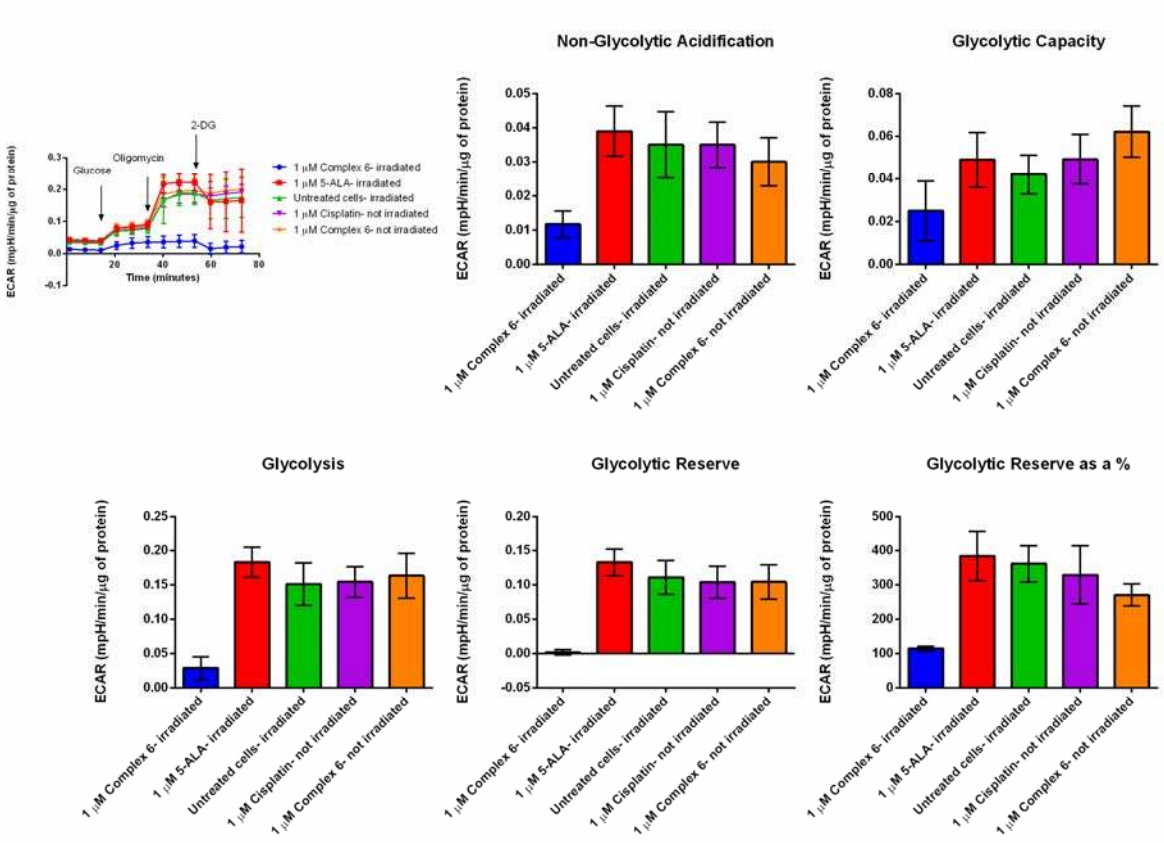

Figure S55. Extracellular acidification rates and different glycolysis parameters in CT-26 cells alone or after treatment with various test compounds.

REFERENCES

1. M. J. Frisch et. al., *Journal*, 2017.
2. T. H. Dunning, Jr. and P. J. Hay, in *Modern Theoretical Chemistry*, ed. H. F. Schaefer III, Plenum, New York, 1977, vol. 3, pp. 1-28.
3. W. J. Hehre, R. Ditchfield and J. A. Pople, *The Journal of Chemical Physics*, 1972, **56**, 2257-2261.
4. P. C. Hariharan and J. A. Pople, *Theoretica Chimica Acta*, 1973, **28**, 213-222.
5. A. Klamt, C. Moya and J. Palomar, *J Chem Theory Comput*, 2015, **11**, 4220-4225.
6. A. D. Becke, *The Journal of Chemical Physics*, 1993, **98**, 5648-5652.
7. C. Ullrich, *Time-Dependent Density-Functional Theory: Concepts and Applications*, Oxford University Press, Oxford, 2012.
8. T. Le Bahers, C. Adamo and I. Ciofini, *J Chem Theory Comput*, 2011, **7**, 2498-2506.
9. F. Maschietto, M. Campetella, M. J. Frisch, G. Scalmani, C. Adamo and I. Ciofini, *Journal of Computational Chemistry*, 2018, **39**, 735-742.
10. B. Sullivan, D. Salmon and T. Meyer, *Inorg. Chem.*, 1978, **17**, 3334-3341.
11. A. Duong, T. Maris, O. Lebel and J. D. Wuest, *The Journal of organic chemistry*, 2011, **76**, 1333-1341.
12. O. Maury, J.-P. Guégan, T. Renouard, A. Hilton, P. Dupau, N. Sandon, L. Toupet and H. Le Bozec, *New J. Chem.*, 2001, **25**, 1553-1566.
13. G. Crosby and W. Elfring Jr, *The Journal of Physical Chemistry*, 1976, **80**, 2206-2211.
14. W. E. Jones Jr, R. A. Smith, M. T. Abramo, M. D. Williams and J. Van Houten, *Inorg. Chem.*, 1989, **28**, 2281-2285.
15. O. Mazuryk, K. Magiera, B. Rys, F. Suzenet, C. Kieda and M. Brindell, *JBIC Journal of Biological Inorganic Chemistry*, 2014, **19**, 1305-1316.
16. R. Clark and J. Reid, *Acta Crystallogr. Sect. A: Found. Crystallogr.*, 1995, **51**, 887-897.
17. *Rigaku Oxford Diffraction*, 2015.
18. A. OLEX, L.J. Bourhis, R. J. Gildea, J. A. K. Howard, H. Puschmann, *J. Appl. Crystallogr*, 2009, **42**, 339-341.
19. G. M. Sheldrick, *Acta Crystallographica Section A: Foundations and Advances*, 2015, **71**, 3-8.
20. G. M. Sheldrick, *Acta Crystallographica Section C: Structural Chemistry*, 2015, **71**, 3-8.
21. A. L. Spek, *Acta Crystallographica Section C: Structural Chemistry*, 2015, **71**, 9-18.
22. K. Nakamaru, *Bull. Chem. Soc. Jpn.*, 1982, **55**, 1639-1640.
23. I. E. Kochevar and R. W. Redmond, in *Methods Enzymol.*, Academic Press 2000, vol. 319, pp. 20-28.
24. D. Garcìa-Fresnadillo, Y. Georgiadou, G. Orellana, A. M. Braun and E. Oliveros, *Helv. Chim. Acta*, 1996, **79**, 1222-1238.
25. S. J. Bruce, I. Tavazzi, V. r. Parisod, S. Rezzi, S. Kochhar and P. A. Guy, *Anal. Chem.*, 2009, **81**, 3285-3296.
26. J. Schindelin, I. Arganda-Carreras, E. Frise, V. Kaynig, M. Longair, T. Pietzsch, S. Preibisch, C. Rueden, S. Saalfeld, B. Schmid, J.-Y. Tinevez, D. J. White, V. Hartenstein, K. Eliceiri, P. Tomancak and A. Cardona, *Nat. Methods*, 2012, **9**, 676-682.